MINISTÉRIO DA CIÊNCIA, TECNOLOGIA E INOVAÇÕES
INSTITUTO NACIONAL DE PESQUISAS ESPACIAIS

sid.inpe.br/mtc-m21d/2022/04.14.14.08-TDI

DEVELOPMENT OF REDUCED GRAPHENE OXIDE SUPPORTED CATALYSTS FOR THE CO_2 HYDROGENATION REACTION

João Lucas Marques Barros

Master's Dissertation of the Graduate Course in Engineering and Space Technologies, guided by Drs. Adriana Maria da Silva, and Evaldo Jose Corat, approved in April 01, 2022.

URL of the original document:
<http://urlib.net/8JMKD3MGP3W34T/46MM4SE>

INPE
São José dos Campos
2022

PUBLISHED BY:

Instituto Nacional de Pesquisas Espaciais - INPE
Coordenação de Ensino, Pesquisa e Extensão (COEPE)
Divisão de Biblioteca (DIBIB)
CEP 12.227-010
São José dos Campos - SP - Brasil
Tel.:(012) 3208-6923/7348
E-mail: pubtc@inpe.br

MINISTÉRIO DA CIÊNCIA, TECNOLOGIA E INOVAÇÕES
INSTITUTO NACIONAL DE PESQUISAS ESPACIAIS

sid.inpe.br/mtc-m21d/2022/04.14.14.08-TDI

DEVELOPMENT OF REDUCED GRAPHENE OXIDE SUPPORTED CATALYSTS FOR THE CO_2 HYDROGENATION REACTION

João Lucas Marques Barros

Master's Dissertation of the Graduate Course in Engineering and Space Technologies, guided by Drs. Adriana Maria da Silva, and Evaldo Jose Corat, approved in April 01, 2022.

URL of the original document:
<http://urlib.net/8JMKD3MGP3W34T/46MM4SE>

INPE
São José dos Campos
2022

Cataloging in Publication Data

Barros, João Lucas Marques.

B278d Development of reduced graphene oxide supported catalysts for the CO_2 hydrogenation reaction / João Lucas Marques Barros. – São José dos Campos : INPE, 2022.

xviii + 131 p. ; (sid.inpe.br/mtc-m21d/2022/04.14.14.08-TDI)

Dissertation (Master in Engineering and Space Technologies) – Instituto Nacional de Pesquisas Espaciais, São José dos Campos, 2022.

Guiding : Drs. Adriana Maria da Silva, and Evaldo Jose Corat.

1. CO2 conversion. 2. Cu-based catalysts. 3. rGO. 4. Surfactants. 5. Deactivation. I.Title.

CDU 141.128

MINISTÉRIO DA CIÊNCIA, TECNOLOGIA E INOVAÇÕES

INSTITUTO NACIONAL DE PESQUISAS ESPACIAIS

Serviço de Pós-Graduação - SEPGR

DEFESA FINAL DE DISSERTAÇÃO JOÃO LUCAS MARQUES BARROS BANCA Nº 077/2022, REGISTRO 912962/2020.

No dia 01 de abril de 2022, por teleconferência, o(a) aluno(a) mencionado(a) acima defendeu seu trabalho final (apresentação oral seguida de arguição) perante uma Banca Examinadora, cujos membros estão listados abaixo. O(A) aluno(a) foi APROVADO(A) pela Banca Examinadora, por unanimidade, em cumprimento ao requisito exigido para obtenção do Título de Mestre em Engenharia e Tecnologia Espaciais/Combustão e Propulsão.

Título: "Development of Reduced Graphene Oxide Supported Catalysts for the CO2 Hydrogenation Reaction".

Membros da Banca:

Dra. Adriana Maria da Silva – Presidente/ Orientadora – INPE/COPDT
Dr. Evaldo Jose Corat – Orientador – INPE/COPDT
Dra. Gisele Aparecida Amaral Labat – Membro Interno – INPE/COPDT
Dr. João Batista Oliveira dos Santos – Membro Externo – UFSCar/DEQ

Documento assinado eletronicamente por **Evaldo José Corat**, **Pesquisador Titular**, em 01/04/2022, às 13:19 (horário oficial de Brasília), com fundamento no § 3º do art. 4º do Decreto nº 10.543, de 13 de novembro de 2020.

Documento assinado eletronicamente por **Adriana Maria da Silva**, **Tecnologista**, em 01/04/2022, às 14:42 (horário oficial de Brasília), com fundamento no § 3º do art. 4º do Decreto nº 10.543, de 13 de novembro de 2020.

Documento assinado eletronicamente por **Gisele aparecida amaral labat (E)**, **Usuário Externo**, em 03/04/2022, às 16:03 (horário oficial de Brasília), com fundamento no § 3º do art. 4º do Decreto nº 10.543, de 13 de novembro de 2020.

Documento assinado eletronicamente por **João Batista Oliveira dos Santos (E)**, **Usuário Externo**, em 05/04/2022, às 13:52 (horário oficial de Brasília), com fundamento no § 3º do art. 4º do Decreto nº 10.543, de 13 de novembro de 2020.

A autenticidade deste documento pode ser conferida no site http://sei.mctic.gov.br/verifica.html, informando o código verificador **9588034** e o código CRC **0BC7DD77**.

Referência: Processo nº 01340.002058/2022-13 SEI nº 9588034

Ao meu amigo Kennedy Kerber

AGRADECIMENTOS

Primeiramente aos meus pais Loide e Cleomar, ao meu irmão Thiago e meu cunhado André, por fazerem de mim quem sou hoje, por todo o suporte na minha jornada até então, e principalmente pelos exemplos de pessoas guerreiras e trabalhadoras que são, os quais carrego comigo hoje e para sempre. Um agradecimento especial à minha namorada Sara, não só pela ajuda no dia-a-dia mas por ser a melhor parceira que alguém pode ter, tanto nos bons momentos quanto nas etapas mais difíceis deste trabalho, onde sempre me proveu muita paciência, amor e carinho, eu jamais teria conseguido sem ela.

Agradeço muito a todos os amigos que fiz na cidade de Cachoeira Paulista por me proporcionarem os pequenos prazeres da vida, tão essenciais nos momentos de correria em um trabalho como este, todos foram muito importantes para a manutenção do meu equilibrio emocional, desejo muito sucesso a todos e que a amizade continue apesar da distância. Também aos meus amigos de infância da cidade de Cascavel - PR, que sempre estiveram presentes para uma boa jogatina e conversas sobre os mais variados assuntos.

Não há palavras suficientes para descrever o quanto sou grato à professora Dra. Adriana Maria da Silva pela paciência, pela excelente orientação e por ter me ensinado aproximadamente tudo que eu sei sobre catálise hoje, além de ter se tornado uma grande amiga pessoal, respeito máximo a ela como pesquisadora e mulher. Agradeço também ao professor Dr. Evaldo Jose Corat pelo aprendizado a respeito dos materiais grafíticos, essencial para o presente trabalho. Outro amigo feito durante o mestrado é o Dr. Carlos Alberto Franchini, ao qual sou muito grato pelas conversas profundas, dicas e pelo suporte técnico com as "engenharias alternativas" instaladas. Fica meu agradecimento sincero também à toda a equipe do Laboratório Associado de Combustão e Propulsão (LCP), incluindo secretarias, seguranças, equipe da limpeza, técnicos e servidores pela manutenção e andamento dos trabalhos no laboratório.

Por fim, o presente trabalho foi realizado com apoio da Coordenação de Aperfeiçoamento de Pessoal de Nível Superior (CAPES) - 33010013 e da Fundação de Amparo à Pesquisa do Estado de São Paulo (FAPESP) - 2018/18798-2, instituições às quais sou grato pelo suporte financeiro e pela continuidade da ciência e tecnologia no estado de São Paulo e no Brasil.

ABSTRACT

The catalytic CO_2 hydrogenation is a potential technology to overcome the current worldwide scenario of high pollution levels and natural resources shortage. In this regard, studies on copper-based catalysts are relevant, as the active sites behavior is not fully understood and deactivation is still an issue. Furthermore, using reduced graphene oxide (rGO) as support is promising to due to the notable physicochemical properties. Hence, this study reports the development of Cu catalysts supported on Zn-rGO hybrids for the CO_2 hydrogenation. To obtain insight on the synthesis procedure, the catalysts were prepared by hydrothermal reduction and wetness impregnation, using Pluronic F127 and Triton X-100 surfactants. Thermogravimetric experiments showed significant effects of surfactants on the thermal stability of the samples. X-Ray diffraction evidenced the synthesis of rGO with few layers and formation of ZnO and Cu_2O phases on the catalysts structure. Large specific surface area results, ranging from 272 to 920 m^2/g, were obtained using adsorption of methylene blue, suggesting improvement when using surfactants. For all samples, highly disordered structures were detected by Raman spectroscopy, suggesting the presence of defects, functional groups and oxygen vacancies. To evaluate CO_2 conversion and products yield, the catalytic unit was tested using $Cu/ZnO/Al_2O_3$ and mixtures with acid catalysts. The results showed increase in conversion and methanol yield with pressure and activity loss, likely due to thermal sintering. DME was obtained with the acid catalysts mixtures and a positive effect on stability was observed with Nb_2O_5. Deactivation also affected all rGO-supported catalysts, resulting in low conversion after 3 h of reaction, although DME traces was obtained. The mass and Raman spectra obtained suggested functional groups were consumed during reduction and reaction procedures, although further characterization is required to confirm the causes of deactivation. The research serves as basis for future development and application of rGO-supported catalysts.

Keywords: CO_2 conversion. Cu-based catalysts. rGO. Surfactants. Deactivation.

DESENVOLVIMENTO DE CATALISADORES SUPORTADOS EM ÓXIDO DE GRAFENO REDUZIDO PARA A REAÇÃO DE HIDROGENAÇÃO DE CO_2

RESUMO

A hidrogenação catalítica de CO_2 é uma potencial tecnologia para superar o atual cenário de alto índice de poluição e escassez de recursos naturais. Neste sentido, estudos sobre catalisadores de cobre são relevantes, visto que o comportamento dos sítios ativos não é totalmente compreendido e a desativação ainda é um problema. Além disso, o uso de óxido de grafeno reduzido (rGO) como suporte é promissor devido às notáveis propriedades físico-químicas. Portanto, este estudo reporta o desenvolvimento de catalisadores de Cu suportados nos híbridos Zn-rGO para a hidrogenação de CO_2. Para obter conhecimento sobre o método de síntese, os catalisadores foram preparados por redução hidrotérmica e impregnação seca, usando os surfactantes Pluronic F127 e Triton X-100. Os experimentos termogravimétricos mostraram efetivo significativo dos surfactantes na estabilidade térmica das amostras. Diffrações de Raios-X evidenciaram a síntese de rGO com poucas camadas e a formação das fases ZnO e Cu_2O na estrutura dos catalisadores. Resultados de área superficial específica elevada, na faixa de 272 a 920 m^2/g, foram obtidos usando adsorção de azul de metileno, sugerindo melhoria com o uso de surfactantes. Para todas as amostras, estruturas altamente desordenadas foram detectadas por espectroscopia Raman, sugerindo a presença de defeitos, grupos funcionais e vacâncias de oxigênio. Para avaliar a conversão de CO_2 e produtividade, a unidade catalítica foi testada usando $Cu/ZnO/Al_2O_3$ e misturas com catalisadores ácidos. Os resultados mostraram aumento na conversão e produtividade com a pressão e perda de atividade, provavelmente devido à sinterização térmica. DME foi obtido com os catalisadores ácidos e um efeito positivo na estabilidade foi observado com Nb_2O_5. Todos os catalisadores suportados em rGO também sofreram desativação, resultando em baixa conversão em 3 horas de reação, embora traços DME tenham sido obtidos. Os espectros de massa e Raman obtidos indicaram que grupos funcionais foram consumidos durante os procedimentos de redução e reação, embora caracterizações adicionais sejam necessárias para confirmar as causas da desativação. A pesquisa serve como base para o futuro desenlvolvimento e aplicação de catalisadores suportados em rGO.

Palavras-chave: Conversão de CO_2. Catalisadores de cobre. rGO. Surfactantes. Desativação.

LIST OF FIGURES

Page

LIST OF TABLES

Page

CONTENTS

1 INTRODUCTION

Over the past century the decreasing fossil fuel resources tendency, along with the dependency of society on oil and natural gas has raised worldwide concerns. Furthermore, the growth in carbon dioxide emission contributed to an increase in global temperature and aggravated climate change due to the 'greenhouse effect'. This overview has given rise to the interest in research and development of new clean alternative energy sources from non-fossil fuel sources (OLAH, 2005).

Among the main strategies for reducing emissions, the recycling of CO_2 emerge as an attractive alternative, as not only it attenuates global climate change effects but also generates value-added products such as chemicals and fuels. However, the main challenge comes from the high thermodynamic stability of CO_2 ($\Delta G^0 = -394$ kJ/mol) and low reactivity, thus requiring energy inputs for its activation and conversion, making catalytic hydrogenation of CO_2 to high value products a promising procedure for atmospheric carbon dioxide recycling (YE et al., 2019).

The catalyst performance and resulting products from the CO_2 hydrogenation reaction depend on the composition of the catalyst employed, as well as its physicochemical properties such as surface area, metallic dispersion and thermal stability. One of the most extensively studied processes is the hydrogenation of CO_2 to methanol over metallic catalysts, mainly Cu-based catalysts, specially the $Cu/ZnO/Al_2O_3$ catalyst, which is widely used industrially, although the exact nature and behavior of the active site in Cu/ZnO catalysts is still controversial, so studies regarding the usage of these materials remain relevant to this day (NIU et al., 2022). Other metals, mainly Pd and Pt, and oxygen vacancies deficient materials have also been used as catalysts for the methanol synthesis.

Overall, the catalytic CO_2 hydrogenation to C_1 products has already been broadly researched and even though significant progress has recently been made in synthesizing C_{2+} compounds, including higher alcohols, olefins and dimethyl ether (DME), there are still many issues to be solved, including catalyst deactivation due to thermal sintering, poisoning, carbon formation and sites deactivation by water formation. Furthermore, the Reverse Water Gas Shift Reaction (RWGSR) competes with methanol and/or DME synthesis during CO_2 hydrogenation conditions. Therefore, currently there is no truly viable catalyst for the hydrogenation to C_{2+} products(SARAVANAN et al., 2017).

Among the reaction products, DME has received increasing attention due to its

outstanding physicochemical properties and wide range of applications, such as Liquefied Petroleum Gas (LPG) blend stock and diesel fuel alternative. In addition, it presents several advantages over other fuels from an environmental viewpoint, including lower NOx, hydrocarbons and CO emissions, sootless combustion and low ozone forming reactivity. These features render DME a potential ultra clean fuel and a possible alternative to fulfill the future energy resource needs (FLEISCH et al., 2012).

Recently carbon based materials including nanotubes, nanofibers and graphene have been getting increasing research interest in catalysis, due to some notable properties that are crucial for catalysts performance, such as large surface area, chemical and thermal stability and interaction with metal compounds (FAN et al., 2015). Many authors have synthesized reduced graphene oxide (rGO) supported catalysts based on metals such as Pd, Ce and Ti achieving high dispersion (FRANCHINI et al., 2020; SHEN et al., 2011; SUN et al., 2013). Furthermore, GO is a 2D network containing sp^2 and sp^3 carbon, as well as functional groups including hydroxyl, epoxy, lactol, ester carbonyl and ketone, suggesting that it possesses an acidic and oxidizing nature (FAN et al., 2015). Thus the exceptional properties of graphene and the synthesis procedures of rGO supported catalysts reported render graphene based materials a potential catalyst for the direct CO_2 hydrogenation to high value products.

The proposed dissertation had the objective of synthesizing, characterizing and evaluating the activity of graphene supported catalysts for the CO_2 hydrogenation reaction. The systems denoted Cu@Zn−rGO and Cu/Zn−rGO were prepared by the hydrothermal and wetness impregnation methods, respectively. Also, the effect of the addition of surfactants was studied. The supports and catalysts developed were characterized by TGA, XRD, Raman spectroscopy, SEM and Methylene Blue Adsorption. The catalytic tests were carried out in a fixed bed unit, previously tested with a commercial $Cu/ZnO/Al_2O_3$ catalyst.

2 LITERATURE REVIEW

2.1 Methanol

Methanol, or methyl alcohol (CH_3OH), is the simplest organic alcohol. At atmospheric conditions, it is a colorless, volatile and flammable liquid. As of 2012, 70% of the global methanol production was used as feedstock in the synthesis of several chemicals, including formaldehyde, methyl-tert-butyl ether (MTBE), acetic acid, dimethyl ether (DME) and propene. As a consequence of the current worldwide scenario mentioned in the previous section, methanol is also receiving increasing attention due to its application as an alternative energy source (JADHAV et al., 2014).

Regarding the usage as energy source, it has been suggested that methanol is an ideal fuel for four-stroke engines. Table 2.1 presents a comparison between the properties of methanol and conventional gasoline. Owning to its relatively elevated heat of vaporization and low calorific value compared to conventional motor fuels, significantly lower temperature may be achieved in combustion chambers. Additionally, NO_x, hydrocarbons and carbon monoxide emissions are lower, even though formaldehyde emission is relevant. Methanol can also be converted into DME, which is a potential diesel fuel substitute. Furthermore, it may be used in refrigeration systems, antifreeze in heating and cooling circuits, protective gas against the formation of hydrates in natural gas pipelines and absorption agent in gas scrubbers (OTT et al., 2000).

Table 2.1 - Gasoline and Methanol properties.

Property	Gasoline	Methanol
Density (kg/L)	0.739	0.787
Caloric value (kJ/kg)	44300	22693
Air consumption (kg/kg)	14.55	6.5
Research octane number	97.7	108.7
Motor octane number	89	88.6
Boiling point range (ºC)	30 - 190	65
Heat of vaporization (kJ/kg)	335	1174

Source: Ott et al. (2000).

In 1923 the first catalytic production of methanol considered industrial was started at Badische Anilin Sodafabrik (BASF) in Germany, the feedstock was synthesis gas (syngas) and the process was conducted at 300 - 400 ºC and drastic pressure conditions, above 300 atm, the catalyst employed was zinc chromite ($Cr_2O_3 - ZnO$)

based. At the time, research was focused on developing iron based catalysts, however it was found that iron was more effective at producing hydrocarbons than methanol, through the Fischer-Tropsch reactions. To improve the poor conversion obtained due to equilibrium limitations, the gas would be recycled over the catalytic bed several times, being cooled in each cycle to condense methanol. To reduce energy costs, and interchanger was later added to the process, using the outlet hot gases to heat the feedstock. Given that syngas was almost never only H_2 and CO, and so a certain quantity of the gas had to be purged, in 1932 a recycling loop with inert components was developed to re utilize the purged gas. Auxiliary beds were also installed to remove unwanted substances. Many of these features are still employed in the current methanol synthesis processes. Figure 2.1 presents a schematic of the basic components of the industrial methanol synthesis, the general setup is still used to this day, with modifications to suit specific industries needs.

Figure 2.1 - Basic components of industrial methanol synthesis.

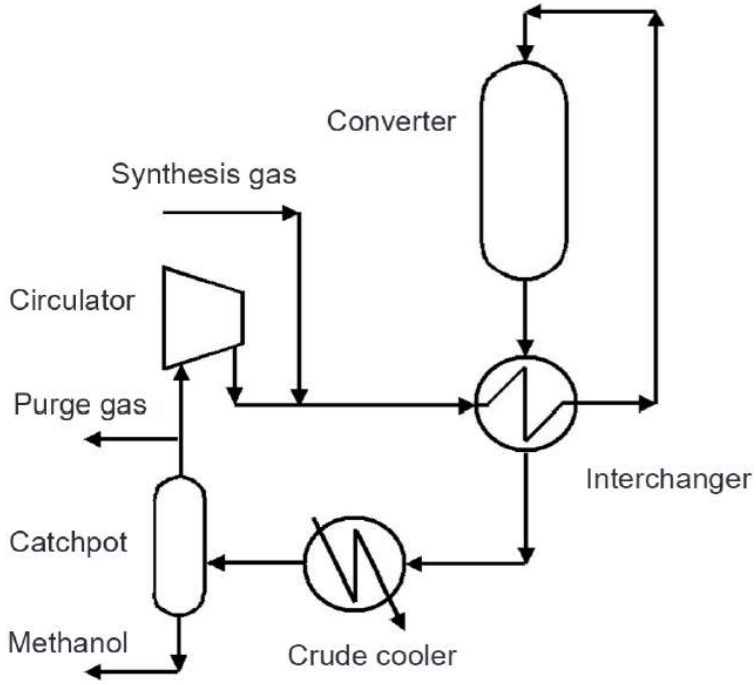

Source: Sheldon (2017).

It was only in 1947 that copper catalysts were introduced, the formulation contained copper, zinc and aluminum synthesized by the co-precipitation method. The catalyst was claimed to be highly selective for methanol. However, as the syngas generation process was changed from coal to natural gas, the feedstock contained sulfur, a poison for copper catalysts. Later, hydrodesulfurisation catalysts were developed in

order to remove sulfur content from naphtha and syngas, maintaining the catalysts activity for longer periods.

In 1960s, significant development was made, mostly by the Imperial Chemical Industries (ICI) of the United Kingdom, creating a process that could operate at 30 - 120 atm and 200 - 300 ^{o}C, using a copper, zinc and chromium catalyst achieving high selectivity (∼99%). Simultaneously, ICI also developed the high pressure steam reformer to convert naphtha and natural gas into syngas, therefore resulting in a complete process from natural gas into methanol, which came to be known as the Low Pressure Methanol (LPM) process, still the most commonly used process for synthesizing methanol to this day (SHELDON, 2017).

In 1997, Nobel Prize winner George A. Olah proposed a "Methanol Economy", a sustainable idea in which methanol would substitute fossil fuels for the energy needs of the modern society. In this sense, methanol would be produced from renewable sources, including the direct oxidative conversion of methane and conversion of atmospheric CO_2. Given the convenient ease of storage and transportation, methanol would be used as fuel and the building block for synthetic hydrocarbons (OLAH, 2005).

The fast growth in consumption of methanol in China, the world leading country in terms of methanol usage, over the years (Figure 2.2) represent a trend in emerging economies, where methanol demand is rapidly increasing. The global methanol market is 30.7 billion USD as of 2021, and it is expected to be 36.3 billion USD by 2026, with compound annual growth rate of 3.4%, a promising value for large companies (MARKETS; MARKETS., 2021).

Figure 2.2 - Methanol consumption in China from 2000 to 2016.

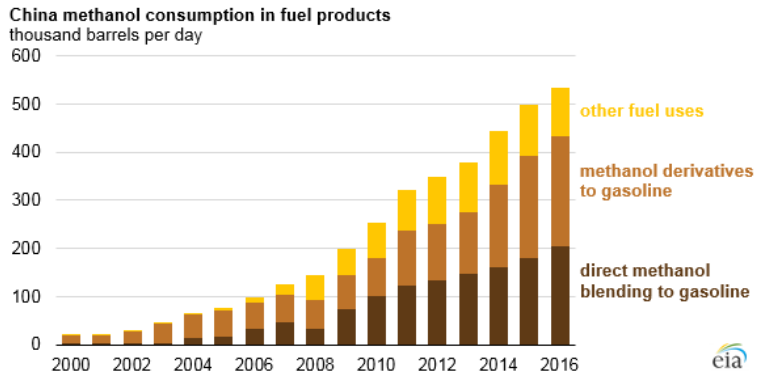

Source: DUNN (2017).

Regarding the economics of methanol synthesis, the most crucial factor that determines the viability of the process is the feedstock cost. As shown in Figure 2.3, methanol produced by CO_2 recovered from effluents or atmosphere captured is currently the most expensive product, most likely due to formerly mentioned high stability of the molecule, resulting in poor conversion values. Furthermore, these gases do not contain sufficient amounts of hydrogen for the catalytic process, and so water-splitting must be used to adequate the reactant. This overview render the large-scale industrial production of methanol using CO_2 not currently viable (ROODE-GUTZMER et al., 2019).

Figure 2.3 - Estimated production cost for methanol from different feedstock.

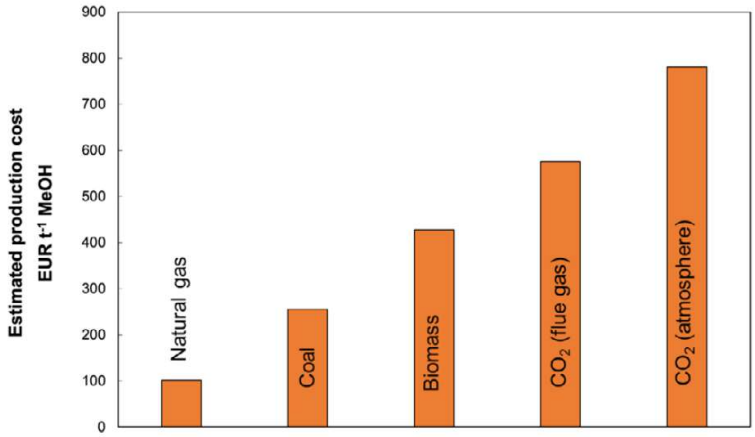

Source: Roode-Gutzmer et al. (2019).

Overall, the main challenges that science and engineering have to overcome in order to make the as-suggested methanol economy a reality are reducing the current CO_2 capture, storage and treatment technologies costs, along with the development of novel low-cost, highly active and selective catalysts for CO_2 conversion. It is noteworthy to highlight that a true renewable methanol synthesis process must use products waste as carbon source, the hydrogen employed must not be derived from fossil fuel and the energy source for the entire process must come from a renewable source.

2.2 Dimethyl Ether

Dimethyl Ether (DME) is the most elementary ether, having the chemical formula CH_3OCH_3. It is a colorless gas at ambient condition and easily liquefiable under relatively low pressures, it also burns with a visible blue flame and is non-peroxide forming in pure state or in aerosol formulations (OGAWA et al., 2003; SEMELSBERGER

et al., 2006). DME has a wide range of possible applications, including Liquefied Petroleum Gas (LPG) blend stock in residential cooking/ heating sector, LPG/DME blends as transportation fuel using spark ignition (SI) engines, diesel fuel alternative, chemical intermediate in olefins production, gas turbine fuel and other potential markets such as fuel cell technology. A review by Fleisch, Basu and Sills (FLEISCH et al., 2012) on the status of DME development in China and other countries shows that DME has very interesting physical properties, which makes it advantageous compared to other fuels. Table 2.2 presents a comparison between some physical properties of DME and other hydrocarbon fuel.

Table 2.2 - Physical properties of DME and specific hydrocarbon fuels.

Property	Propane	Methanol	DME	Diesel Oil	Methane
Boiling Point (ºC)	-42	64.6	-25.1	180 - 360	-161.5
Vapor Pressure (bar) at 20ºC	8.4	-	5.1	-	-
Liquid Density (g /cm³) at 20ºC	0.509	0.790	0.670	0.840	-
Sp. Gravity (vs. Air)	1.52	-	1.69	-	0.55
Flammability Limits (% vol)	2.1 - 0.4	5.5 - 36.0	3.4 - 17.0	0.6 - 7.5	5.0 - 15.0
Cetane Number	5	5	55 - 60	40 - 55	0
Calorific Value (Kcal /Kg), LHV	11.1	4800	6900	10.2	12.0
Calorific Value (Kcal /nm³), LHV	21.8	-	14.2	-	8600

Source: Fleisch et al. (2012).

DME is a flammable, thermally-stable liquid that can be handled in a similar way to LPG. For those reasons, the largest market for DME is the usage as a blend fuel with LPG, so much that as of 2012, 90% of the total DME produced in China was blended with LPG. In residential cooking and heating sector, DME and LPG can be used both as a mixture or separately. Studies show that a usage of 15 - 20% DME in LPG/DME blends does not require any modification in existing home and restaurants cooking appliances or distribution. According to the International DME Association (IDA), the fuel has been recognized as a clean fuel with the perspective to reduce indoor air pollution in Asia and Africa (FLEISCH et al., 2012).

With rising concerns about petroleum shortage, DME is gathering attention as a potential diesel substitute. As shown in Table 2.2, DME's high cetane number makes it an efficient fuel, other advantages of DME over diesel include lower NOx, hydrocarbons and CO emissions, sootless combustion, low auto-ignition temperature and lower engine noise (SEMELSBERGER et al., 2006). Due to high oxygen content and no $C - C$ bonds in the DME molecule, its combustion produces almost zero soot, which implies that DME-fuelled engines would not need a particulate filter. Shorter

ignition delay, smaller amount of fuel injected during ignition and smaller amount of fuel burned during the pre-mixed phase cause NOx emissions to be lower on DME than in diesel engines. Because DME has a short ignition delay period, the over-rich and over-lean mixture regions might be smaller, resulting in reduced HC and CO emissions (ARCOUMANIS et al., 2008). The review by Semelsberger et al. (SEMELSBERGER et al., 2006) include data of a road load test comparing DME and Diesel engines emissions. The data is presented in Figure 2.4.

Figure 2.4 - Road load test data comparing engine emissions using diesel and neat DME.

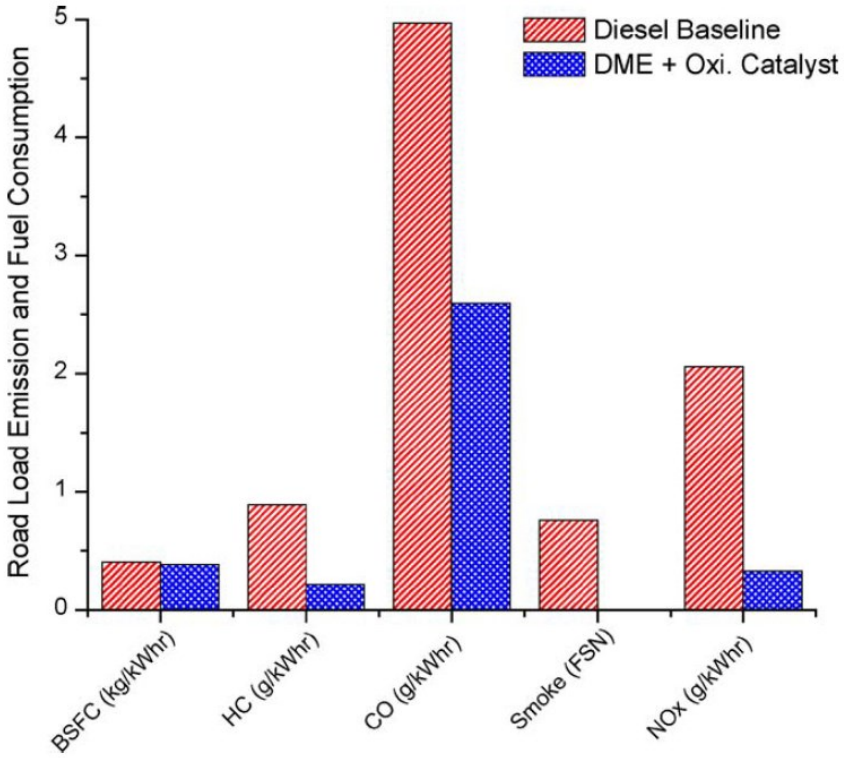

Source: Semelsberger et al. (2006).

A challenging aspect of using a DME engine is the viscosity of the fuel, which is approximately 20 times lower than diesel viscosity. This leads to an increase in leakage in pumps and fuel injectors. Also, there are still lubrication problems with DME, which results in reduced engine lifetime and possible failures in pumps and injectors (SEMELSBERGER et al., 2006).

DME can also be used as propellant for arcjet thruster, a space propulsion device used for North-South station-keeping in satellites. Due to specific physical properties

such as boiling point, freezing point and vapor pressure at room temperature, it is possible to store DME as a liquid under a relatively low pressure compared to other propellants including hydrazine. As confirmed by Kakami et al. in a demonstration experiment, a prototype DME arcjet thruster operated at a discharge power of 1 kW, specific power in the range 20 - 40 MJ / kg and plenum chamber pressure from 40 to 160 kPa, approximately the same operating conditions of conventional thrusters, thus indicating that DME is a potential propellant for this device with storage advantages (KAKAMI et al., 2008). Additionally, DME is considered a green propellant due to its advantages from a environmental viewpoint.

2.2.1 Environmental impact

Over the past decades, environmental pollution and the greenhouse effect resulting from the inordinate use of petroleum based energy sources have caused concerns and attention to the development of alternative energy resources. Also, worldwide laws and regulations have been imposed on diesel fuel usage in all areas. In an early work by Fleisch et al., DME was highlighted as a potential ultra clean fuel (FLEISCH et al., 1997).

Firstly, dimethyl ether is not harmful to the ozone layer, showing low ozone forming reactivity compared to other hydrocarbon fuels, as presented in Figure 2.5.

From a greenhouse gas emission viewpoint, DME is one of the best fuels to use. Fleisch et al., also analysed Cradle-to-grave greenhouse gases emissions for several traditional fuels and DME, the results are shown in Figure 2.6. A CO_2 equivalent ratio of 50 for methane and 300 for nitrous oxide was employed with three different models for the calculation. DME presented a equivalent ratio in the range 96 - 114, one of the lowest of all fuels studied (FLEISCH et al., 1997).

Regarding global warming, Good and Francisco (GOOD et al., 1998) reported short atmospheric lifetimes and insignificant infrared absorption, resulting in small Global Warming Potentials (GWP) for DME, indicating that it is benign to the atmosphere. Table 2.3 shows a comparison between GWP values for CO_2, CH_4, N_2O and DME previously reported (GOOD et al., 1998; SEMELSBERGER et al., 2006).

Table 2.4 presents worldwide emission regulations for trucks compared to an emission data for a DME-fueled truck (FLEISCH et al., 2012). The specific emissions of NOx, CO, Unburned Hydrocarbons (UHC) and Particulate Matter (PM) from the usage of DME were lower than those required in all regulations.

Figure 2.5 - Relative Ozone-Forming Potentials of Various Hydrocarbons.

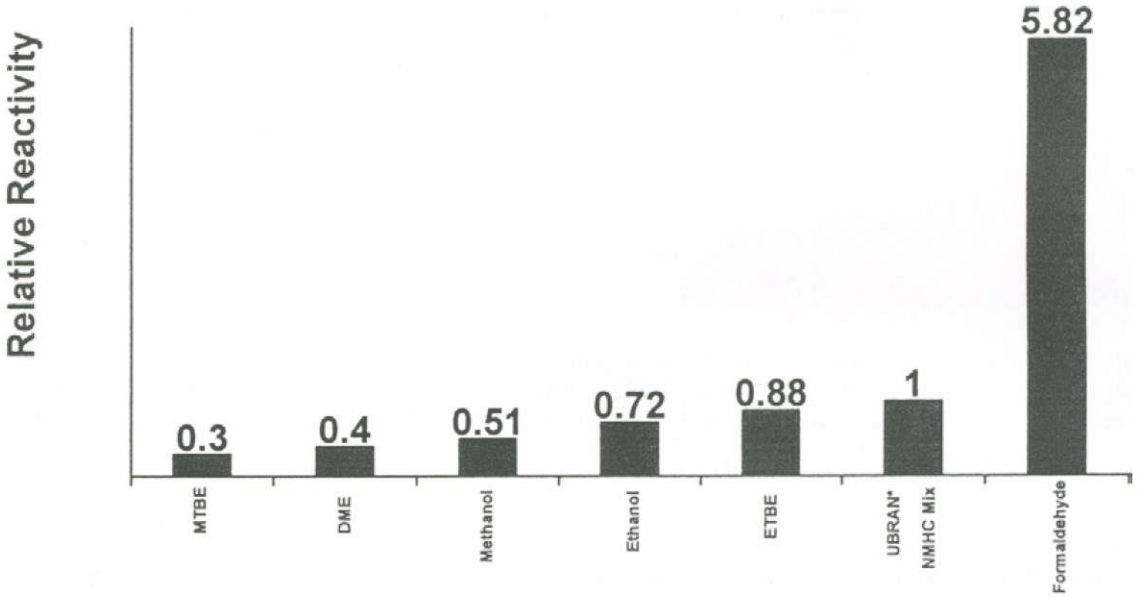

Source: Fleisch et al. (1997).

Figure 2.6 - Relative Greenhouse Emissions of fuels.

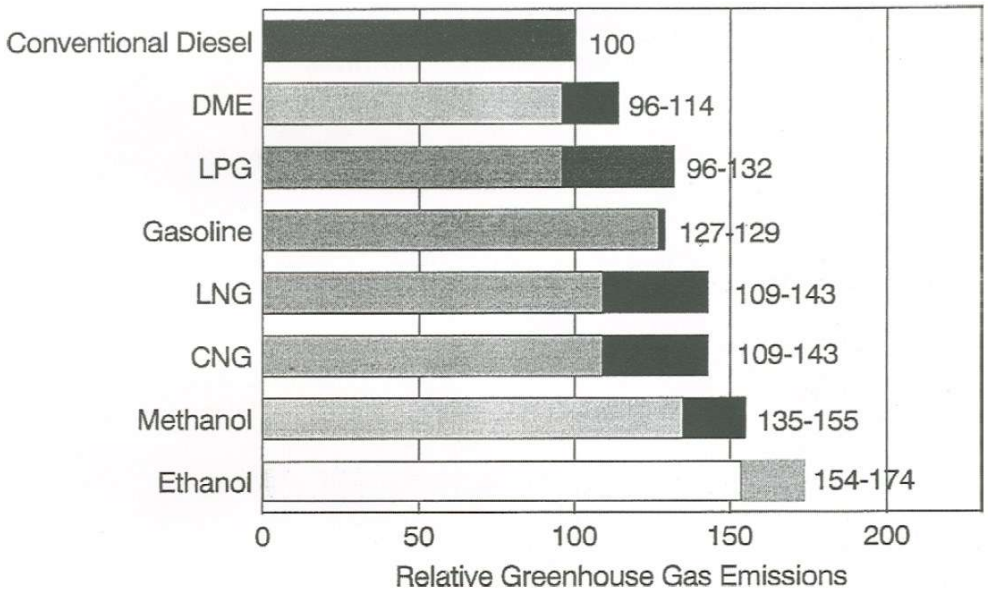

Source: Fleisch et al. (1997).

From a health impacts standpoint, despite being a volatile organic compound, DME is non-carcinogenic, non-teratogenic (does not produce physical or functional defects in the human embryo), non-mutagenic and non-toxic (SEMELSBERGER et al., 2006).

There are two main procedures for obtaining DME, one of them being a two step

Table 2.3 - Global Warming Potentials (GWP).

	Time horizon		
	20 years	100 years	500 years
DME	1.2	0.3	0.1
CO_2	1.0	1.0	1.0
CH_4	56.0	21.0	6.5
N_2O	280.0	310.0	170.0

Source: Semelsberger et al. (2006).

Table 2.4 - Emission data for DME-fueled truck, gms/kwhr.

	NOx	CO	UHC	PM
Japan 2009 regulations	0.70	2.22	0.17	0.01
US-2010 regulations	0.27	20.80	0.19	0.01
Euro-VI 2013 regulations	0.40	1.50	0.13	0.01
DME Truck Test Data	0.11	0.21	0.12	0.001

Source: Fleisch et al. (2012).

process in which methanol is usually synthesized from synthesis gas (CO + H_2) on catalysts composed of metals and oxides in the first step, then DME is produced by dehydration of methanol over an acid catalyst in the second step. The first step, however, is thermodynamically limited, in the sense that an increase in the reaction temperature promotes CO_2 activation, but a decrease in temperature favors methanol production, this method also requires two reactors. The other procedure is a single step process where DME is directly produced by CO_2 and H_2 mixtures (CO_2 hydrogenation), this alternative route is getting industrial and research interest not only for the lower thermodynamic limitation, but also reduced operation costs (FRUSTERI et al., 2015a).

2.3 Catalytic CO_2 hydrogenation

The usage of fossil fuels in the form of coal, petroleum and natural gas has granted an era of advancement and profitability for human development over the past two centuries. Coal as an energy source was dominant in the 18th century with the industrial revolution, currently it is used mainly for generating electricity and even though our coal reserves may last for many centuries, coal mining is increasingly affected by environmental struggles and safety. Oil and natural gas have become progressively dominant energy sources and raw materials for chemicals over the last few decades. However, due to the expanding world population, oil reserves may last for approximately 40 years. This overview has caused concerns since society

still depends on fossil fuels for the majority of its energy needs ($\sim$ 80%), also the combustion of fossil fuels releases substantial amounts of carbon dioxide (OLAH, 2005).

The striking increase on the atmospheric CO_2 concentration levels (from 280 to 390 ppm) contributed to an increase in global temperature and aggravated climate change. The relevance of this issue is emphasized by international action both from governments and companies, including the Intergovernmental Panel of Climate Change (IPCC), the United Nations Framework Commission on Climate Change, the Global Climate Change Initiative and the European Strategic Energy Technology Plan (SET-Plan). Furthermore, as of 2022, an incentive prize of one hundred million US dollars is being awarded for teams to propose an economically viable scale model for removing carbon content from the atmosphere (ALVAREZ et al., 2017; SAEIDI et al., 2014; MUSK, 2021).

Currently, there are three main strategies for reducing CO_2 emissions: reduction of CO_2 produced, capture and storage of CO_2 and usage of CO_2 emitted. The latter strategy is attractive, since it reduces global climate change effects and also generates value-added products such as chemicals and fuels, this provides new opportunities for industrial development. One of the challenges in transforming CO_2 into other chemicals is the high thermodynamic stability of the compound ($\Delta G^0 = -394$ kJ/mol), thus requiring high energy substances such as hydrogen to activate the molecules (SAEIDI et al., 2014).

Over the years, the catalytic CO_2 hydrogenation to C_1 products has been widely studied, however, there are still several obstacles in facilitating the conversion of CO_2 into high-value C_{2+} species including higher alcohols, olefins and dimethyl ether (DME). The challenges to be overcome include improving stability towards thermal sintering and carbon deposition, raising conversion, enhancing selectivity to the desired products and inhibiting the Reverse Water Gas Shift Reaction (RWGSR) (SARAVANAN et al., 2017; YE et al., 2019).

The methanol synthesis from CO_2 hydrogenation and methanol dehydration to DME are represented by Reactions 2.1 and 2.2, respectively (AHMAD; UPADHYAYULA, 2019). The Reverse Water Gas Shift Reaction (RWGSR), a which is a side reaction

present in the CO_2 hydrogenation mechanism is represented by Reaction 2.3.

$$CO_2 + 3\,H_2 \rightleftharpoons CH_3OH + H_2O \qquad \Delta_{H_{298}} = -49.51\,\text{kJ/mol} \tag{2.1}$$

$$2\,CH_3OH \rightleftharpoons CH_3OCH_3 + H_2O \qquad \Delta_{H_{298}} = -23.40\,\text{kJ/mol} \tag{2.2}$$

$$CO_2 + H_2 \rightleftharpoons CO + H_2O \qquad \Delta_{H_{298}} = +41.19\,\text{kJ/mol} \tag{2.3}$$

2.3.1 Effect of operating conditions

The operating conditions play an important role in the CO_2 hydrogenation reaction. CO_2 conversion and product selectivity are strongly dependent on temperature, pressure, molar H_2/CO_2 ratio of the reactant mixture and space velocity, which is often presented in the literature as the Gas Hourly Space Velocity (GHSV), expressed in h^{-1}, the inverse of residence time.

A computational thermodynamic analysis of CO_2 hydrogenation to methanol, DME and hydrocarbons (AHMAD; UPADHYAYULA, 2019) predicts that CO_2 conversion at equilibrium increases with pressure, effect attributed to the equilibrium shift towards the products, according to Le Chatelier's principle. Also, increasing pressure lowers CO selectivity. At low pressures (1 bar), CO_2 conversion increases with temperature, but under high pressure conditions (~ 60 bar) the conversion experiences a decrease when temperature rises from 100°C to approximately 300°C and then increases at higher temperatures. The results indicate that the higher the reaction temperature, the lower the selectivity to methanol and DME, as expected from exothermic reactions. However, low temperature conditions (< 250 °C) may be insufficient for the activation of the CO_2 molecules, on the other hand, higher temperatures may promote the endothermic RWGSR therefore requiring a temperature compromise to obtain the best possible results. Regarding the effect of feed composition on CO_2 conversion and selectivity to methanol and DME, the authors suggest that by increasing H_2/CO_2 molar feed ratio, CO_2 functions as the limiting reactant, improving conversion. By comparing the simulations performed with experimental data, it was acknowledged that a 3:1 H_2/CO_2 molar ratio condition resulted in the highest CO_2 conversion and selectivity to methanol and DME.

Table 2.5 - Effect of operating conditions over CO_2 conversion and selectivity to Methanol.

Catalyst	T(ºC), P(bar)	GHSV (h^{-1})	H_2/CO_2	X (%)	S (%)	Ref
12%Cu-6%V/γ-Al_2O_3	240, 30	1800	3	14.0	19.0	(ZHANG et al., 2007)
12%Cu-6%V/γ-Al_2O_3	240, 30	3600	3	13.0	23.0	(ZHANG et al., 2007)
12%Cu-6%V/γ-Al_2O_3	240, 30	5400	3	11.0	27.0	(ZHANG et al., 2007)
12%Cu-6%V/γ-Al_2O_3	240, 30	7200	3	9.0	32.0	(ZHANG et al., 2007)
12%Cu-6%V/γ-Al_2O_3	220, 30	3600	3	7.0	32.0	(ZHANG et al., 2007)
12%Cu-6%V/γ-Al_2O_3	260, 30	3600	3	18.0	16.0	(ZHANG et al., 2007)
12%Cu-6%V/γ-Al_2O_3	280, 30	3600	3	20.0	14.0	(ZHANG et al., 2007)
Cu/ZnO/Al_2O_3	250, 20	3600	3	15.8	22.8	(LIU et al., 2003)
Cu/ZnO/Al_2O_3	250, 20	10000	3	15.1	21.9	(LIU et al., 2003)
Cu/ZnO/ZrO_2	230, 30	-	3	15.2	35.1	(RAUDASKOSKI et al., 2007)
Cu/ZnO/ZrO_2	250, 30	-	3	19.4	29.3	(RAUDASKOSKI et al., 2007)
Cu/ZnO/ZrO_2	270, 30	-	3	22.8	21.3	(RAUDASKOSKI et al., 2007)

Source: Author.

Several authors have reported experimental results for the CO_2 hydrogenation to methanol at different operating conditions (LIU et al., 2003; RAUDASKOSKI et al., 2007; ZHANG et al., 2007), Table 2.5 presents the effect of the parameters on the conversion and selectivity. Even though the temperature range is narrow, it can still be noted from all studies that increasing temperature results in an increase in CO_2 conversion and a decrease in methanol selectivity due to the exothermic nature of the reaction, the results are in agreement with the thermodynamics simulations mentioned previously. Using a copper based catalyst promoted by vanadium, (ZHANG et al., 2007) performed CO_2 hydrogenation at different temperature and space velocity conditions, observing that increasing GHSV has a negative effect on the conversion, possibly due to short residence time not being sufficient to activate CO_2, on the other hand, low GHSV (1800 h^{-1}) decreases selectivity, indicating that long residence time may promote side reactions such as RWGSR. (LIU et al., 2003) reported a similar effect on the conversion, although selectivity also decreased in a high GHSV condition. Overall, the studies suggest that space velocity in the range 3000 - 5000 h^{-1} appears to be a decent compromise. The analysis serves to have a grasp on the effects of operating conditions in the methanol synthesis.

A few authors reported the effect of catalyst composition and operating conditions on the direct synthesis of DME from CO_2 hydrogenation (BONURA et al., 2017; FRUSTERI et al., 2015a; SUN et al., 2004; WANG; ZENG, 2005; WENGUI et al., 2013; ZHANG et al., 2014). The results are displayed in Table 2.6. The effect on temperature in this reaction is similar to the observed in the methanol synthesis, higher temperature results in higher DME selectivity values but lower CO_2 conversion, as can be observed in the work by Bonura et al. (BONURA et al., 2017). Sun et al. achieved $73,6\%$ DME selectivity by loading Pd on the $CuO/ZnO/Al_2O_3/ZrO_2/HZSM-5$ hybrid catalyst

and performing the reaction at low temperature (SUN et al., 2004). Also in agreement with methanol synthesis is the effect of space velocity on CO_2 conversion, however, the results reported by (FRUSTERI et al., 2015a) indicate that lowering space velocity improved selectivity as well. The data also suggests that increasing pressure improves both conversion and selectivity.

Table 2.6 - Summary of the effect of operating conditions over CO_2 conversion and selectivity to DME.

Catalyst	T(°C), P(bar)	Space velocity	H_2/CO_2	$X(\%)$	$S(\%)$	Ref
$Cu/ZnO/Al_2O_3/SiO_2$	250, 30	3200 h^{-1}	4	12.0	40.0	(WANG; ZENG, 2005)
$Cu/ZnO/Al_2O_3/HZSM-_5$	270, 30	4200 h^{-1}	3	30.6	49.2	(ZHANG et al., 2014)
$Cu/ZnO/Al_2O_3/La_2O_3$	250, 30	3000 h^{-1}	3	43.8	71.2	(WENGUI et al., 2013)
CuZnZr/ferrierite	220, 50	8800 NL $Kg^{-1}h^{-1}$	3	11.5	17.5	(BONURA et al., 2017)
CuZnZr/ferrierite	240, 50	8800 NL $Kg^{-1}h^{-1}$	3	18.0	14.0	(BONURA et al., 2017)
CuZnZr/ferrierite	260, 50	8800 NL $Kg^{-1}h^{-1}$	3	23.0	13.0	(BONURA et al., 2017)
$CuZnZr/HZSM-_5$	240, 30	10000 NL $Kg^{-1}h^{-1}$	3	15.9	38,5	(FRUSTERI et al., 2015a)
$CuZnZr/HZSM-_5$	240, 30	2500 NL $Kg^{-1}h^{-1}$	3	19.3	44.6	(FRUSTERI et al., 2015a)
$CuZnZr/HZSM-_5$	240, 50	2500 NL $Kg^{-1}h^{-1}$	3	23.6	49.3	(FRUSTERI et al., 2015a)
$Cu/ZnO/Al_2O_3/ZrO_2$ + Pd	200, 30	1800 h^{-1}	3.3	18.7	73.6	(SUN et al., 2004)

Source: Author.

In conclusion, the literature suggests that the CO_2 hydrogenation reaction should by carried out using the following operating conditions: reaction temperature in the range 200 - 300 °C, pressure at 20 bar or higher, 3:1 H_2/CO_2 molar ratio in the reactant mixture and GHSV from 2000 to 5000 h^{-1}.

2.3.2 Catalysts and supports

Aside from the operating conditions of the catalytic CO_2 hydrogenation reaction, the properties of the catalyst to be employed, such as the active species, surface area, thermal and chemical stability, metal crystallite size and oxidation state have a crucial role on the activity and selectivity obtained in the process. In this sense, even though a variety of different active species has been studied, copper-based catalysts are still the most relevant, as Cu is a major abundant element and has been proven to be highly active in converting CO_2. Therefore, Cu catalysts are low cost and effective materials for the CO_2 hydrogenation reaction. However, challenges still remain as current research focuses on better understanding the exact behavior of active sites, the role of promoters and the reaction mechanism, as well as optimizing the catalysts by modifying synthesis procedures and further adding components to the catalytic system.

2.3.2.1 Cu/ZnO catalysts

As mentioned above, to this day the exact nature of the active site for H_2 dissociation and CO_2 activation remains controversial. A review by (NIU et al., 2022) gathered results from several authors, in which some agree that metallic copper is responsible for the overall catalytic activity, depending only on the metallic surface area, while others found that the activation of CO_2 is independent of Cu^0 and the active site is Cu^{+1} instead (YANG et al., 2013). Additionally, more recent studies suggest that it is the interaction between Cu and a support such as Zn that actually promotes catalytic activity, however, even this effect is unclear, as some results point to the interaction of oxides and some indicate the formation of alloys to be the the main active component. Furthermore, it has also been proposed that the activity may be proportional to both Cu^0 and Cu^{+1}. What is clear though, is the positive synergistic effect of Cu and the Zn support, affecting the morphology and electronic properties of catalysts. The interaction results in smaller particle size, decreasing diffusion of the reactant molecules and rendering active sites more accessible, as well as increasing surface area, which may prevent deactivation (LIU et al., 2003). In the attempt to optimize the performance of Cu/ZnO catalysts, over the years many authors have reported the utilization of different materials in CO_2 hydrogenation, with changes on the synthesis procedure and addition of promoter. Hence, even though copper catalysts have been researched for many years, current studies on the material are still relevant.

In a study aiming to understand the synergy of Cu and Zn, (VALANT et al., 2015) prepared a series of Cu/ZnO catalysts through different methods: physical mixtures of Cu and ZnO with varying Zn content, Cu@ZnO_x core-shell catalysts by surface modification precipitation, Cu@ZnO_x/ZnO nano-core-shell materials by wet impregnation with 1% Cu content and Cu-ZnO coprecipitates. By physically mixing CuO and ZnO, the authors obtained core(Cu)-shell(Zn) structures that showed low conversion (less than 1%) but 100% selectivity to methanol, indicating that this configuration is not active for the RWGSR and that optimal methanol yield is obtained with 62% weight of ZnO. Additionally, both intended core-shell structures also inhibited CO formation, with the Cu@ZnO_x catalyst yielding the most methanol quantity per kg of fresh catalyst, while the nano-core-shell material yielded more methanol per kg of copper. On the other hand, the coprecipitates were active for the RWGSR and presented poor selectivity to methanol. The authors suggest that the active site for methanol synthesis is derived from the interaction of Cu and ZnO and that core-shell is a promising structure for highly selective catalysts.

Using the Supercritical Antisolvent (SAS) precipitation methodology, (KONDRAT et al., 2016) were able to stabilize the rare georgite copper zinc mineral. Obtaining catalysts that were found to be more selective to methanol (selectivity obtained was over 99%) than the standard industrial catalyst, which uses other forms of more readily-obtainable minerals such as zincian malachite, aurichalcite and rosasite. The innovative work demonstrates that well established catalysts may still be further optimized by more advanced synthesis procedures.

For over 40 years, $Cu/ZnO/Al_2O_3$ catalysts have been widely studied and employed industrially, presenting decent activity and selectivity to methanol. Also, it has been demonstrated that Al_2O_3 provides chemical and thermal stability to the system while preventing deactivation by sulphur to some extent. Furthermore, the balance of basic and acid sites present in ZnO and Al_2O_3, respectively, prevents methanol to be converted into other products (LIU et al., 2003). Therefore, aluminum oxides are the most commonly used promoters both in research and industry. However, as deactivation due to thermal sintering and CO formation are still persisting issues and methanol is a product in high demand, several studies have been also reported on modifications of the $Cu/ZnO/Al_2O_3$ catalyst in order to further optimize CO_2 conversion and methanol selectivity.

It has been proposed the impregnation Pd in small quantities (4 and 10% wt.) to the conventional methanol synthesis catalyst. Even though the temperature range used was lower than for most studies on CO_2 hydrogenation, the authors found that the synthesized catalyst presented a slight improvement in methanol yield per Cu mole. CO formation increased with temperature as expected from the RWGSR, and methane traces were also detected. Nevertheless, the authors reported decreasing CO_2 conversion by adding Pd, indicating that employing promoters may not be straightforward positive for performance, and so careful analyses must be conducted in order to optimize existing catalysts (MELIÁN-CABRERA et al., 2002).

On the other hand, the addition of Al and Zr promoters to the conventional Cu/ZnO catalyst has been reported with improved performance. (AN et al., 2007) included different amounts of Al and Zr in the coprecipitation synthesis of Cu/ZnO. All materials were found to be fibrous, with highly dispersed Cu/Zn crystallites. The catalyst containing 5% mol of the promoters presented CO_2 conversion 17% higher than the commercial counterpart at mild conditions of 230 ^{o}C and 40 bar, methanol yield and selectivity were increased by 81% and 31%, respectively. Additionally, a stability test was performed for 300 h time on stream, where methanol yield

was maintained during the entire process. XRD analysis indicate smaller zinc oxide crystallites in the promoted samples and the authors suggest that Zr^{+4} dissolved in ZnO formed ion defects on the catalyst surface, which might have absorbed Cu^{+1} and stabilized a larger quantity of active sites. The results show that the addition of promoters can lead to improved catalytic activity even in small quantities.

Regarding alternative synthesis procedures, (HONG et al., 2002) prepared a series of $Cu/ZnO/Al_2O_3$ catalysts using the natural polymer gelatin, in order to avoid agglomeration of particles during calcination. Characterization of the catalyst with 12.7% wt. of gelatin indicated increase in BET surface area, pore volume, Cu surface area and decrease in Cu crystallite size when comparing to the same material synthesized by conventional coprecipitation without the addition of the polymer. Also, the catalytic test result shows slightly improved CO_2 conversion as well as methanol yield and selectivity.

Although Al_2O_3 is the most commonly used promoter for methanol synthesis catalysts, ZrO_2 was also found to be active and therefore, effort has been put in studying and optimizing the synthesis procedures and performance of Cu/ZnO catalysts promoted by Zr. (RAUDASKOSKI et al., 2007) prepared $Cu/ZnO/ZrO_2$ samples in order to understand the effect of ageing time of the coprecipitation method. Characterization of the materials suggests that longer ageing time results in higher BET surface area and smaller CuO and ZnO crystallite size, while ZrO_2 peaks were not detected by XRD, indicating high dispersion. Accordingly, CO_2 conversion and methanol selectivity were found to increase with ageing time during the catalyst synthesis.

Dong et al. (2016) evaluated the characteristics and catalytic performance of $Cu/ZnO/ZrO_2$ catalysts reduced by $NaBH_4$ by comparing the results with a conventional ZrO_2 promoted material without the reducing agent. Even though the presence of $NaBH_4$ reduced BET and Cu surface areas, the samples presented improved thermal stability and reducibility and smaller Cu crystallite size. Regarding performance, in all temperature conditions studied, the reduced samples showed higher methanol selectivity than the conventional catalyst. The optimum catalyst found in terms of methanol yield was the sample with $NaBH_4$/Cu molar ratio of 5. CO_2 conversion was not significantly altered by the addition of the reducing agent.

Using a novel reverse coprecipitation synthesis method, (ARENA et al., 2007) synthesized ZrO_2 supported Cu/ZnO catalysts with varying Zn/Cu atomic ratios and fixed zirconia loading. The data provided indicates that Zn/Cu of 0,3 - 0,4 leads to the optimum material properties, such as BET surface area, pore volume and Cu

dispersion. The authors suggest that low Zn/Cu ratios may cause agglomeration of Cu particles while higher ratios might decrease the stabilization of Cu^{+1} sites on the ZrO_2 cavities. Although the catalytic tests were performed at low temperature conditions (160 - 200 °C), the catalysts with the Zn/Cu ratio mentioned previously presented methanol selectivity higher than the commercial $Cu/ZnO/Al_2O_3$ both at 10 and 30 bar. Given the low temperature employed, selectivity values obtained were in the range 50 - 90% while CO_2 conversion varied from 1 to 7%. Also, at 200 °C, the commercial catalyst presented higher conversion, while the synthesized materials showed improved selectivity.

Furthermore, several authors have studied the usage of other components with Cu/ZnO catalysts. (TOYIR et al., 2001) evaluated the effect of Ga and SiO_2 supported catalysts using the incipient wetness impregnation synthesis method with low weight % of copper. The smallest Cu crystallites were observed in the samples containing silica, suggesting that SiO_2 had a positive effect on the metal dispersion. The catalysts promoted by silica also presented higher methanol productivity compared to the Ga containing materials. However, the highest performance was observed in the test with a catalyst promoted both by hydrophobic SiO_2 and Ga (Cu-Zn-Ga/SiO_2), in which the authors obtained 5.6% CO_2 conversion and 99% methanol selectivity at reaction pressure of 20 bar and temperature of 270 °C. Additionally, the material presented stability over 80 h reaction time. The results indicate a positive interaction between silica, gallium and the conventional Cu/ZnO catalyst.

More recently, the use of bimetallic Pd-Cu catalysts has been reported (JIANG et al., 2015). In an extensive work, the authors synthesized catalyst containing single Cu or Pd metals, as well as materials containing both components, palladium and copper ratio were varied, as was the synthesis procedure. The supports used were highly porous materials. The results indicate that the coimpregnation method promotes the formation of alloys, while sequential impregnating the metals resulted in unalloyed phases as well. It was observed that the effect of Pd/(Pd+Cu) ratio on methanol formation is a volcano-shaped curve, with maximum at ratio of 0.34, in which the material presented highly dispersed PdCu alloys. The authors suggest that alloys may adsorb weakly-bonded hydrogen, promoting the hydrogenation of the intermediate formate species to methoxide, a slow step in the reaction mechanism. It was also suggested that alloys might enhance CO_2 chemisorption, however, more study is required on this regard. It can be observed that the exact behaviour of active sites in bimetallic alloyed catalysts is also not yet fully understood, and so studies on this subject are relevant.

Apart from the examples cited so far, the review paper by Saeidi et al. brings a summary of different Cu/ZnO catalyst as well as materials containing other elements and experimental conditions over the conversion and selectivity of CO_2 hydrogenation to Methanol (SAEIDI et al., 2014). The results are further summarized in Table 2.7. The experimental data provided highlights the effort that has been put in developing catalysts for the CO_2 hydrogenation to methanol over the years. Therefore, as mentioned previously, even though the reaction has been extensively studied, research on the development of catalysts is still relevant to optimize the performance, reduce costs and understand the role of active sites.

Table 2.7 - Summary of different catalysts effect over CO_2 conversion and selectivity to Methanol.

Catalyst	T(°C), P(bar)	X_{CO_2}[%]	S_{MeOH}(%)
$Cu/Zn/Ga/SiO_2$	270, 20	5.6	99.5
Cu/Ga/ZnO	270, 20	6.0	88.0
Cu/ZrO_2	240, 76	6.3	48.8
$Cu/Ga/ZrO_2$	250, 20	13.7	75.5
$Cu/B/ZrO_2$	250, 20	5.6	99.5
Cu/B/Cr	170, 50	25.9	72.9
$Ag/Zn/ZrO_2$	220, 80	2.0	97.0
$Au/Zn/ZrO_2$	220, 80	1.5	100
$Cu/Zn/ZrO_2$	220, 20	12.0	71.1
$Ag/Zn/Al/ZrO_2$	240, 20	18.7	47.2
Pd/Zn/CNTs	250, 20	6.3	99.6
$LaCr_{0,5}Cu_{0,5}O_3$	250, 20	10.4	90.8

Source: Saeidi et al. (2014).

The direct DME synthesis from CO_2 hydrogenation requires a bifunctional catalyst, which must perform two reactions in one step: methanol synthesis and then methanol dehydration to DME. The catalyst must include an active metallic component for the methanol synthesis and also an acid component for its posterior dehydration. Utilization of such catalysts were first reported for the DME production from synthesis gas, later it was shown that the same hybrid catalysts employed in the synthesis from syngas were also active for the CO_2 hydrogenation to DME. The bifunctional catalysts can be prepared by two different procedures, a physical mixture or an integrated mixture (ALVAREZ et al., 2017).

In a physical mixture, the metallic and the acid components are mixed using dry powder mixing or grinding, therefore the two types of active sites of the new catalyst,

namely the sites for methanol synthesis and the acid sites for methanol dehydration are well separated. Even though $\gamma{-}Al_2O_3$ is often suggested as a component for the dehydration process catalyst due to its acidity and high surface area, (XU et al., 1997) reported that the water produced in CO_2 hydrogenation decreases its activity, most likely due to its hydrophilic nature and acidity. The authors also found that the HZSM-5 zeolite (an aluminosilicate zeolite belonging to the pentasil family of zeolites) presented mainly Brønsted acid sites while γ-Al_2O_3 contains Lewis acid sites, which caused the negative effect of water to be less expressive on the zeolite. This effect has driven many researchers to study the combination of HZSM with variations of the commercial Cu/ZnO methanol synthesis catalyst, some of them reaching high DME selectivity and CO_2 conversion. Wengui et al. prepared several physically mixed $CuO{-}ZnO{-}Al_2O_3{-}La_2O_3$/HZSM5 catalysts with different La loadings for direct CO_2 hydrogenation to DME, showing that an amount of La up to 2% increases acidity and has a positive effect on the catalyst performance, achieving 43.8% CO_2 conversion and 71.2% DME selectivity (WENGUI et al., 2013).

On the other hand, integrated mixtures purposely have the active components for the two reactions closely placed, aiming to facilitate DME synthesis. These catalysts are prepared in a single synthesis procedure, by adding the methanol synthesis component over the acid catalyst using precipitation, impregnation or the hydrothermal method. HZSM-5 based acid catalysts have also been studied using the integrated mixture technique, combined with Cu based catalysts. A study reported 18.7% CO_2 conversion and high selectivity to DME (73.6%) using $CuO{-}ZnO{-}Al_2O_3{-}ZrO_2/HZSM-5$ bifunctional catalysts modified by Pd (SUN et al., 2004). By using a similar catalyst synthesis technique, Wang and Zeng studied the effect of alumina concentration on $Cu{-}ZnO{-}Al_2O_3{-}SiO_2$ catalyst and found that 10% Al_2O_3 content in the catalyst system results in approximately 12% CO_2 conversion and 40% selectivity toward DME (WANG; ZENG, 2005).

Aside from the choice of elements to compose an efficient catalyst for direct CO_2 hydrogenation to DME, the properties of the catalyst and support are also critical aspects. Features like crystallite size (metallic dispersion), surface area, thermal stability, reducibility and acidity have to be taken into account. Bonura et al. (BONURA et al., 2017) evaluated the performance of CuZnZr/ferrierite catalysts prepared through two different procedures, resulting in two different metallic dispersion patterns and metal-zeolite ratio. The results indicate that a higher metallic dispersion facilitates CO_2 activation, but also increases CO selectivity. Also, it reveals that the methanol dehydration to DME is favoured only in the presence of balanced acid

sites, whereas too high acidity promotes the reverse reaction instead. This conclusion is in agreement with a previous work (FRUSTERI et al., 2015a), in which the results also indicates that the CO_2 hydrogenation to DME requires a balance of basic sites to activate CO_2 and acid sites to perform methanol dehydration.

All copper based catalysts are prone to deactivation in continuous processes, which can occur due to thermal sintering, poisoning by sulfur or chloride species, coke deposition or even physical damage to the catalyst structure (TWIGG; SPENCER, 2001). Thermal sintering is the most common cause of deactivation of copper catalysts, both on industrial and laboratory contexts. It consists of crystallite growth on the support structure due to high temperature conditions, resulting in lower metallic surface area and therefore lower catalytic activity. Poisoning is defined as the strong chemisorption of unwanted reactants on active sites that would be available for the desired reaction. Given the high reactivity between Cu and sulfide species, it is important to ensure that not even trace amounts are present in the reaction. The reaction conditions may also cause the formation of inert phases, such as copper aluminates, impacting negatively the catalyst performance. Furthermore, thermal degradation of the support is also possible, and therefore the thermal stability of the material must be studied and the reaction temperature chosen accordingly (BARTHOLOMEW, 2001). Regarding the noble metal catalysts, Pd based catalysts are the most utilized due to high activity and selectivity to methanol. In comparison to the commercial $Cu/ZnO/Al_2O_3$ catalyst, increasing temperature and pressure improved selectivity to methanol and CO_2 conversion. Besides the Pd/ZnO catalysts, other systems such as Ag/ZnO and Au/ZnO have recently been studied and results show that noble metal and support interaction promotes higher activity and selectivity to methanol than the industrial copper based catalyst (YANG et al., 2017). However, noble metals are much more expensive and less abundant than Cu.

2.3.2.2 Carbon supported catalysts

As was observed, most of the research regarding the development of catalysts for the CO_2 hydrogenation reaction focuses on oxide-based supports, however, recently carbon materials have received attention as well. Properties such as surface area, porosity and hydrophobicity render carbon based materials potential supports for catalytic systems. In general, currently the materials most studied as supports for methanol synthesis are carbon nanotubes (CNTs), carbon nanofibers (CNFs) and graphene-based, while activated carbon (AC) and carbon black (CB) were used to a lesser extent.

In terms of stability in hydrogenation reactions, typical oxide supports may be modified by the byproduct H_2O, while carbon supports have shown to be stable due to the hydrophobic nature of the materials. Still, carbon may be converted into CH_4 and CO through methanation ($C + 2H_2 \rightarrow CH_4$), steam gasification ($C + H_2O \rightarrow CO + H_2$) and CO_2 gasification ($C + CO_2 \rightarrow 2CO$) and while these reactions hardly occur on pure carbon materials at the temperature range of hydrogenation, the addition of metal phases such as Cu and ZnO promote the effects. Therefore, removal of carbon during CO_2 hydrogenation is possible and may collapse the support structure. Nevertheless, it is established that amorphous carbons such as AC are more susceptible, while CNTs and graphene-based materials are less reactive to CO_2, H_2 and H_2O (FURIMSKY, 2020).

To evaluate the performance of highly dispersed Cu-Zn alloys on carbon supports, (GROSSMANN et al., 2015) prepared several CNTs supported catalysts, using different methods of functionalization and materials with varying inner diameter, while the active phases were introduced by impregnation. Thermal stress in oxidative atmosphere was used to functionalize O-CNTs (i.d. = 6 - 7 nm) and CNT-Py (i.d. = 50 nm) supports and CNT-A was modified by reflux in nitric acid. Methanol productivity over the materials was compared to a commercial catalyst. The structure obtained was different for materials prepared by different procedures, while the O-CNTs samples presented both agglomerates and smaller metal particles within nanotubes, in CNT-A the active phases were found in the external section and in CNT-Py, Cu and Zn were present in fibrous structures. Copper showed a heterogeneous particle size distribution and the exposed metallic area also varied between samples. The authors performed two series of catalytic tests, using two different reduction conditions: standard with 2% H_2 in He at 240 °C for 1 h and severe with 10% CO in H_2 at 400 °C for 30 min. While the commercial catalyst showed the best performance in both conditions in terms of methanol concentration, it was outperformed by the samples CuZnO/CNT-A and CuZnO/CNT-Py in terms of m^2 of Cu. It was noteworthy that the severe reduction condition was favorable to the commercial catalyst, which presented high copper content (50% wt.), while the standard procedure resulted in a better performance of the CNTs samples with highly dispersed nanoparticles, in fact CNT-Py was not active after being reduced in the more drastic approach. The results suggest that mild reduction conditions should be employed when pretreating catalysts containing nanoparticles. Furthermore, the O-CNTs samples presented poor methanol productivity in both conditions, indicating that this synthesis procedure may result in blocked active sites, as the active phases were found within the nanotubes.

Additionally, alternative active phases were also reported to be employed in the synthesis of CNTs supported catalysts for CO_2 hydrogenation. (LIANG et al., 2009) evaluated the activity of PdZn supported on Multi-Walled Carbon Nanotubes (MWCNTs) in comparison with the same materials supported on AC and γ-Al_2O_3, using the sequential wetness impregnation method to introduce the metal phases. In terms of CO_2 conversion and methanol yield, the optimal Pd/Zn molar ratio was 0,1, while PdZn loading quantity varied for each support. The optimized materials obtained were 16%PdZn/CNTs, 35%PdZn/AC and 20%PdZn/γ-Al_2O_3. Reaction and reduction temperature were also optimized to 250 °C and 500 °C, respectively. XRD analyses revealed the formation of the PdZn alloy after reduction in all catalysts, the diffractogram of the CNTs supported material also presented lines related to MWCNTs, indicating stability in a reducing atmosphere. Characterization performed showed significantly higher Pd dispersion in the CNTs material compared to the AC and γ-Al_2O_3 counterparts, while Pd surface area was only slightly improved. Regarding catalytic tests, the CNTs supported catalysts presented greater CO_2 conversion (6.30%) than AC (4.93%) and γ-Al_2O_3 (4.44%) as well as methanol STY, which was 37.1, 28.1 and 24.2 mg/h.g for CNTs, AC and γ-Al_2O_3, respectively. As the Turnover Frequency (TOF) for Pd^0 was also higher for the CNTs supported catalyst, the authors suggest that slightly improved surface area alone would not result in that much higher methanol STY, and so the nanotubes may have had a promoter action, possibly due to hydrogen spillover. The study suggests that for a PdZn active phase, CNTs might be a more appropriate support than a traditional aluminum oxide. Nevertheless, a comparison with the commercial $Cu/ZnO/Al_2O_3$ catalyst would be appropriate, also, in practical terms the total amount of Pd employed in the synthesis procedure would harshly increase the material production cost.

CNFs properties such as chemical stability, mechanical strength, high porosity and low tortuosity make the material a potential support for catalytic systems. However, studies on CuZnO supported on CNFs for CO_2 hydrogenation to methanol are scarce. In the attempt to develop a Cu based system supported on CNTs while evaluating the effect of ZnO, (DIN et al., 2019) synthesized 15Cu-15ZrO_2/CNFs catalysts with the addition of ZnO promoter in small quantities (1 - 4% wt. in the materials denoted CZCZ1 - CZCZ4, respectively). TEM images shows well dispersed catalytic phases on the fiber structures in the catalysts with ZnO content up to 3%, with particle agglomeration observed in the sample with 4%. Also, increasing ZnO content until 3% did not cause significant variation in BET surface area, which only decreased harshly for the CZCZ4 sample. A similar behavior was observed by N_2O

chemisorption, indicating that metallic Cu surface area, dispersion and relative distribution all decreased substantially when increasing ZnO %wt. beyond 3%. The authors were able to correlate the characterization results with the catalytic activity in terms of methanol STY, as the sample CZCZ3 presented the optimal value (45 g/kg.h), with methanol selectivity reaching 92% and 9% CO_2 conversion. It is noteworthy that the results were obtained in tests using a mild temperature of 180 °C. The performance was improved in comparison with other works using commercial catalysts and comparable with studies on conventional Cu/ZnO and Cu/ZnO/ZrO_2 systems with more drastic reaction conditions, which were reported in papers gathered by the authors. The innovative research demonstrates that CNTs are suitable supports for methanol synthesis, while optimizing ZnO content in a multi component system. Nevertheless, Cu based catalysts supported on CNFs still have much space for investigations.

Diez-Ramirez et al. (2016) studied the the formation and activity of PdZn alloys using two types of CNFs (fishbone and platelet), ZnO and Al_2O_3 as supports. Surprisingly, the authors identified reduced phases (Pd^0 and PdZn alloy) with XRD on the post-calcined CNFs supported catalysts, without a reduction step, an effect which was also observed on Cu/CNFs but not on Pd/Al_2O_3, suggesting that nanofibers alone could act as the reducing agent, forming metallic Pd and the alloy. Nevertheless, it was observed that the reduction step prior to the reactions still increased methanol production. While the reference catalyst Pd/CNFs was only selective toward CH_4, formation of PdZn alloys on the PdZn/CNFs catalysts successfully converted CO_2 to methanol, with Pd/Zn ratio and type of CNFs having an effect on production rate. It was observed that a decrease in Pd/Zn led to a better performance at higher temperatures (250 °C for Pd/Zn = 0.13), while increasing it resulted in smaller alloy particles and higher methanol selectivity at lower temperatures (200 °C for Pd/Zn = 0.75), effect attributed to highly active small particles producing CO at higher temperatures. The overall temperature effect was explained by the difference in the adsorption of reactants studied by Temperature Programmed Desorption (TPD). The optimal result was obtained using Pd/Zn = 0.13 supported on platelets CNFs at low temperatures. One of the highlights of the research it that all results were obtained at ambient pressure, indicating that CNFs supported materials may not require drastic conditions for methanol synthesis.

In comparison with the carbon materials cited, activated carbon (AC) has the advantage of low cost and availability, however, very few studies on AC supported catalysts for the CO_2 hydrogenation to methanol have been reported. (LUO et al.,

2020) prepared Cu-Zn catalysts supported on AC by incipient wetness impregnation. Two methods for fixating the active phases and removing precursor residue were employed, a novel cold plasma operation (catalyst denoted CZC-P) and conventional calcination under Ar flow (CZC-C). The CuO content on both materials was 20% wt. XRD analyses revealed that the cold plasma technique successfully synthesized the material, as the diffractograms obtained for the two samples were very similar. Microscopy images (SEM and TEM) indicated higher dispersion on the CZC-P sample, which was attributed to the lower temperature used in the synthesis, also, improved interaction between CuO and ZnO was observed in the plasma sample. The authors found these characteristic to be responsible for the significant improvement both in CO_2 conversion and methanol STY during the tests performed at 260 °C and 40 bar. The authors also performed in situ Diffuse Reflectance Fourier Transform Spectroscopy (DRIFTS) analyses to determine reaction intermediates and propose a mechanism for the CO_2 hydrogenation on the AC supported catalysts. The main intermediates observed were carbonate, bicarbonate, carbon ion, formate and methoxy, indicating that the hydrogenation proceeded through the formate pathway. The proposed mechanism is presented in Figure 2.7, hydrogen diffusion from Cu to ZnO occurs due to spillover, which rapidly converts bicarbonate to formate, then methoxy. At this point, methoxy may be further hydrogenated to methanol, or decomposed to form CH_4 and CO. The study shows its relevance with the development of low cost catalysts, novel synthesis procedures and mechanism.

Figure 2.7 - Proposed mechanism of CO_2 hydrogenation on CuZnO/AC catalyst.

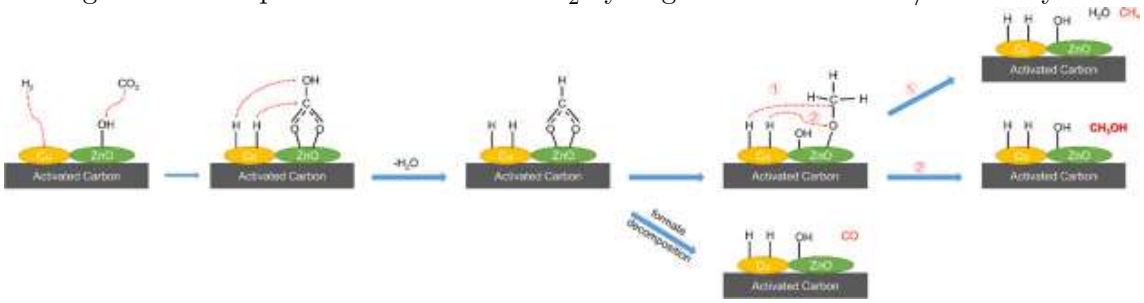

Source: Luo et al. (2020).

No studies on the usage of carbon black (CB) as a support for CO_2 hydrogenation catalysts were found, which indicates a possible research opportunity on the field. Similarly, research on DME production from CO_2 hydrogenation over carbon supported catalysts is also scarce. No studies cited so far address the use of graphene supported catalysts, as these shall be covered in the subsequent section of the review.

2.4 Graphene

Graphene denotes a flat carbon monolayer firmly packed into a two-dimensional (2D) honeycomb lattice, a basic building block for other dimensionalities graphitic materials. It can be wrapped up into 0D fullerenes (C_{60}), rolled into 1D nanotubes or stacked into 3D graphite, as shown in Figure 2.8. Even though graphene has been studied for approximately sixty years, only recently researchers realized that it also provides an excellent theoretical toy model for quantum electrodynamics studies, which gave rise to extensive research. Nowadays, graphene is currently being studied by several areas in order to have a better understanding of its properties and morphology, as well as applications (GEIM; NOVOSELOV, 2010).

Figure 2.8 - Graphene as the building block for graphitic materials.

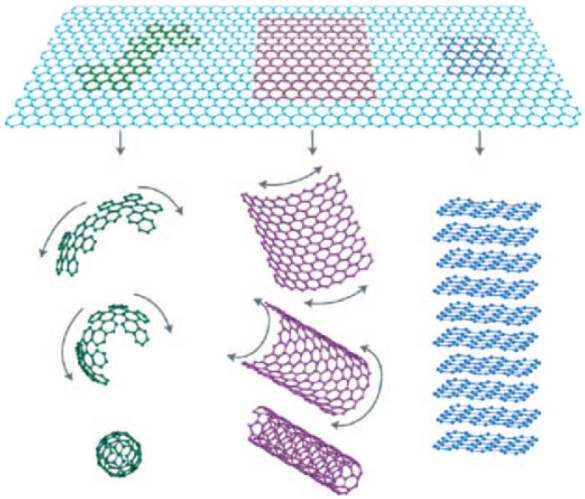

Source: Rao et al. (2009).

Over the past years, graphene has got increasing research interest in many areas, such as quantum mechanics, electronics and electrochemical. On the other hand, due to some specific properties, graphene, graphene oxide and reduced graphene oxide are getting attention in the catalysis field as well. Hence, this section reviews synthesis procedures and properties of graphene, focusing on catalysis applications.

2.4.1 Properties

Pristine graphene has several unique properties, such as high electron mobility ($\sim 10000\,\mathrm{cm^2V^{-1}s^{-1}}$) and thermal conductivity ($3000 - 5000\,\mathrm{W\ m^{-1}K^{-1}}$) at room temperature, white light absorbance of 2.3% with negligible reflectance and theo-

retical specific surface area of $2630\,m^2g^{-1}$ for single-layer graphene (SG) (RAO et al., 2010). Also noteworthy is the excellent chemical stability and mechanical strength of graphene sheets. These exceptional features have made graphene rise as an outstanding free-metal catalyst and 2D support for a wide range of catalytic reactions. Even so, the majority of applied studies have been performed by using the less expensive and more available graphene oxide (GO) and reduced graphene oxide (rGO). Oxidation and/or reduction significantly alter the physical structure of graphene by introducing defects and functionalities, which may provide good dispersibility in solvents, contributing to better catalytic performance of graphene-based catalysts and supports (MACHADO; SERP, 2012).

Figure 2.9 presents schemes for the structures of Graphene, GO and rGO. The foundation of the graphene structure are strong σ bonds, which form the honeycomb configuration, and π bonds mediate the interaction between different layers. This conformation makes graphene a promising electron conductor, since it allows delocalized π electrons to be easily conducted. The electronic properties, as well as the thermal conductivity and expansion of graphene vary with both the number of layers and the relative position of atoms in adjacent layers. This affects the properties of GO due to the presence of oxygenated surface groups and structural defects (Figure 2.9), causing a substantial loss in conductivity. To restore conductivity, the GO layers must be reduced, and depending on the reduction level, the surface can be fine-tuned in order to attain different electronic and optoelectronic features (MACHADO; SERP, 2012).

Figure 2.9 - Graphene, GO and rGO structure schemes in rGO synthesis.

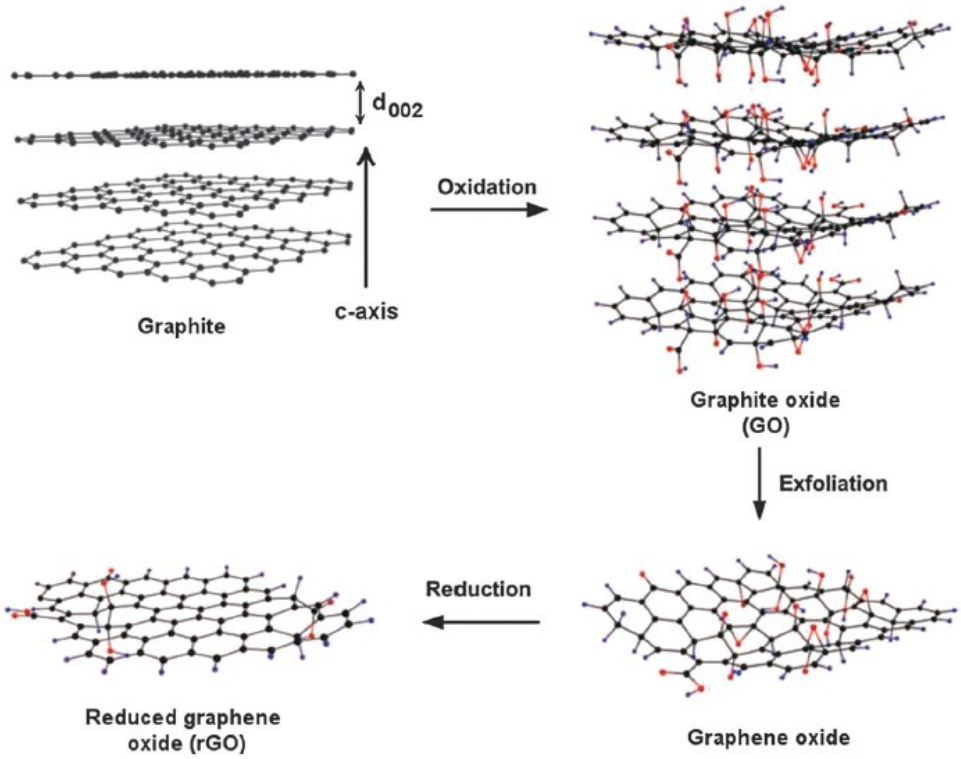

Source: Machado and Serp (2012).

One of the most important properties of graphene for catalysis applications, in particular for CO_2 hydrogenation, is adsorption of metals. Understanding the adsorption mechanism and the interaction between the adsorbed species and the carbon atoms is crucial to graphene-based materials synthesis. The adsorption sites of a graphene layer are represented in Figure 2.10, where an (H) site is at the center of a hexagon, a (B) site is halfway between two carbon atoms and (T) is above a carbon atom. Nakada and Ishii (NAKADA; ISHII, 2011) conducted first-principles calculations based on Density Functional Theory (DFT) to determine the adsorption energy for nearly all possible adsorbed atoms (adatoms). The results indicated in Figure 2.11 show the most stable adsorption site and bond energy for each element, H6 sites represents the H sites mentioned previously. The highlighted elements in bold rectangles showed a bond distance to graphene of less than 2.0 Å, indicating strong adsorption. The study shows that for the majority of transition metals (with a few exceptions such as Cu) the most stable is the H adsorption site, for nonmetallic elements the B sites have the most stability and the T site is only the most stable for a few species. Also, the bond energy for most transition metals and nonmetallic elements such as

C, N and O are very high. Regarding the bond distance between graphene and the adatom, large distances tend to reduce the binding energy, showing a similar behavior to physical adsorption. On the other hand, the bold highlighted species present a bonding feature similar to chemical adsorption (NAKADA; ISHII, 2011).

Figure 2.10 - Graphene adsorption sites.

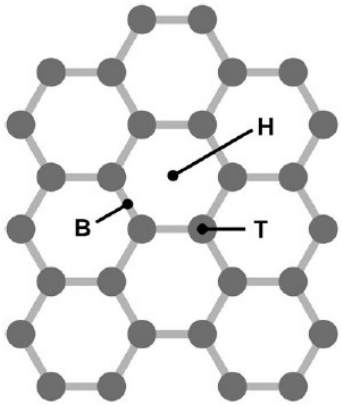

Source: Machado and Serp (2012).

Figure 2.11 - Most stable graphene adsorption sites and bond energy for several elements.

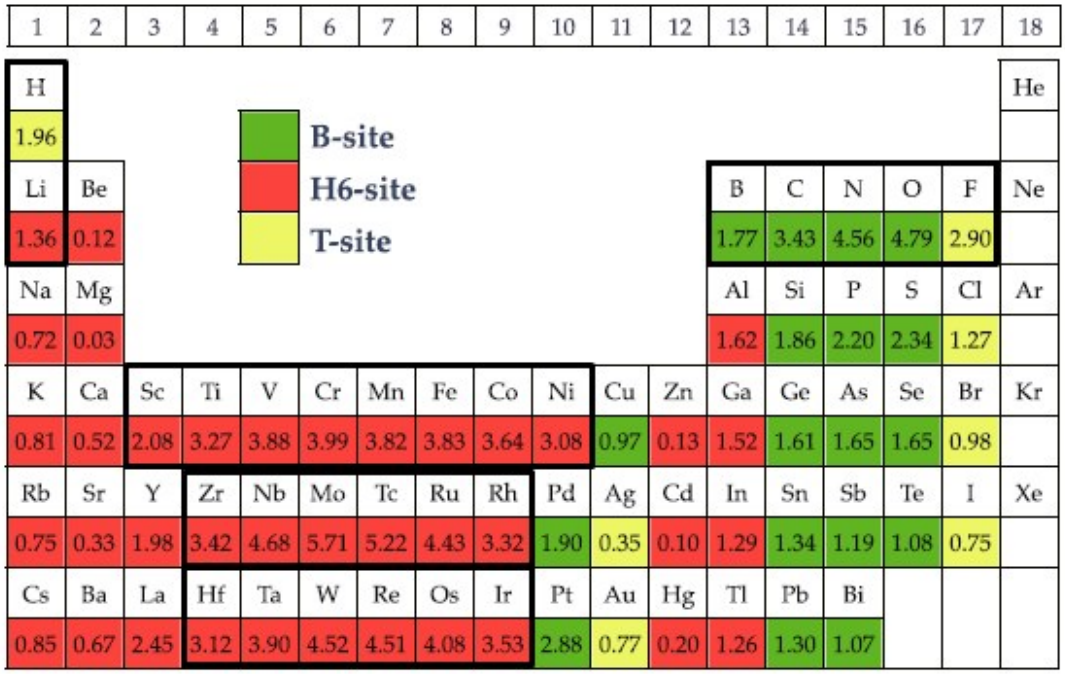

1	2	3	4	5	6	7	8	9	10	11	12	13	14	15	16	17	18
H																	He
1.96																	
Li	Be											B	C	N	O	F	Ne
1.36	0.12											1.77	3.43	4.56	4.79	2.90	
Na	Mg											Al	Si	P	S	Cl	Ar
0.72	0.03											1.62	1.86	2.20	2.34	1.27	
K	Ca	Sc	Ti	V	Cr	Mn	Fe	Co	Ni	Cu	Zn	Ga	Ge	As	Se	Br	Kr
0.81	0.52	2.08	3.27	3.88	3.99	3.82	3.83	3.64	3.08	0.97	0.13	1.52	1.61	1.65	1.65	0.98	
Rb	Sr	Y	Zr	Nb	Mo	Tc	Ru	Rh	Pd	Ag	Cd	In	Sn	Sb	Te	I	Xe
0.75	0.33	1.98	3.42	4.68	5.71	5.22	4.43	3.32	1.90	0.35	0.10	1.29	1.34	1.19	1.08	0.75	
Cs	Ba	La	Hf	Ta	W	Re	Os	Ir	Pt	Au	Hg	Tl	Pb	Bi			
0.85	0.67	2.45	3.12	3.90	4.52	4.51	4.08	3.53	2.88	0.77	0.20	1.26	1.30	1.07			

Source: Nakada and Ishii (2011).

Regarding CO_2 hydrogenation, the study indicates that many metal species can be adsorbed in graphene with good stability. Also, due to the high binding energy and short bond distance of O species, metal oxides can also be adsorbed in graphene sites.

2.4.2 Synthesis of graphene-based materials

Graphene layers can be blended with several components to form specific functionalities, this includes metals, metal oxides, polymers, small organic compounds, bio-materials and even other carbon nanomaterials. For heterogeneous catalysis, particular interest is given to metal and metal oxide components.

Most metal nanoparticles composites reported consist of noble metal particles such as Au, Pt, Pd and Ag, other metal nanoparticles of Fe, Cu and Ni were also used. There are many strategies used for synthesizing graphene materials with well dispersed metal nanoparticles, including a technique that consists of chemical functionalization of the graphitic surface, which promotes covalent bonds between the

metal and the graphene plane, resulting in high dispersion. Graphene oxide already possesses a large amount of functional groups, and can be chemically reduced along with the metal precursor to form the corresponding graphene-metal composite, this method was reported by many authors (MACHADO; SERP, 2012). Another reduction method reported by Hassan et al. (HASSAN et al., 2009) involves the reduction of the nanoparticles and GO simultaneously through microwave-irradiation (MWI). The advantage of this method is the uniform and quick heating of the mixture, being a potential method for efficient large-scale production of graphene-metal composites.

Several inorganic materials have been synthesized and supported on graphene structures, including ZnO, Al_2O_3, Cu_2O, CeO_2, TiO_2, MnO_2, Fe_3O_4, NiO and SiO_2. The main preparation methods for the graphene-metal oxide materials include sol-gel and the hydrothermal/solvothermal process. The sol-gel approach has the advantage of hydroxyl groups of GO/rGO layers acting as nucleation sites, resulting in chemically bonded metal oxide nanoparticles, and the hydrothermal method reduces GO to rGO promoting nanostructures with high crystallinity, not requiring post-synthetic annealing or calcination (MACHADO; SERP, 2012).

Regarding the synthesis of graphene oxide, the early method proposed by Hummers and Offeman (HUMMERS; OFFEMAN, 1958) still, to this day, serves as the basis for modern GO synthesis. The main objective of the method was reducing the synthesis time and explosion hazard from methods reported back then. The classic experiment consisted of stirring powdered graphite and $NaNO_3$ into H_2SO_4, then adding $KMnO_4$ under vigorous agitation. The suspension was then further diluted with warm water and treated with H_2O_2. Afterwards, it was filtered resulting in a yellow-brown filter cake. Finally, after washing the filter cake three times with water, the GO residue was dispersed in water to about 0,5% solids and the dry form was obtained by centrifugation followed by dehydration over phosphorus pentoxide (P_4O_{10}). The synthesis resulted in dried GO with Carbon-to-oxygen atomic ratio of 2.25, 23% water and 2% ash content (HUMMERS; OFFEMAN, 1958).

Over the years, modifications of the Hummers method were studied in the synthesis of graphene-based materials. Chen et al. (CHEN et al., 2013) proposed an eco-friendly improvement of the Hummers methodology whithout the use of $NaNO_3$, aiming to synthesize GO without releasing toxic gases such as NO_2 and N_2O_4 or producing Na^+ and NO_3^-, which are difficult to be removed from waste water formed in the process of synthesizing and purifying GO. The results are shown in Table 2.8, where GO1 and GO2 represents the samples produced by the modified and conventional

Hummers method respectively. The yield is calculated by the ratio of GO weight and graphite powder weight, it indicates that the method is able to oxidize graphite to GO without $NaNO_3$ with a small difference from the traditional method. The C/O atomic ratio was measured by X-ray photoelectron spectroscopy (XPS), showing that both samples are within the expected range for GO (2.1 - 2.9). The fourth and fifth columns indicate the peak intensities of intact carbon and oxygenated carbon respectively, confirming that the samples have similar oxidization degrees. Lastly, the zeta potentials indicate that both materials are negatively charged due to the presence of carboxyl groups. The study shows that removing a hazardous material from the synthesis procedure does not alter significantly the reaction product (CHEN et al., 2013). Other authors have used modified Hummers methods in GO synthesis, reporting potential graphene-based materials for catalysis applications (FRANCHINI et al., 2020; MARCANO et al., 2010; SHEN et al., 2011).

Table 2.8 - Comparison of GO samples produced by modified and conventional Hummers method.

	Yield (%)	C/O	C−C/C=C (%)	O (%)	ζ (mV)
GO1	92.0	2.36	47.9	52.1	-43.8
GO2	96.0	2.23	46.5	53.5	-45.6

Source: Chen et al. (2013).

Since the rise of interest in graphene research, many methods have been used to reduce graphene oxide to rGO, including chemical reduction and hydrothermal reduction, with the latter having a number of advantages over chemical reduction. The hydrothermal conversion requires a simple setup consisting of an autoclave and an oven, it has good scalability and is industrially compatible with batch processing and the degree of GO reduction can be controlled through temperature and pressure parameters. The process is also intrinsically pure as it only utilizes water, while hydrazine or sulfonate chemical reduction methods introduce impurities into rGO. On this subject, Ding et al. (DING et al., 2012) studied the influence of temperature, heating time and GO solution concentration on rGO synthesis by hydrothermal reduction through several characterization analysis. The results indicate that rGO can be obtained in water at GO concentration below 0.3 mg/mL, heating time in the range 2 h - 6 h and temperature higher than 160 °C with excellent dispersion. This method has been reported to successfully reduce GO to rGO by many authors (FRANCHINI et al., 2020; SHEN et al., 2011; ZHOU et al., 2009).

2.4.3 Heterogeneous catalysis applications

Graphene-based materials are promising catalyst supports due to their large surface area and chemical stability. The performance and activity of a catalyst critically depend on the interaction between the active phase and the support, in other words, it is expected that the chemical bond at the support-catalyst interface can be used to tune chemical and electronic properties of the active sites in order to obtain higher catalytic activity and selectivity to the desired products. Also, usually stronger support interaction with the catalyst promotes better dispersion and stability. Nevertheless, graphene is chemically inert due to strong sp^2 bonds between carbon atoms of a graphene layer, leading to weaker interaction with the supported metal cluster. Therefore, mechanical strains, structural defects and functional groups are usually introduced in order to promote stronger binding of catalyst species and graphene-based support. While this is generally achieved by using rGO as the catalyst support (FAN et al., 2015), other types of graphene-based materials have been used as supports and promoters as well.

To prevent sintering of metallic nanoparticles during catalytic CO_2 hydrogenation to CH_4, (WU et al., 2019) prepared Ni nanoparticles supported on microporous graphenelike carbon (MGC) catalysts. Incipient wetness impregnation was employed to introduce 5 - 20 % wt. of Ni on MGC. Raman spectra showed graphitic structure on the material, indicated by a high relative intensity of the G band. The catalytic tests performed at ambient pressure showed optimum CH_4 selectivity at 400 °C, decreasing with higher temperatures most likely do to RWGS reaction. XRD analysis of the spent catalysts did not present significant changes. The optimal Ni loading was 15%, achieving 50% CO_2 conversion and 2066 ($mg/g_{cat}h$) CH_4 STY. The stability of the catalyst was also tested and compared with Ni supported on AC and CB with same loading, the results show that the MGC material was stable over 30 h on stream maintaining 95% CH_4 selectivity, while the counterparts rapidly deactivated.

Even though most of the research regarding the use of graphene-based materials as supports and promoters for CO_2 hydrogenation targets methane as the desired product, the majority of the examples cited in this section focuses on methanol production.

Several Cu-ZnO-Al_2O_3 (CZA) cataysts promoted by nitrogen-doped graphene (NG) were synthesized by coprecipitation and employed in the CO_2 hydrogenation to methanol. Characterization showed that NG content up to 10% wt. improved properties such as BET surface area, metallic dispersion and Cu exposed surface area,

while also resulting in smaller crystallite size. On the other hand, exceeding 10% had a negative effect on the same properties, effect which was attributed to NG stacking and covering the CZA phase due to exceeding content. The Raman spectra obtained showed no significant difference between fresh NG and the catalysts prepared, demonstrating that the high level of defects (indicated by high intensity ratio of D and G bands) were maintained during the synthesis procedures. Accordingly to the characterization results, catalytic activity also presented optimal performance with the 10NG-CZA sample (8.2% CO_2 conversion and 84% CH_3OH selectivity). The authors state that NG had the roles of support, providing surface area for CZA and promoter, improving H_2 adsorption and spillover. While the negative effect of higher NG content was related to stacking, NG weight lower than 10% might have provided insufficient surface area, causing agglomeration of CZA and poor Cu dispersion. Additionally, a stability test was performed, showing that the 10NG-CZA catalyst maintained conversion and selectivity during approximately 50 hour on stream (MA et al., 2019).

Graphene oxide is a 2D network of variable concentrations of sp^2 and sp^3 carbon, possessing hydroxyl and epoxy functional groups on the base layer and also lactol, ester carbonyl and ketone groups at the edges of defects, these groups render GO an acidic and strong oxidizing nature. Additionally, the amphiphilic nature (possesses both hydrophilic and lipophilic properties) and excellent dispersibility of GO causes its surface to be more accessible to precursors which in turn enhance accessibility of catalytically active species. Even though most hydroxyl and epoxy functional groups are removed in the GO reduction process, highly stable carbonyl and ether groups remain at the edges and most defects are still observed in the basal plane. Furthermore, sulfate groups and other heteroatom-containing functionalities introduced by adsorption during the Hummers synthesis of GO may be present in trace amounts. The ensemble of these functionalities, edges, topological defects and electronic features contribute to the catalytic activity of rGO. Nonetheless, the presence of functional groups and defects in GO and rGO will substantially alter electron transfer with catalytically active species, thus graphene and rGO based catalysts may present differences in catalytic performance in applications such as electrocatalysis (FAN et al., 2015).

Many authors have reported the synthesis of rGO-supported catalysts with interesting results. Using a modified Hummers method to obtain GO and posterior hydrothermal reduction to rGO, (FRANCHINI et al., 2020) produced $Pd/CeO_2{-}rGO$ and Pd/rGO catalysts. The results indicate high dispersion of CeO_2 on the rGO surface

and that ceria, in turn, has a remarkable promoting effect on Pd dispersion. Shen et al. (SHEN et al., 2011) reported an environmental friendly efficient route for the synthesis of TiO_2/rGO sheets, the method consists in using glucose as the reduction agent of the hydrothermal synthesis, while GO was obtained from the modified Hummers method as well. The process also shows simplicity, low cost, high productivity and reduced processing time. Furthermore, Sun et al. (SUN et al., 2013) proposed an efficient procedure to synthesize a rGO-carbon nanotube (CNT) composite to support Pd nanoparticles, resulting in a Pd/rGO/CNT catalyst. The method consisted of obtaining GO by the modified Hummers method, then hydrothermal reducting an aqueous dispersion of GO and CNT forming macroscopic rGO-CNT cylinder hydrogels, followed by dipping of the resulting composite in a K_2PdCl_4 solution. The catalyst presented high catalytic recycling stability, the results presented in Table 2.9 compare the reaction time for five cycles of the catalytic aqueous redox reaction of 4-NP to 4-AP by $NaBH_4$ using Pd/rGO/CNT, Pd/rGO and Au/C core-shell catalysts. The results indicate that the Pd/rGO/CNT catalyst presents higher recycling stability than the Pd/rGO catalyst and the shortest reaction time among the analysed composites, an indicative of high catalytic activity.

Table 2.9 - Comparison of the catalytic recycling stabilities of composites.

	Cycle				
Catalyst	1st	2nd	3rd	4th	5th
Pd/rGO	30 s	120 s	180 s	190 s	210 s
Pd/rGO/CNT	20 s	30 s	35 s	40 s	40 s
Au/C core-shell	300 s	300 s	300 s	300 s	300 s

Source: Sun et al. (2004).

Regarding the CO_2 hydrogenation reaction, a few authors have reported the synthesis, characterization and catalytic tests using rGO supported catalysts with interesting results. All authors synthesized GO from modified Hummers method, while reduction was carried out by different procedures. All materials consist of some form of Cu supported on rGO. The catalysts were tested in the selective CO_2 hydrogenation towards methanol. As of 2021, no papers were found on the use of graphene supported catalysts for DME production.

By using chemical reduction with hydrazine and the incipient wetness impregnation method, (DEERATTRAKUL et al., 2016) synthesized Cu−Zn/rGO catalysts with different metal loadings. The reduction of GO to rGO as well as the presence of CuO

and ZnO phases were confirmed both by XRD and Raman spectroscopy. Fourier Transform Infra-Red (FTIR) analysis indicated that the structure of rGO and the catalysts were not altered by calcination at 350 ºC. This result was further confirmed by TGA, in which the major mass losses occurred at 450 and 600 ºC. Temperature Programmed Reduction (TPR) measurements revealed that the reduced catalysts presented Cu^0, Zn^0 and ZnO species. The higher catalytic performance was obtained using 0,25 g of 10%Cu−Zn/rGO, the reaction was carried out at 250 ºC, 15 bar, GHSV = 2400 h^{-1}, 3:1 molar H_2/CO_2. Reduction was performed at 350 ºC for 2 h with 40 mL min^{-1} H_2 flow. The results obtained were 26% CO_2 conversion, 5,1% methanol selectivity and 424 ($mg/g_{cat}h$) Space Time Yield (STY) of CH_3OH.

Additionally, the authors also reported a study on the effect of reduction time in the step prior to the catalytic tests using in situ X-ray Absorption Near Edge Structure (XANES) spectroscopy. In this case, rGO was doped with N using hydrazine, so the system employed was 10%Cu-Zn/N-rGO. The reduction temperature was 350 °C and reduction time was tested from 30 to 180 minutes. By the observations of XRD analyses of the spent catalysts, along with the XANES spectra, the authors found that 90 min reduction time was the optimal condition, as the copper oxidation state was closer to 0 than for shorter times, while longer times aggravated sintering of the metal. Accordingly, the catalytic tests at the optimized condition resulted in 30% CO_2 conversion and a remarkable methanol STY of 591 ($mg/g_{cat}h$), a drastic increase compared to the results reported previously. The effect was attributed only to reduction time, as the activity of the N-rGO support was found to be negligible (DEERATTRAKUL et al., 2017).

The same group later reported the effect of temperature on the reduction of GO to rGO by the hydrothermal reduction method, finding 140 ºC to be the optimal condition. The rGO aerogel was then freeze-dried. The catalysts were prepared by wetness impregnation as well. The best result was obtained using 0.15 g of 15%Cu−Zn/rGO, the reaction and reduction conditions were similar to the previous study. The results obtained were 10.3% CO_2 conversion and 94.53 ($mg/g_{cat}h$) STY of methanol (DEERATTRAKUL et al., 2018). In both experiments, the total reaction time was 5 h, longer tests would be required in order to assess the long-term stability of the materials.

Employing the co-precipitation method with vitamin C to reduce GO, (FAN; WU, 2016) synthesized CuO−ZnO−ZrO_2−Al_2O_3/rGO (CZZA/rGO) catalysts containing 20% and 80% weight of CZZA and GO, respectively. The characterization indicated

that the CZZA/rGO catalyst had higher surface area compared to CZZA. The reaction was performed using 0.8 g of the catalysts, with temperature in the range 200 - 280 ºC, pressure from 10 to 20 bar, GHSV = 6075 - 10935 h^{-1} and 3:1 molar H_2/CO_2. The catalysts were reduced at 250 ºC for 2 h under 100 mL min^{-1} of $10\%H_2/N_2$ flow. The optimal reaction conditions resulted in 14.7% CO_2 conversion and 11.6% CH_3OH yield. XRD analyses were performed before and after the reaction, the diffractograms indicate that the structure and oxidation state of the metal on the material were preserved during the reaction.

Similarly, (WITOON et al., 2018) studied the effect of GO in $CuO{-}ZnO{-}ZrO_2$ catalysts prepared by reverse co-precipitation with different GO content. For the catalytic tests, 0.25 g of the material was diluted in 0.75 g of silica sand. Reduction was conducted at 300 ºC for 4 h under 60 mL min^{-1} of H_2 flow. The reaction conditions were: T = 200 - 280 ºC, P = 20 bar, the reactant was 65 mL min^{-1} of a 3:9:1 (CO_2:H_2:N_2) mixture. For all catalysts, with temperature rise, CO_2 conversion increased and CH_3OH selectivity and STY decreased. The highest conversion was obtained using the catalyst with 2.5% GO content, while the highest methanol selectivity and STY were obtained using the material containing 1.0% GO. GO content higher than 2.5% resulted in performance lower than the GO-free catalyst. The highest STY result obtained ($\sim$280 $mg/g_{cat}h$) was at T = 240 ºC. The authors also performed stability tests, using the same reactions conditions, with 96 h time-on-stream, the results revealed constant methanol STY, and a decrease in CO STY.

Furthermore, in order to prevent agglomeration of graphene layers caused by drastic oxidation and reduction conditions, the addition of surfactants was reported in the synthesis of TiO_2/rGO photocatalysts using the hydrothermal method (HU et al., 2017). The authors evaluated morphological and structural changes and photocatalytic activity by introducing the surfactants Triton X-100, sodium dodecyl benzene sulfonate (SDBS) and cetyl trimethyl ammonuim bromide (CTAB). Scanning Electron Microscopy (SEM) and High Resolution Transmission Electron Microscopy (HRTEM) images showed that the sample without any surfactant was harshly aggregated, while for the samples with surfactant, a monolayer was observed. The BET surface area also increased with all surfactants. Raman spectroscopy results indicate that the surfactant-free catalyst presents fewer functional groups and defects. The photo-catalytic activity was also improved by the usage of surfactants.

3 METHODOLOGY

3.1 Supports and catalysts synthesis

3.1.1 Graphene oxide synthesis

The graphene oxide (GO) synthesis was performed following a modified Hummers method proposed by (MARCANO et al., 2010) with slight modifications. Firstly, a mixture of concentrated acids H_2SO_4/H_2PO_4 (360:40 mL) (Sigma-Aldrich) were mixed with 3 g of Flake Graphite (Sigma-Aldrich) in a reactor, followed by the slow addition of 18 g of $KMnO_4$ (Sigma-Aldrich). The system was kept under stirring and room temperature for 24 h. The reaction temperature was then increased to 50 °C and maintained for 4 h. Temperature control was done by an ultra-thermostatic water bath. After the system was cooled to room temperature, 400 mL of ice and 8 mL of a 30% H_2O_2 (Sigma-Aldrich) solution were added. Subsequently the mixture was filtered and the solid washed with distilled water, 10% HCl (Sigma-Aldrich) aqueous solution and ethanol two times to remove metallic ions. Finally, the solid was washed with deionized water and centrifuged at 16000 rpm several times until it reached a pH of 5.5. After each centrifuge cycle, the water content was removed from the suspension. Finishing the process, a resulting dark brown gel which consists of GO was obtained.

3.1.2 Reduced graphene oxide synthesis

The reduced graphene oxide (rGO) synthesis was carried out by sonicating 40 mL of GO in an ultrasound bath for 2 h. Then the GO water dispersion was put in a teflon-lined autoclave, sealed and maintained at 180 °C for 17 h. The obtained rGO consisted in a black-colored cylinder immiscible in the residual water. The solid was removed from the residue and submerged in ethanol for three days straight changing the solvent daily. Finally, the material was dried at room temperature. The resulting sample was denoted as rGO_S.

In the attempt to maintain the structural properties of rGO after the drastic hydrothermal reduction conditions, two additional rGO samples were also synthesized following the exact same procedure described, but with the addition of surfactants before the ultrasound step. For rGO_P, Pluronic F127 surfactant was added to the mixture and for rGO_T, Triton X-100 (Sigma-Aldrich) was used.

3.1.3 Supports synthesis

The hybrid supports Zn−rGO were also prepared through the hydrothermal synthesis procedures described previously, with the addition of the Zn promoter precursors. The quantity of the promoter was calculated in order to result in catalysts with 10% Zn content. The precursor utilized was $Zn(NO_3)_2 * 6\,H_2O$ (Sigma-Aldrich). Firstly, for the hybrid supports synthesis the precursor salt was dissolved in distilled water, making a 10 mL volume with the required quantity to achieve 10% of Zn content in the resulting support. The salt solution was added to a GO solution (for Zn−rGO_P and Zn−rGO_T samples, Pluronic F-127 and Triton X-100 were also added, respectively), mixed until homogenized and kept in an ultrasound bath for 2 h before the hydrothermal synthesis. Afterwards, the mixture was poured into a Teflon reactor, which was sealed, inserted into the autoclave and isolated. The autoclave was placed into an oven with forced air circulation at 180°C for 17 h. After the hydrothermal procedure, the autoclave was cooled to room temperature, the solid was filtered and washed with ethanol.

3.1.4 Catalysts synthesis - one-step hydrothermal route

In this work it is proposed a novel one-step hydrothermal GO reduction for the synthesis of the Cu@Zn-rGO catalysts by introducing two metal phases simultaneously. The innovative aspect is the insertion of two metal phases in the sample, resulting in a complete catalytic system prepared in a single step, which has not been reported previously in the synthesis of rGO-supported catalysts for CO_2 hydrogenation. The synthesis procedure was carried out similarly to the previous item (Section 3.1.3), with the addition of Cu. The catalysts were prepared in order to obtain 10% of Cu and 10% of Zn in weight content in the final catalyst. Firstly, for the hydrothermal synthesis of the catalysts, the Cu precursor salt $Cu(NO_3)_2 * 3\,H_2O$ (Sigma-Aldrich) and the Zn precursor salt were dissolved in distilled water separately, achieving a volume of 10 mL each. The aqueous solutions containing the salts were then added a GO solution (for the Cu@Zn−rGO_P and Cu@Zn−rGO_T catalysts, Pluronic F-127 and Triton X-100 were added, respectively), homogenized and kept in an ultrasound bath for 2 h before the hydrothermal procedure. Subsequently, the mixture was poured into a Teflon reactor, which was isolated and inserted into the autoclave reactor. As described previously, the system was kept into an oven with forced air circulation at 180°C for 17 h. Finally, the autoclave was cooled to room temperature and the solid filtered and washed with ethanol.

Using the hydrothermal route, the catalysts Cu@rGO were also synthesized with

10% weight of Cu in order to evaluate the catalytic activity without the promoter species.

3.1.5 Catalysts synthesis - wetness impregnation method

The Cu/Zn−rGO catalysts were prepared by wetness impregnation of Cu onto the Zn−rGO hybrid supports described previously (Section 3.1.3). The quantity of the metallic precursor was calculated in order to obtain final catalysts with 10% weight of Cu. The method consists in placing the metal-containing solution in contact with the solid. In this procedure, the solution volume has to be equal the required quantity to fill the pore volume of the support, which must be previously determined by N_2 physisorption or through the wet point technique. In this case, the pore volume was determined experimentally using the wet point technique, which consisted in keeping 0.1 g of the support in an oven at 100 °C for 30 min to completely remove the water content. After drying, the sample was cooled in a desiccator with silica gel. After reaching the room temperature, water was slowly added to the sample in droplets. With the addition of each droplet, the material was homogenized and this procedure was repeated until the sample started to lose its powder form and became slurry. The wet point is the solution volume corresponding to the last droplet in which the solid is still powder and, therefore, it is given in mL/g. With the wet point determined, an aqueous solution containing the precursor $Cu(NO_3)_2 * 3\,H_2O$ was prepared with the exact volume required to fill the pore volume of the corresponding support mass. Similarly, the impregnation was carried out by slowly adding droplets of the solution on the solid support. As the droplets were added, the solid and liquid phases were physically mixed until homogenization. Afterwards, the sample was kept in desiccator with silica gel overnight. Finally, the sample was thermally treated at 300 °C (5 °C/min) under 40 mL/min synthetic air flow for 2 h.

Using the same synthesis procedure, the reference catalyst Cu/ZnO was also prepared. Firstly, $Zn(NO_3)_2 * 6\,H_2O$ (Sigma-Aldrich) was calcined at 500 °C (5 °C/min) to obtain ZnO, which is the catalyst support. Then the support pore volume was determined by the wet point method. The solution containing copper was added in droplets until the pores were completely filled. The resulting catalyst was thermally treated at 350 °C (5 °C/min) under 40 mL/min synthetic air flow for 2 h.

Firstly, the reference Cu/ZnO catalysts was prepared with calcination at 350 °C. However, after impregnating the Cu/Zn-rGO catalysts, a thermogravimetric analysis was performed to assess the maximum temperature in which the calcination step could be performed in order to prevent major mass loss. As the main loss occurred

at 350 °C, the temperature chosen for calcination was 300 °C.

3.2 Catalysts characterization

3.2.1 N_2 physical adsorption

The specific surface area of the reference support and catalyst (namely ZnO and Cu/ZnO respectively), as well as the commercial $Cu/ZnO/Al_2O_3$ catalyst was determined by N_2 physisorption analysis at -196 °C on a Micromeritics ASAP 2020 (Fig 3.1). Before the N_2 adsorption analyses, the catalysts were outgassed at 300 °C for 2 h. The specific surface areas were determined by applying the BET formalism to the collected data.

Figure 3.1 - Micromeritics ASAP 2020.

Source: Author.

3.2.2 Methylene blue adsorption

BET theory is appropriate for the analysis of nonporous, macro and mesoporous materials, however, graphene based catalysts potentially contains micropores. Therefore alternative methods must be employed in the determination of the specific surface area, such as the adsorption of dopamine or methylene blue (MB), which have been reported in the analysis of graphene materials (CHEN et al., 2020; ARIAS et al., 2020).

In this study, the specific surface area was determined by adsorption of methylene blue (MB) using linearization of the Langmuir isotherm. The procedure consisted in adding 15 mg of the material to 10 mL of MB solutions at different concentrations: 25, 100, 200, 500 and 1000 mg/L under 800 rpm magnetic stirring and keeping at this condition for 24 h. The resulting solutions were centrifuged for 30 min at 5000 rpm in order to separate the solid materials from the liquid phase. The final concentrations were then read by Ultraviolet-visible spectroscopy (UV-Vis) using wavelength of 663 nm. The equipment used was the UV-M51 Spectrophotometer (BEL Photonics) shown in Figure 3.2 with 10 mm Quartz cuvettes.

Figure 3.2 - UV M-51 BEL Photonics. Source: Author

Source: Author.

3.2.3 Thermogravimetric Analysis (TGA)

In this study, the thermal stability evaluation was carried out using a TA-Analyser STA 443 Jupiter (Netzsch) (Fig 3.3). The experiments were conducted under synthetic air atmosphere with total flow of 100 mL/min, with programmed temperature increase from 30 to 800 °C (10 °C/min).

Figure 3.3 - TA-Analyser STA 443 Jupiter TG.

Source: Author.

3.2.4 X-Ray Diffraction (XRD)

The X-Ray diffractograms were collected in a Panalytical Empyrean diffractometer (Fig 3.4) using Cu radiation source (CuKα = 1.5405Å), with 2θ varying from 8 to 90 ° and 2θ step of 0.02.

Figure 3.4 - Panalytical Empyrean.

Source: ASMAI (2021).

3.2.5 Scanning Electron Microscopy (SEM)

The Scanning Electron Microscopy (SEM) images were obtained by a TESCAN MIRA3 electron microscope (Fig 3.5) equipped with a Field Emission Gun (FEG), operating at 20.0 kV. The magnifications used were 1, 10, 50 and 100 kx.

Figure 3.5 - TESCAN MIRA3 electron microscope.

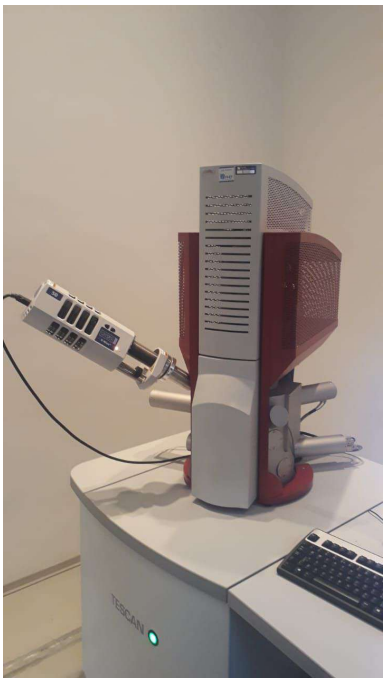

Source: Author.

3.2.6 Raman spectroscopy

The Raman spectra were obtained through a Horiba Scientifica (Laboram HR evolution mode) spectrometer (Fig 3.6), with a laser wavelength of 514 nm. The range of the analyses was 100 - 3000 cm^{-1}.

Figure 3.6 - Horiba (LabRAM HR Evolution Mode).

Source: Author.

3.3 Catalytic tests

The catalytic tests were performed in a fixed-bed stainless steel reactor, previously built specifically for the CO_2 hydrogenation reaction. Given the nature of the process, which was carried out under high pressure conditions, the system was designed with safety accessories including a protection grid. As shown in Figure 3.7, the main case and the removable slabs were constructed in stainless steel. In the left section (Figure 3.7) instruments such as temperature and pressure controllers, voltage and amperage readers and mass flow controllers were installed. The left side is also equipped with three-way, "open and close" and backpressure control valves. In the rear side of the main case, a pressure relief valve was inserted for security. In the oven case (right section), an internal isolation was made with glass wool to prevent high temperatures from damaging the electronic devices. The wool was inserted on the walls and sealed with thinner steel, in order to prevent wool degradation and protect the user from aspirating it. Furthermore, a condenser was installed in the gas line after the fixed-bed reactor to collect methanol and other liquid products.

Figure 3.7 - Catalytic Unit for the CO_2 hydrogenation reaction.

Source: Author.

The operating conditions were optimized by performing catalytic tests of the CO_2 hydrogenation over a commercial catalyst $Cu/ZnO/Al_2O_3$ (Prosint Química S.A.) with molar composition of 0.56, 0.28 and 0.16 of Cu, Zn and Al, respectively. The experiments were carried out following the conditions presented in literature (Section 2.3.1). The reaction temperature was in the range 200 - 300 °C, pressure conditions tested were 1, 10, 20 and 30 bar, H_2/CO_2 molar ratio of 3 and Gas Hourly Space Velocity (GHSV) of 3000 h^{-1}.

After a series of tests with the commercial catalyst, the operating conditions to be used in all experiments were defined and the complete experimental procedure was: 0.1 g of the catalyst were measured and diluted in 1 g of SiC (Sigma-Aldrich) or Quartz, the mixture was then loaded into the stainless steel tubular reactor using glass wool as a support for the solid, then the fixed bed was pressurized using the backpressure valve with He flow in order to check for gas leaks. Afterwards, the material was reduced at 300 °C for 1 h under 50 mL/min of H_2 flow, which was

switched to 30 mL/min of He after the reduction step to remove H atoms adsorbed on the metallic sites. The system was kept at this condition for 30 min, then the reactor temperature was set to the reaction temperature. Subsequently, the flow was changed to the 3:1 H_2/CO_2 reactant mixture setting the flow rate to obtain a GHSV of 3000 h^{-1}, bypassing the reactor to be analysed by Gas Chromatography (GC), with the aim of analysing the reactants feed. The reactor was then pressurised to 30 bar with He using the backpressure valve. Finally the flow was switched to the reactant mixture, starting the catalytic reaction. The condenser was kept at 0 °C during the entire experiment, a thermostatic water-ethylene glycol bath was used to control the temperature. The gas products were analysed every 20 min by GC and Mass Spectrometry (MS) described in the following item. The liquid products were collected and analysed after the reaction by another GC (Clarus 580).

3.3.1 Gas Chromatography (GC)

The gas chromatography method was developed using conditions appropriate to evaluate the signal area of the components and prevent peak overlap. The calibrated gases were H_2, CO_2, CO, CH_4 and DME. The gas chromatograph used was a Clarus 500 GC (Perkin Elmer), equipped with TCD and FID detectors. The column employed was the Elite Q and the carrier gas was He. The liquid products were analyzed in a Clarus 580 GC (Perkin Elmer) by a FID detector, calibration was performed for methanol and ethanol, the injection volume was 1 µL for all samples. The equipment is presented in Figure 3.8.

Figure 3.8 - Gas Chromatrographs (a) Clarus 500 GC; (b) Clarus 580 GC.

Source: Author.

3.3.2 Mass Spectrometry (MS)

In order to analyse potential unknown products and confirm the results obtained by GC, the QMS 403 D Aeolos Mass Spectrometer was coupled to the catalytic unit using a three-way valve to change the flow between the GC and the MS. The carrier gas used was He as well, with 300 mL/min flow. All mass-to-charge ratio (m/z) values from 1 to 100 were monitored.

4 RESULTS

4.1 Resulting samples

The Graphene Oxide (GO) synthesis was carried out following the method described in Section 3.1.1. During the procedure, the reactants undergone several physical changes. Figure 4.1 presents the reaction mixture aspect over the synthesis steps. After mixing graphite with the acids and adding $KMnO_4$, a "moss-green" color was observed (Figure 4.1a), which was maintained over the 24 h of this step. At the final steps, the addition of ice made the color change to dark purple (Figure 4.1b), becoming yellow after pouring H_2O_2 (Figure 4.1c). Finally, when filtered and washed, the suspension became orange coloured, with a brown sedimentary material at the bottom, as shown in Figure 4.1d. Subsequently, the suspension was centrifuged and the water removed, resulting in a dark brown gel, which consists in GO (Figure 4.2).

Figure 4.1 - GO synthesis after: (a) mixing graphite, acids and $KMnO_4$; (b) adding ice; (c) adding H_2O_2 and (d) filtering and washing.

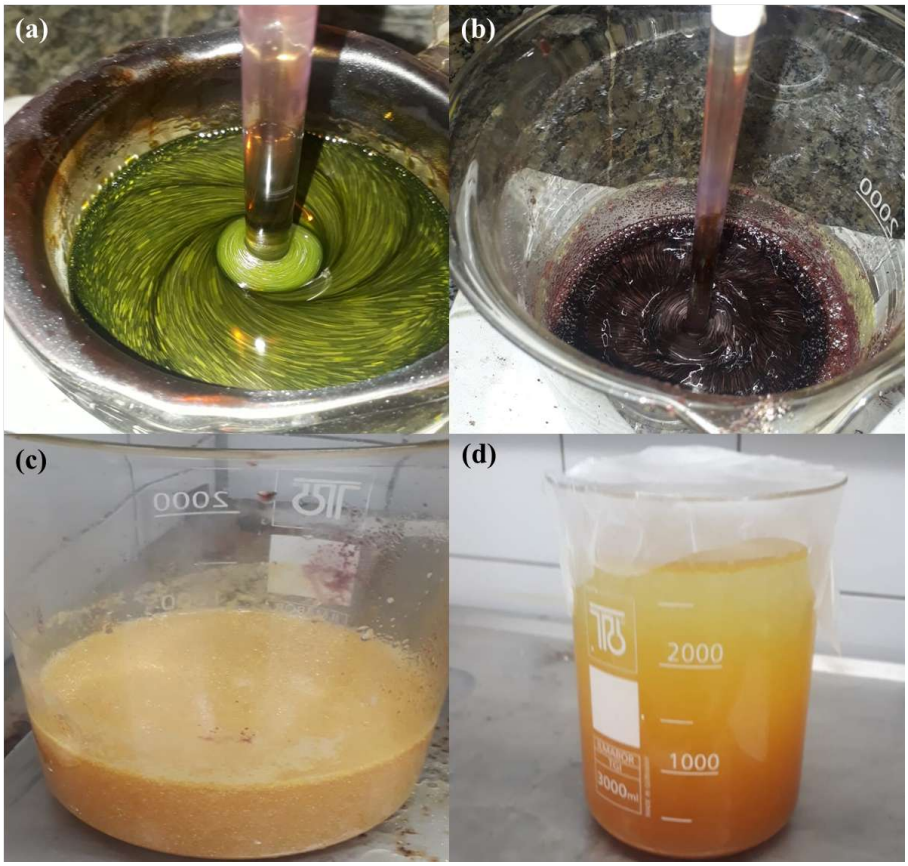

Source: Author.

Figure 4.2 - Graphene Oxide (GO) gel resulting product.

Source: Author.

With the GO gel, the supports and catalysts were synthesized by the hydrothermal reduction method according to the procedure described in Sections 3.1.3 and 3.1.4, respectively. As an example, Figure 4.3 presents the resulting Zn−rGO_P support, consisting of a black cylinder. The other samples, including rGO, supports and catalysts, presented similar shape, and therefore are not shown. The aspect of the obtained material is in accordance with the catalyst reported by (DEERATTRAKUL et al., 2018), which the authors referred to as rGO hydrogel and rGO aerogel after drying.

Figure 4.3 - (a) As-synthesized Zn-rGO_P support; (b) After drying.

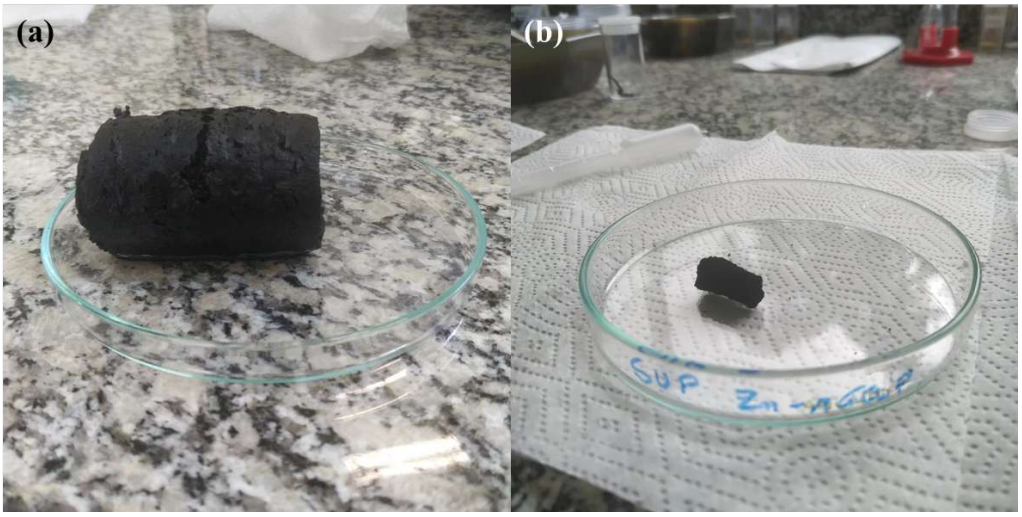

Source: Author.

The volume of the as-synthesized and dried rGO and support materials were determined by direct measures of the samples, which were approximated to ideal cylinders, the results are presented in Table 4.1, where ρ_b is the bulk density determined with the resulting dry volume and mass. During the drying process, a significant decrease in size was observed in the materials, as shown in Figure 4.3b as an example. This phenomenon may be explained due to removal of residual water from the synthesis procedure, retraction of graphene layers, and the collapse of the structure resulting from abrupt water transition from liquid to gas state, given the high surface tension of the solvent. Analysing the macroscopic structure of the samples, it was observed that the decrease in volume on the products prepared with Pluronic F-127 surfactant was similar to the surfactant-free samples, while in the samples containing Triton X-100 the reduction was less drastic during drying, indicating that it prevented retraction of graphene layers to some extent. When synthesizing rGO-based photocatalysts, (HU et al., 2017) reported a similar effect on volume reduction using several surfactants to improve the structure and morphology of the TiO_2/rGO nanocomposites. As a consequence of the changes in volume, the Triton containing samples presented a substantial decrease in bulk density compared to the counterparts. Surprisingly, the Zn-rGO_P sample weighted more than expected, resulting in higher density, which can be attributed to experimental errors or regions of different concentration on the GO. The synthesized rGO_T samples have densities comparable with the study reported by (CÁMARA-TORRES et al., 2021), in which the authors obtained materials with $\rho_b = 0.05$ and 0.09 g/cm^3, however, the methodology involved

thermal reduction at more drastic conditions (300 °C) followed by a densification procedure. On the other hand, rGO_S and rGO_P presented significant higher ρ_b. Furthermore, the catalysts Cu@Zn-rGO are not included in the analysis, as the materials were very different in shape, in fact the Cu@Zn-rGO_P sample was not even a cylinder when the hydrothermal reduction was finished, as the material obtained was in small chunks inside the autoclave. Also noteworthy was the difference in the time required for completely drying at room temperature, ranging from a couple days for the Triton samples to almost two weeks for some materials with Pluronic. This can be explained by the amphiphilic nature of Triton, which combined with the rGO hydrophobicity may have resulted in an overall hydrophobic material. On the other hand, it has been reported that Pluronic F127 causes surfaces to become hydrophilic, despite also being an amphiphilic surfactant (LUK et al., 2008).

Table 4.1 - Volume reduction during drying and bulk density of rGO and supports.

Sample	V_i (cm^3)	V_f (cm^3)	Vol. reduction (%)	ρ_b (g/cm^3)
rGO_S	56.0	3.2	94.3	0.19
rGO_P	52.9	3.3	93.8	0.19
rGO_T	42.6	33.2	22.1	0.05
Zn-rGO_S	36.3	3.0	91.7	0.25
Zn-rGO_P	34.9	3.1	91.3	0.47
Zn-rGO_T	34.6	18.9	45.5	0.05

Source: Author.

When using Triton as surfactant, the resulting materials presented a soft spongeous aspect, as observed in Figure 4.4, in contrast with the hard solids obtained from the surfactant-free synthesis or with Pluronic. In general, upon breaking the cylinders, the materials assumed a powder form (Figure 4.5a), except for the rGO_P and rGO_T samples, as in the former the formation of sheets was observed (Figure 4.5b) and in the latter the material assumed an aspect of small chunks, similar to a "modeling clay" (Figure 4.5c), in both cases some characterization analyses such as XRD were hindered. However, the support and catalysts synthesized with Pluronic presented powder aspect as well, indicating the effect of interaction of metals with the rGO matrix. Interestingly, when breaking the Triton-containing cylinders Zn-rGO_T and Cu@Zn-rGO_T, a "soft" powder aspect was obtained.

To evaluate the effect of Zn and rGO as supports on the properties and performance of the materials, the catalysts Cu/ZnO (Figure 4.5d), Cu@rGO_S and Cu@rGO_P were also synthesized through the wetness impregnation method and hydrother-

Figure 4.4 - (a) As-prepared Cu@Zn-rGO_T catalyst; (b) Final product after drying.

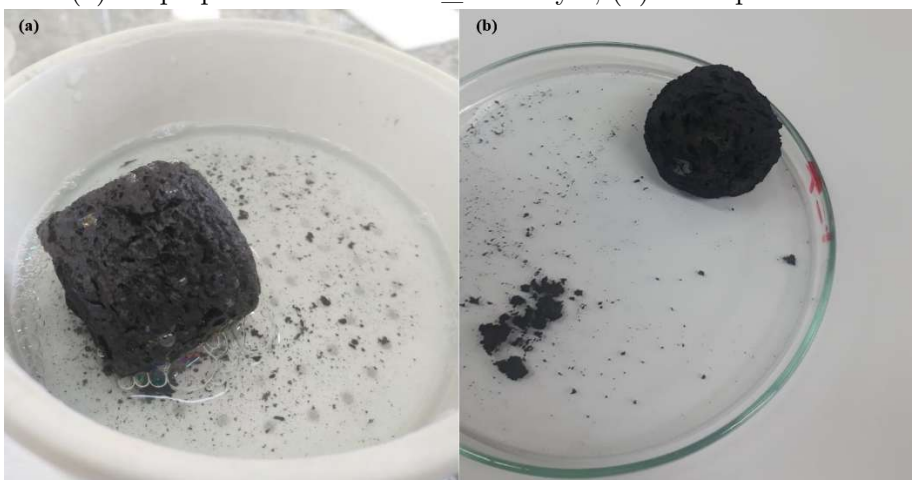

Source: Author.

Figure 4.5 - (a) Cu@Zn-rGO_P powder; (b) rGO_P sheets; (c) rGO_T small chunks; (d) Cu/ZnO powder.

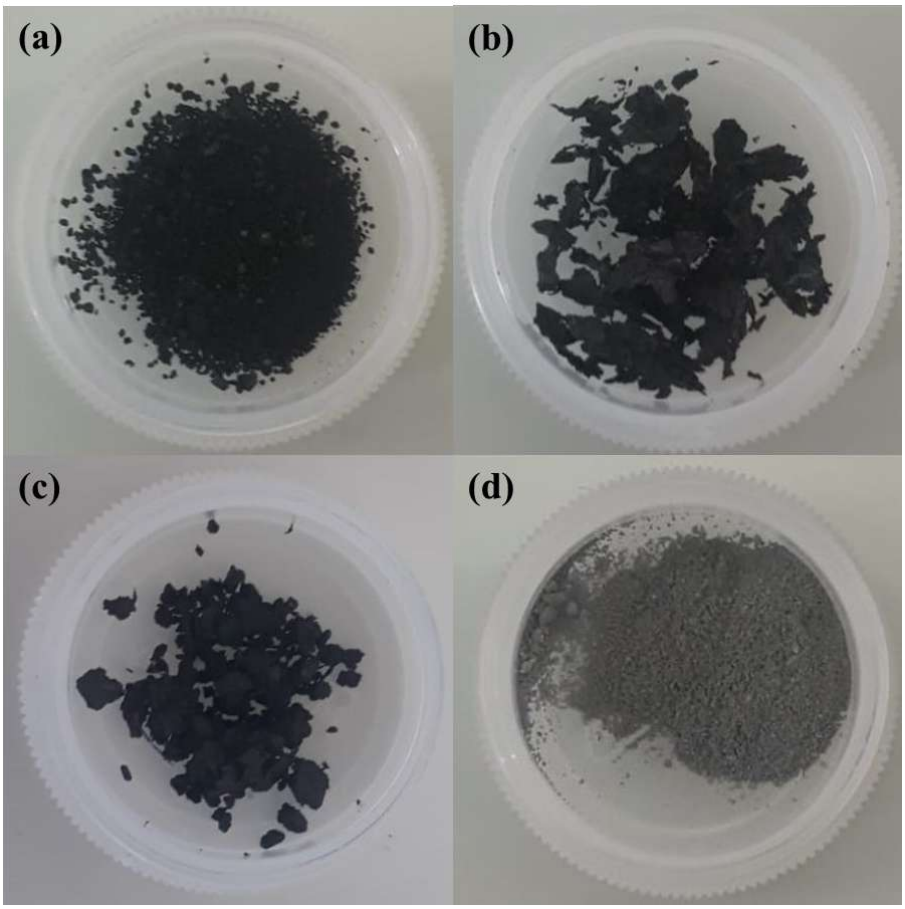

Source: Author.

mal route, respectively. The Cu@rGO samples presented black cylinder shape, size reduction during drying and powder form in the final product as well.

A summary of the samples successfully synthesized in this study and the respective procedures is presented in Table 4.1.

Table 4.2 - Samples synthesized in this study and the procedure employed.

Sample	Procedure
Cu/ZnO	Wetness Impregnation
GO	Hummers method
rGO_S	Hydrothermal reduction
rGO_P	Hydrothermal reduction
rGO_T	Hydrothermal reduction
Zn-rGO_S	Hydrothermal reduction
Zn-rGO_P	Hydrothermal reduction
Zn-rGO_T	Hydrothermal reduction
Cu@Zn-rGO_S	One-step hydrothermal reduction
Cu@Zn-rGO_P	One-step hydrothermal reduction
Cu@Zn-rGO_T	One-step hydrothermal reduction
Cu/Zn-rGO_S	Wetness impregnation
Cu/Zn-rGO_P	Wetness impregnation
Cu/Zn-rGO_T	Wetness impregnation

Source: Author.

4.2 Characterization

4.2.1 Specific surface area

As described in Sections 3.2.1 and 3.2.2, the surface area of the materials was determined by N_2 and MB physisorption. N_2 adsorption analysis with BET theory was only employed for the characterization of the support ZnO and the catalyst Cu/ZnO. The rGO-containing samples were analysed by MB adsorption and linearization of the Langmuir isotherm. Calculations were performed following the procedure reported by (ITODO et al., 2010), the equilibrium concentrations and quantity of MB adsorbed for all materials were best represented by the Langmuir type 1 linear form, as expected for the majority of porous solids. The quantities of MB adsorbed at equilibrium were determined by Equation 4.1, the linearization of the Langmuir isotherm (Type 1) is expressed by Equation 4.2 and the surface area results were obtained by Equation 4.3.

$$q_{eq} = \frac{(C_0 - C_{eq})V_{\mathrm{MB}}}{m_{\mathrm{s}}} \tag{4.1}$$

$$\frac{C_{eq}}{q_{eq}} = (1/q_m)C_{eq} + 1/Kq_m \tag{4.2}$$

$$S = \frac{q_m\, a_{\mathrm{MB}}\, \mathrm{Na} \cdot 10^{-23}}{M_{\mathrm{MB}}} \tag{4.3}$$

In which: q_{eq} is the quantity of MB adsorbed at equilibrium (mg/g), C_0 the initial MB solution concentration (mg/L), C_{eq} the MB solution at equilibrium read by UV-Vis (mg/L), V_{MB} the volume of MB solution (L), m_{s} the adsorbate mass (g), q_m is the maximum quantity of MB adsorbed (mg/g), K the adsorption equilibrium constant, S is the specific surface area (m^2/g), a_{MB} the area occupied by one molecule of MB (197.2 Å²), Na the Avogadro number and M_{MB} the MB molecular weight (373.9 g/mol).

The specific surface area results (Table 4.3) indicate that rGO may be an appropriate support for copper catalysts, as it presented excellent surface area, notably higher than ZnO. Even though the surface area of the catalysts is expected to be lower than the support area, as metals occupy adsorption sites, the Cu@Zn−rGO_S catalyst surface area harshly decreased compared with rGO_S. This behavior is in agreement with previous research of our group, wherein the CeO_2-rGO support exhibited an expressive diminishing of the specific surface area in comparison with the rGO counterpart samples (FRANCHINI et al., 2020). Results of High-Resolution Transmission

Electron Microscopy (HRTEM) showed CeO_2 was anchored on the rGO support at the nanoscale in a continuous manner, explaining the specific surface area drop.

Table 4.3 - Specific surface area.

Sample	q_m (mg/g)	S (m^2/g)
ZnO	-	0,346
Cu/ZnO	-	0,194
rGO_S	290	920
Zn−rGO_S	148	470
Zn−rGO_P	193	612
Zn−rGO_T	242	769
Cu@Zn−rGO_S	86	272
Cu@Zn−rGO_P	154	490
Cu@Zn−rGO_T	239	759

Source: Author.

With regard to the rGO samples synthesized using surfactant, the MB adsorption experiments did not exhibit plausible results, therefore only the specific surface area obtained for rGO_S is presented. This divergence might be originated due to the macroscopic shape of the samples discusses in the previous section, considering rGO_P presented the shape of sheets while rGO_T was obtained in small chunks, so transformation into powder could not be achieved in both cases. Thus, a possible hypothesis for these values of specific surface area might be related to mass transport phenomena. Conversely, the samples containing Zn and Cu/Zn could be transformed into powder and the results are consistent, revealing the beneficial role of the surfactant in keeping the structural integrity and improving the specific surface are of the rGO supported catalysts. While Pluronic did not cause significant macroscopic changes to the samples (Section 4.1), it was observed that the decrease in surface area when adding the metallic phases was not as drastic as for the surfactant-free counterparts. This effect was even less pronounced on the Triton samples, as surface area of the catalyst was practically the same as the result for the support. Accordingly, (HU et al., 2017) observed a similar effect on the specific surface area when preparing TiO_2/rGO nanocomposites using several surfactants. The authors suggest that a nonionic surfactant, such as Triton X-100, may promote a homogeneous dispersion of TiO_2 on rGO through strong H-Bond forces, causing increase in surface area. Therefore, it is possible that a similar effect occurs when using Cu and Zn.

4.2.2 Thermogravimetric analysis

The thermal stability of catalysts is a fundamental aspect for high performance in the CO_2 hydrogenation reaction, as the conversion temperature range is 200 - 300 °C. Therefore, all sample were tested in synthetic air atmosphere in order to evaluate if the catalysts are adequate for the reaction. It is important to point out that the reduction step was performed in a hydrogen atmosphere while the reaction was conducted with a H_2/CO_2 mixture, so the mass loss profile at these conditions may differ from the results obtained with synthetic air. Nevertheless, the analyses serve to have a grasp on the thermal stability of the materials. Additionally, the results are also important to estimate the stability of graphene-based materials in regeneration processes, which are also performed under oxidizing atmosphere.

Figures 4.6a and 4.6b present the results for mass loss profile and respective first derivative for the rGO samples. Specifically for rGO_S, the thermobalance was coupled to a Mass Spectrometer (MS), so the effluent gases were analyzed. Mass spectrum indicated that the mass loss at the early stage of the analysis may be attributed to desorption of physisorbed residual water from the synthesis process, whereas the abrupt loss at approximately 500 °C (derivative peak as shown in Figure 4.6b) is due to combustion of the carbon structure, as the m/z ratio values of 18 and 44 were observed, relating to H_2O and CO_2 respectively. At 800 °C the material was completely decomposed. Addition of surfactants caused changes in the thermal profile. The profile obtained for the rGO_P sample presented a small peak at 210 °C, which may be attributed to hydroxyl and ether oxygenated groups present on the Pluronic structure (SAMSUDIN et al., 2015). Regarding stability, while the major mass loss started earlier than for rGO_S (at 400 °C), it may observed that the sample was not completely degraded at 800 °C. However, over 10% of the Pluronic sample mass was lost by 300 °C, which may affect negatively the catalyst stability.

As for rGO_T, the result was significantly different. Firstly, no losses were observed up to 100 °C, indicating the absence of physisorbed water content in the material, which may be related to the possible hydrophobic characteristic discussed previously. Secondly, two mass loss stages were observed, indicated by two distinct peaks in Figure 4.6b, with the first one starting at 250 °C and reaching maximum at 320 °C, implying the removal of oxygenated groups present on the surfactant. However, comparing the profile obtained with the results reported by (MITSUDA et al., 1989) on the evaporation of Triton X-100 under air atmosphere at different temperatures, it may be inferred that the shouldering present in the first loss peak corresponds to

degradation of the oxygenated groups of the surfactant, as the authors observed this effect on a high quantity of the material at 283 °C. Furthermore, the second peak at 600 °C, is attributed to degradation of either the whole or part of the graphene structure, indicating improvement in the thermal stability in a sense. Nevertheless, experiments with varying amounts of the surfactant and coupling of TG with MS would be required to fully comprehend the effect of the materials in combination with rGO.

Figure 4.6 - (a) Mass loss profile and (b) Mass loss first derivative for the rGO samples.

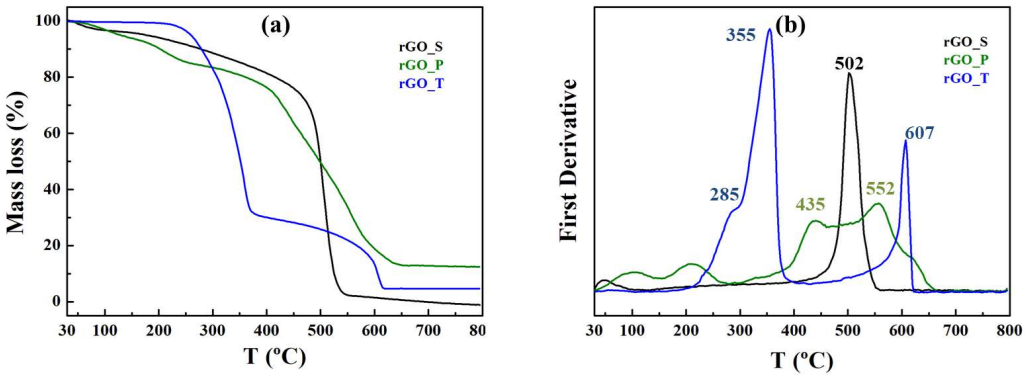

Source: Author.

The results for the Zn-rGO supports are exhibited in Figures 4.7a and b. For Zn-rGO_S, it can be noted that the addition of Zn did not cause significant differences comparing to rGO_S, as the only major loss is still around 500 °C. Regarding Zn-rGO_P, the diffuse derivative peak became more defined, indicating that the Pluronic groups either interacted with Zn on the rGO structure or were removed during the hydrothermal synthesis, which would explain the absence of mass loss at lower temperatures. As for Zn-rGO_T, the behavior of mass loss in two stages was maintained, however, as the the main loss is observed at 550 °C, in this case it is easier to attribute the peak at 300 °C to the surfactant surface oxygenated groups, which is in agreement with the rGO_T result as well as the study by (MITSUDA et al., 1989). Also, the lower intensity of the first peak (compared to rGO_T) is an indicative that some surface groups may interact with ZnO more intensely.

Figure 4.7 - (a) Mass loss profile and (b) Mass loss first derivative for the Zn-rGO samples.

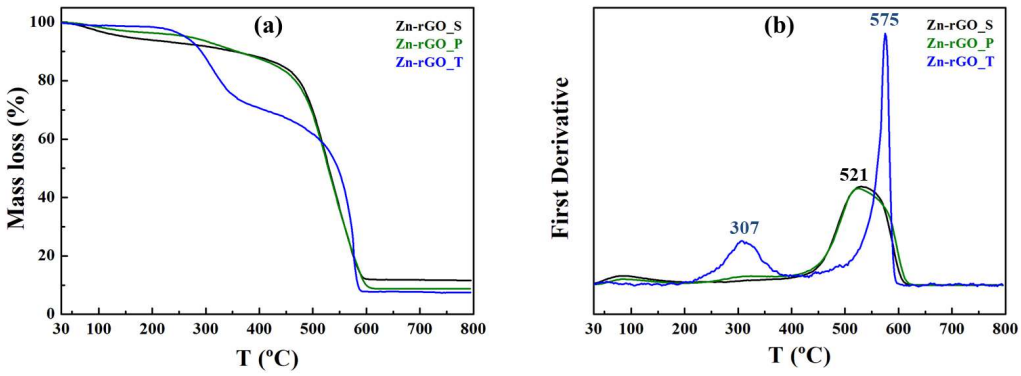

Source: Author.

The mass loss profiles and first derivatives obtained for the Cu@Zn-rGO catalysts are presented in Figures 4.8a and 4.8b, respectively. For all materials, it becomes clear that the addition of copper shifted the derivative peaks to the temperature range 300 - 400 °C, indicating that the metal may promote the activity of the decomposition of the rGO structure, effect which was found to be more expressive in the Triton-containing catalyst. Similarly as was observed for the supports, the Cu@Zn-rGO_S and Cu@Zn-rGO_P samples presented very similar behavior, both in the profile and first derivative, except for the final mass, which was slightly higher for the Pluronic sample. Also in agreement with the results for rGO and the supports, significant water loss at early stages of the analysis was also not observed for Cu@Zn-rGO_-T, which further indicates the hydrophobicity of the material obtained. Also, the mass loss peaks corresponding to the surfactant and rGO are overlapped (Fig 4.8b), meaning that the possible positive effect observed on the previous samples is not as significant when Cu is included.

Figure 4.8 - (a) Mass loss profile and (b) Mass loss first derivative for the Cu@Zn-rGO samples.

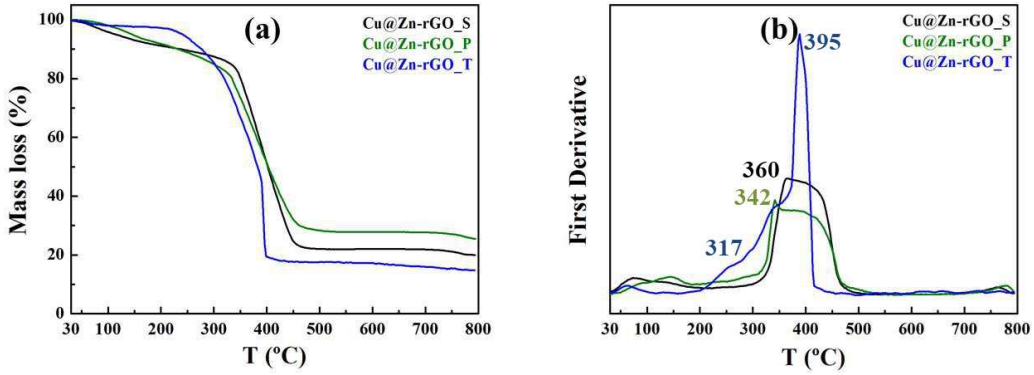

Source: Author.

The TG analyses were also useful for choosing an appropriate calcination temperature for the Cu/Zn-rGO catalysts. After the wetness impregnation procedures and prior to calcination, the thermal stability of the impregnated precursors was also evaluated following the same methodology. Given that all materials presented the main loss around 350 °C, attributed to the carbonic chain combustion, calcination was performed at 300 °C for all samples, in order to prevent degradation of important components. The TG results for the prepared Cu/Zn-rGO catalysts after calcination are presented in Figure 4.9. It may be observed that at lower temperatures the mass change was less expressive than for the other samples, because residual water as well as nitrate and hydroxyl groups are removed with thermal treatment. The catalysts prepared by this procedure also presented the main derivative peak around 300 - 400 °C, evidencing a predominant role of the surfactant nature. Nevertheless, the Cu@Zn-rGO samples exhibited lower stability than its counterparts catalysts, which may be related to oxygen groups remaining from the synthesis procedure. However, for Cu/Zn-rGO_P, two well-resolved peaks were observed, suggesting the presence of different carbon forms. Nonetheless, the correspondent peaks for the other samples exhibit a broad shape, evidencing peaks overlapping. Also the final mass was slightly lower than for the impregnated counterparts.

Figure 4.9 - (a) Mass loss profile and (b) Mass loss first derivative for the Cu/Zn-rGO samples.

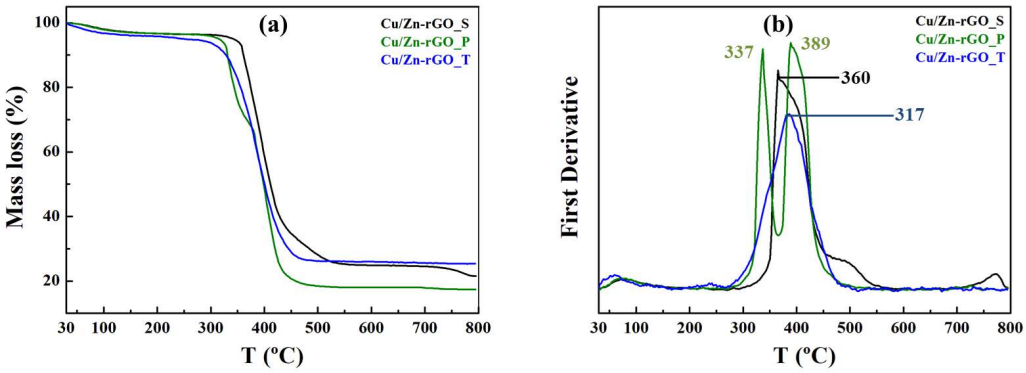

Source: Author.

Table 4.4 presents a comparison between the thermal stability of the rGO obtained with previous reports by a few authors. In general, the results are in agreement with the thermal stability reported by (DEERATTRAKUL et al., 2016), in which the rGO mass was significantly lower at 600 °C, even though it was synthesized by chemical reduction with hydrazine. Also, the authors obtained a similar profile to the catalysts of this study in the analysis of a 30% Cu-Zn/rGO material synthesized by wetness impregnation, with the final mass being approximately the metal content. (ALAM et al., 2017) produced a more stable rGO sample, as the main mass loss started at 600 °C, however, it is important to highlight that both GO and rGO were obtained by very different methods than those of the present study. In contrast, significant differences in stability were observed comparing to materials reduced thermally with Ar/H_2 (OSSONON; BÉLANGER, 2017) and chemically with galactose (KRISHNAMOORTHY et al., 2012)), in which rGO was not completely decomposed even in drastic temperatures. Nevertheless, the comparison indicates that distinct rGO synthesis procedures may result in materials with varying thermal stabilities.

Table 4.4 - Thermal stability of rGO reported by a few authors.

Reduction method	Main loss (°C)	Final temperature (°C)/mass (%)	Reference
Hydrothermal	500	800/0	This study
Chemical with Hydrazine	500	600/25	(DEERATTRAKUL et al., 2016)
Thermal without gas flow	600	800/0	(ALAM et al., 2017)
Thermal in $Ar/5\%H_2$	500	900/75	(OSSONON; BÉLANGER, 2017)
Chemical with galactose	100	1000/65	(KRISHNAMOORTHY et al., 2012)

Source: Author.

Furthermore, as the final remaining masses approached 10% and 20% respectively for the supports and catalysts, the data also suggests that the precursor salts used in the synthesis procedure were in the correct amount to result in catalysts with 10% wt. of Zn and Cu, even though a more precise analysis such as Inductively Coupled Plasma (ICP) would be required to assess the exact quantity of metal present in the materials.

Overall, from the TG analyses, it can be inferred that the materials have suitable stability for the CO_2 hydrogenation reaction, with the exception of Cu@Zn-rGO_T. It is worth noticing that the thermal analysis atmosphere is entirely distinct from the catalytic tests. Regarding the Cu@Zn-rGO_T catalyst, temperatures above 200 °C may result in decomposition of the surfactant, which may lead to a highly undesirable structure collapse or graphene layers re-stacking. Apart from these materials, all other catalysts presented stability up to 350 °C, beyond the temperature range for the reaction. Furthermore, given that the start of the Cu/Zn-rGO_T sample decomposition was delayed by approximately 100 °C in comparison with rGO, supports and other catalysts containing Triton, it may be inferred that a certain amount of surfactant was lost in the calcination step, as the main loss occurred right beyond this temperature on the prepared catalyst.

4.2.3 X-Ray diffraction

The XRD patterns obtained for the calcined support ZnO and Cu/ZnO impregnated catalyst are shown in Figure 4.10. All diffraction lines obtained for the support (green) correspond to ZnO phase with hexagonal crystal system. Impregnating copper produced diffraction lines at 2θ = 35.53, 38.81, 48.51, 58.29 and 61.53°, all of which are attributable to the monoclinic CuO phase. The appearance of relatively intense CuO peaks in the pattern indicates the presence of Cu with larger crystallite sizes. As a matter of fact, the calculated crystallite size considering the peak at 2θ = 38.81° was 19.2 nm, which is plausible considering the low surface area of ZnO, presented in Section 4.2.1.

Figure 4.10 - Diffraction patterns obtained for ZnO and Cu/ZnO.

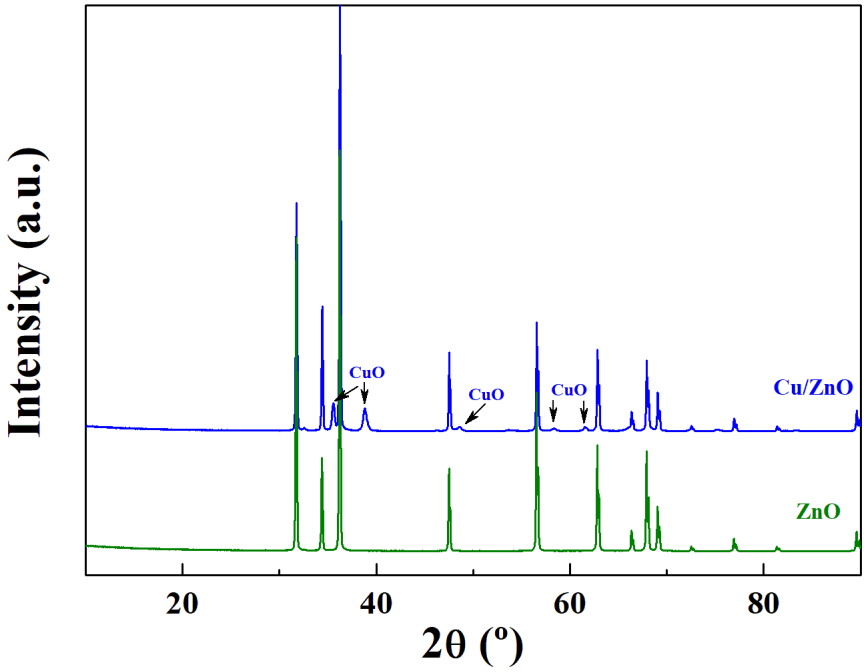

Source: Author.

The GO and rGO synthesis were assessed by XRD as shown in Figures 4.11a and 4.11b, respectively. The diffractogram for GO presented a peak at 2θ= 12.28°, attributable to graphene oxide, indicating that graphite was successfully oxidized during the synthesis procedure. The low intensity and broad base of the peak indicate the formation of rGO with a structure without stacking order and few layers. Figure

4.11b shows two broad peaks, with maximum at 2θ= 24.53; 43.36 and 78.82°. The peak at 24.53° corresponds to the basal plane of graphite, the broadening indicates a disordered structure with few layers. Overall, the diffractogram is characteristic of reduced graphene oxide. As mentioned previously, the aspect obtained with rGO_P and rGO_T made the XRD analyses difficult, due to height differences. Therefore the resulting diffractograms for both samples are not shown.

Figure 4.11 - Diffraction patterns obtained for (a) GO; (b) rGO_S.

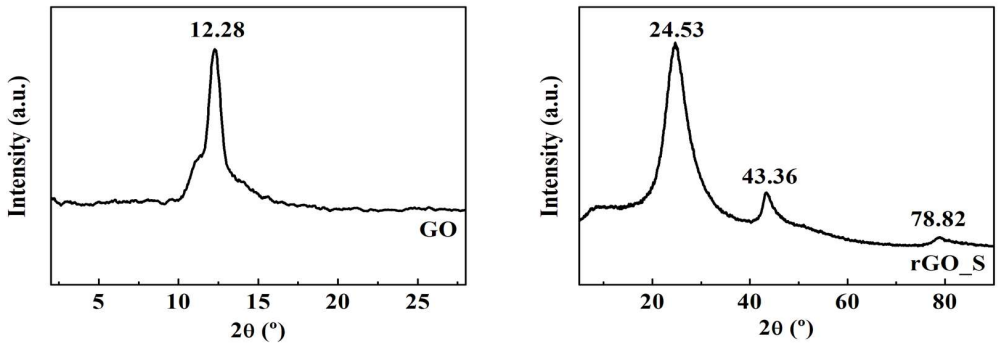

Source: Author.

Figure 4.12 shows the diffraction patterns obtained for the Zn-rGO supports. In all patterns, the rGO related peaks are still observed with broad bases, so the graphene structure was preserved during the hydrothermal synthesis with the addition of Zn. Also, the absence of lines attributable to Zn indicates very small crystallites, below the XRD equipment detection level. Furthermore, the sample containing Triton presented a slight blue shift, an indicative of larger interlayer distance (Table 4.5), also noteworthy was the decrease in number of layers, suggesting a pronounced effect of the surfactant on the structural integrity of the sample.

Figure 4.12 - Diffraction patterns obtained for the Zn-rGO supports.

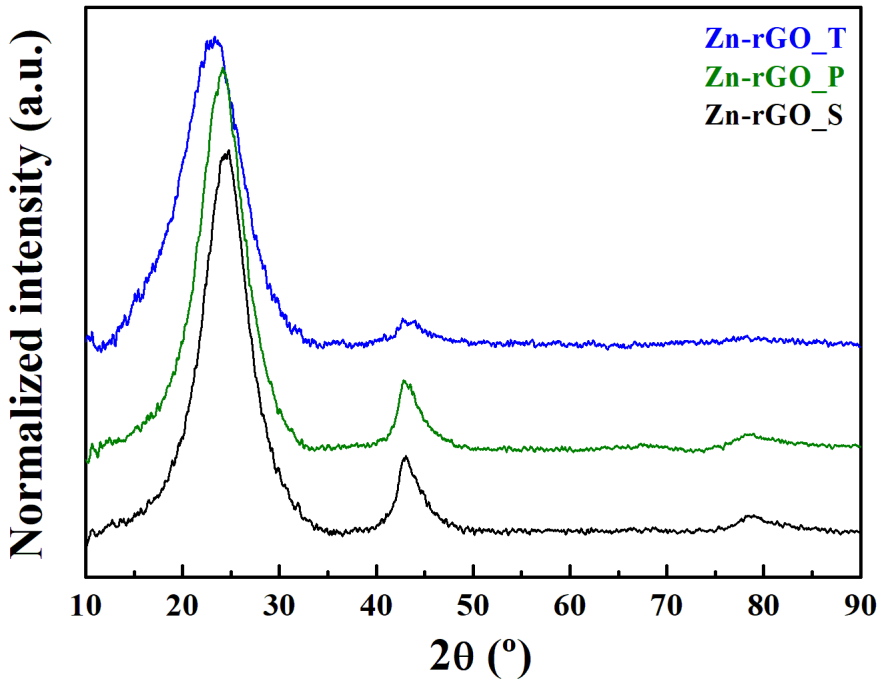

Source: Author.

The diffractograms for the Cu@rGO reference catalysts are presented in Figure 4.13. The addition of Cu in the hydrothermal synthesis of the surfactant-free sample caused no significant changes in the diffractograms. As for Cu@rGO_P, a peak corresponding the surfactant was detected around $2\theta = 19°$. The less intense satellite peaks could not be identified, but may be related to residual groups from the copper precursor salt, possibly fixated due to interaction with the surfactant. The absence of peaks related to copper oxide indicates high dispersion of the phase on the rGO surface, possibly with particle size of a few nanometers.

Figure 4.13 - Diffraction patterns obtained for the Cu@rGO catalysts.

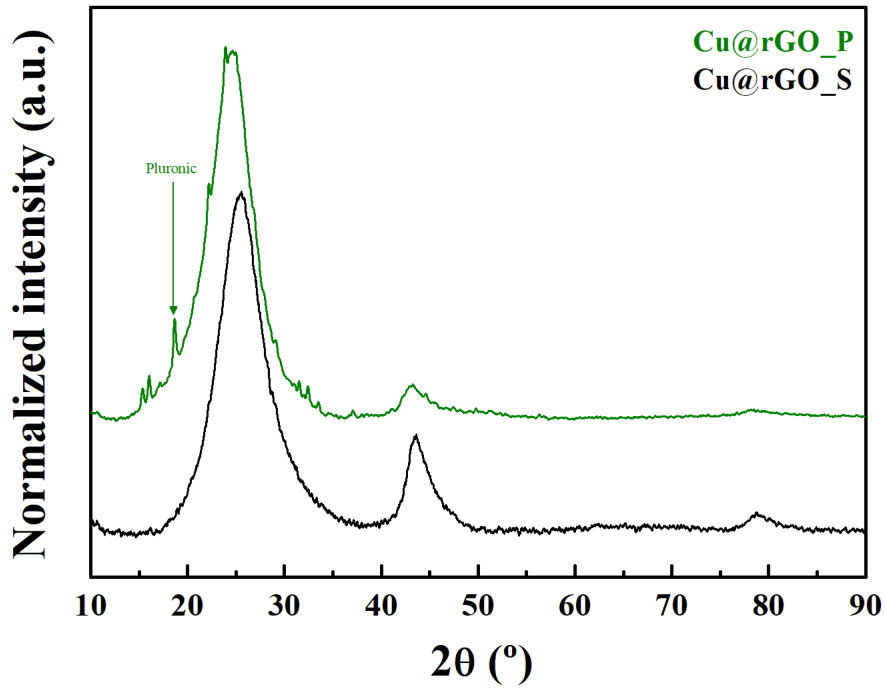

Source: Author.

Figure 4.14 presents the pattern obtained for the Cu@Zn-rGO catalysts, the addition of copper and zinc resulted in more complex diffractograms. The peaks corresponding to Cu_2O ($2\theta = 29.55$, 36.48, 42.30, 61.34 and 73.46°) were overlapped by ZnO, so determination of Cu particle size by the Scherrer equation was not possible, although the sharp and intense main peak at 36.48° indicates large particle size. In general, the Cu^{+1} oxidation state was observed, which may be the active site for CO_2 hydrogenation (YANG et al., 2013), although the interaction between reactants and copper active site is still unclear, as mentioned in Section 2.3.2.1 of the literature review. Conversely, on previous studies with Cu-based rGO supported catalysts, it has been reported the presence of CuO and Cu-Zn alloy, although the synthesis procedures are different from the present work (DEERATTRAKUL et al., 2016; WITOON et al., 2018). This effect may be attributed to the novel one step hydrothermal procedure used in the synthesis, in which Zn and Cu nitrates were added to the GO gel sequentially, whereas most papers employ methods such as coimpregnation or impregnation in supports prepared previously. On the other hand, the Cu@Zn-rGO_P sample presented both CuO and Cu_2O phases, indicating that the addition of Pluronic may have promoted oxidation of the original copper oxide to some extent. A similar

observation of both phases was reported by (FAN; WU, 2016), when synthesizing rGO-supported catalysts using a Cu-ZnO-ZrO_2-Al_2O_3 (CZZA) precursor. The CuO peak identified (2θ= 52.26°) has low intensity and broadness, resulting in crystallite size of 18.7 nm, determined using Lorentz fitting profile and the Scherrer equation. Although crystallite size distribution may be heterogeneous, it may be inferred that the phase is poorly dispersed on the rGO structure. The peaks at low angle observed in the Pluronic containing and surfactant-free catalysts could not be identified. As for the Triton sample, aside from the overlapped ZnO and Cu_2O line, only a single peak was observed, which also was not identified. Also notable was the broader rGO peak at 2θ= 23.68° also slightly blue shifted.

Figure 4.14 - Diffraction patterns obtained for the Cu@Zn-rGO catalysts.

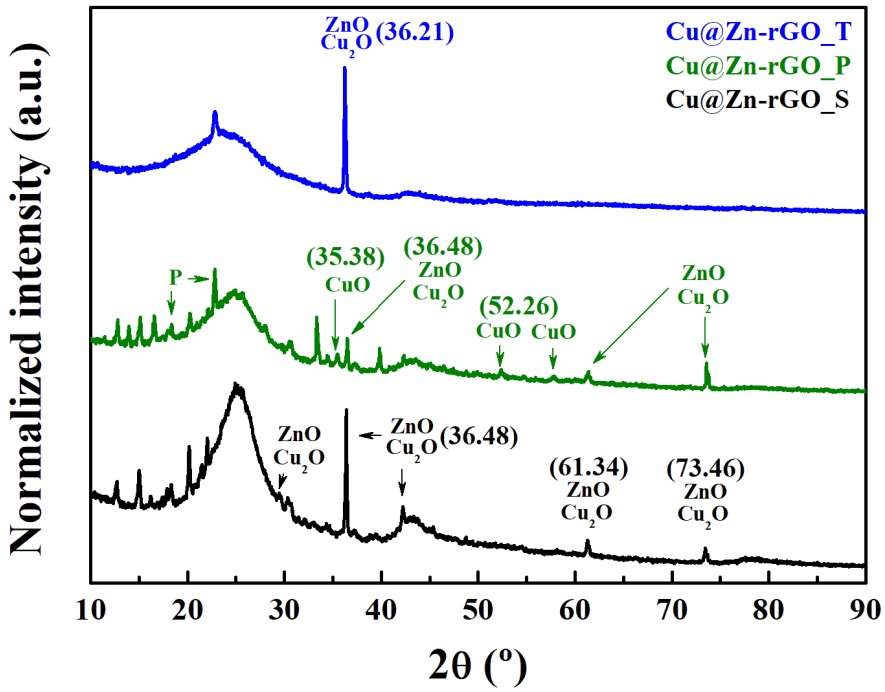

Source: Author.

Additionally, the number of graphene layers of the samples was estimated by XRD using the methodology described by (KUMAR et al., 2021), consisting of dividing the calculated mean layer width (Equation 4.4) by the interlayer distance (Equation 4.5), the results are shown in Table 4.5. This procedure was also reported by other authors (MAURO et al., 2012; GUERRERO-CONTRERAS; CABALLERO-BRIONES, 2015). The re-

sults indicate few-layered structure of the samples, as expected for graphene-based materials and also highlight the effectiveness of chemical exfoliation of graphite by the modified Hummers method employed in the GO synthesis. It has been established that few-layered materials (up to 10 layers) present thermal, mechanical and electrical properties similar to the remarkable features of monolayer graphene and these properties decrease as the number of layers is increased (KUMAR et al., 2021). Furthermore, the results suggest that introducing Cu,Zn and the Pluronic surfactant did not alter the number of layers significantly. The Cu@Zn−rGO_T sample presented the lowest L_c and number of layers, which may also be observed from the broader rGO peak, indicating that Triton might have been effective in maintaining a structure similar to monolayer graphene.

Table 4.5 - L_c, interlayer distance and number of layers for the graphene-based samples.

Sample	L_c (nm)	d (nm)	N
rGO_S	15.1	3.6	4 (4.1)
rGO_P	10.3	3.7	3 (3,0)
Zn-rGO_S	14.1	3.6	4 (3.9)
Zn-rGO_P	14.4	3.7	4 (3.9)
Zn-rGO_T	9.9	3.9	3 (2.6)
Cu@rGO_S	13.9	3.5	4 (4.0)
Cu@rGO_P	14.0	3.6	4 (3.8)
Cu@Zn-rGO_S	16.9	3.5	5 (4.8)
Cu@Zn-rGO_P	12.1	3.6	3 (3.3)
Cu@Zn-rGO_T	8.8	3.7	2 (2.4)

Source: Author.

The equations employed were:

$$L_c = 0,89\lambda\beta^{-1}\cos^{-1}(\theta) \tag{4.4}$$

$$d = \frac{n\lambda}{2\sin(\theta)} \tag{4.5}$$

$$N = \frac{L_c}{d} \tag{4.6}$$

where: L_c is the mean crystallite length (nm), λ the wavelength (nm), β the Full Width at Half Maximum (FWHM) of the peak used (rad), θ the angle between the incident ray and the scattering plane (rad), d is the interlayer distance (nm), n the number of wavelengths ($n = 1$ in this case) and N is the number of graphene layers.

Overall, from the results it was observed the rGO structure was maintained in all

samples. Also, by comparing the results obtained for the supports and Cu@rGO and Cu@Zn-rGO catalysts, it may be inferred that when using a single metallic phase (Cu or Zn), the hydrothermal procedure generates well dispersed phases, while employing both simultaneously may result in different degrees of interaction, promoting the interplay between the metallic phases and inhibiting interchange with rGO. The surfactants had different outcomes on the catalysts, as Pluronic may have promoted the fixation of groups from the Cu precursor, while Triton appears to have the effect of increasing the interlayer distance, resulting in samples with fewer graphene layers.

4.2.4 Scanning Electron Microscopy

The morphological analysis was carried out with a Scanning Electron Microscope (SEM) equipped with a Field Emission Gun (FEG), the images obtained for rGO_-S are presented in Figure 4.15. It was observed a folded "wavy" structure, possibly consisting of an agglomeration of graphene layers. The images also show a degree of homogeneity, as different morphology regions were not observed.

Figure 4.15 - SEM images of rGO_S with (a) 2 kx, (b) 20 kx and (c) 100 kx magnification.

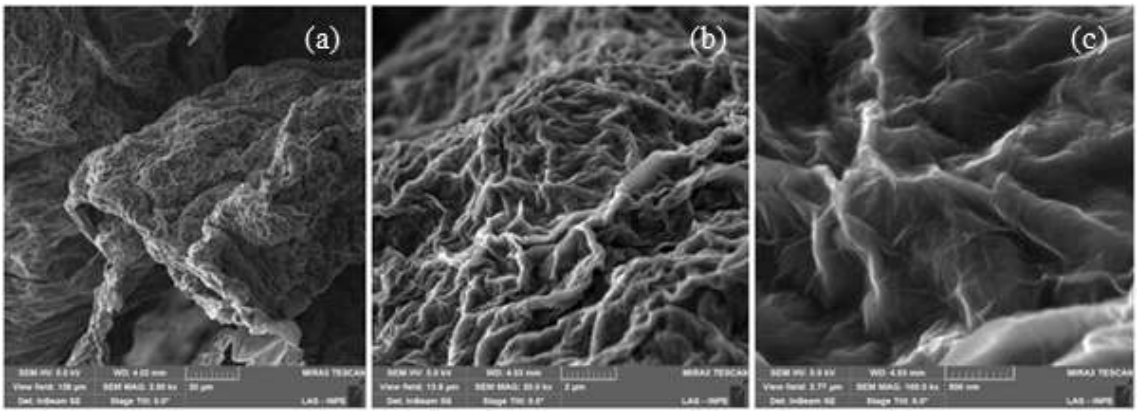

Source: Author.

Figure 4.16 presents the images obtained for rGO_P. Even though no significant difference was observed comparing to rGO_S, in this case the images better illustrates the layered structure of rGO. Using 40 and 100 kx magnifications, it may be noted the individual sheets close to each other.

The images obtained for the Zn-rGO_S support are shown in Figure 4.21. The addition of the metallic phase caused layers to become further agglomerated, while also originating regions with different morphology, as observed with 1 and 10 kx magnifications, suggesting a more heterogeneous structure.

For the Cu@Zn-rGO_P catalyst, the images are exhibited in Figure 4.18. The catalyst presented significant changes in comparison with the rGO samples and support. As the metal content is around 20%, it was observed the formation of a highly heterogeneous structure (Figure 4.18a), possibly due to metallic phases agglomerates and interaction with Pluronic. Using 10 and 30 kx magnifications, a structure of "blocks" was identified, and distinction between rGO layers can no longer be observed. At 100 kx magnification (Figure 4.18d), some large layers could be distinguished.

Figure 4.16 - SEM images of rGO_P with (a) 1 kx, (b) 10 kx, (c) 40 kx and (d) 100 kx magnification.

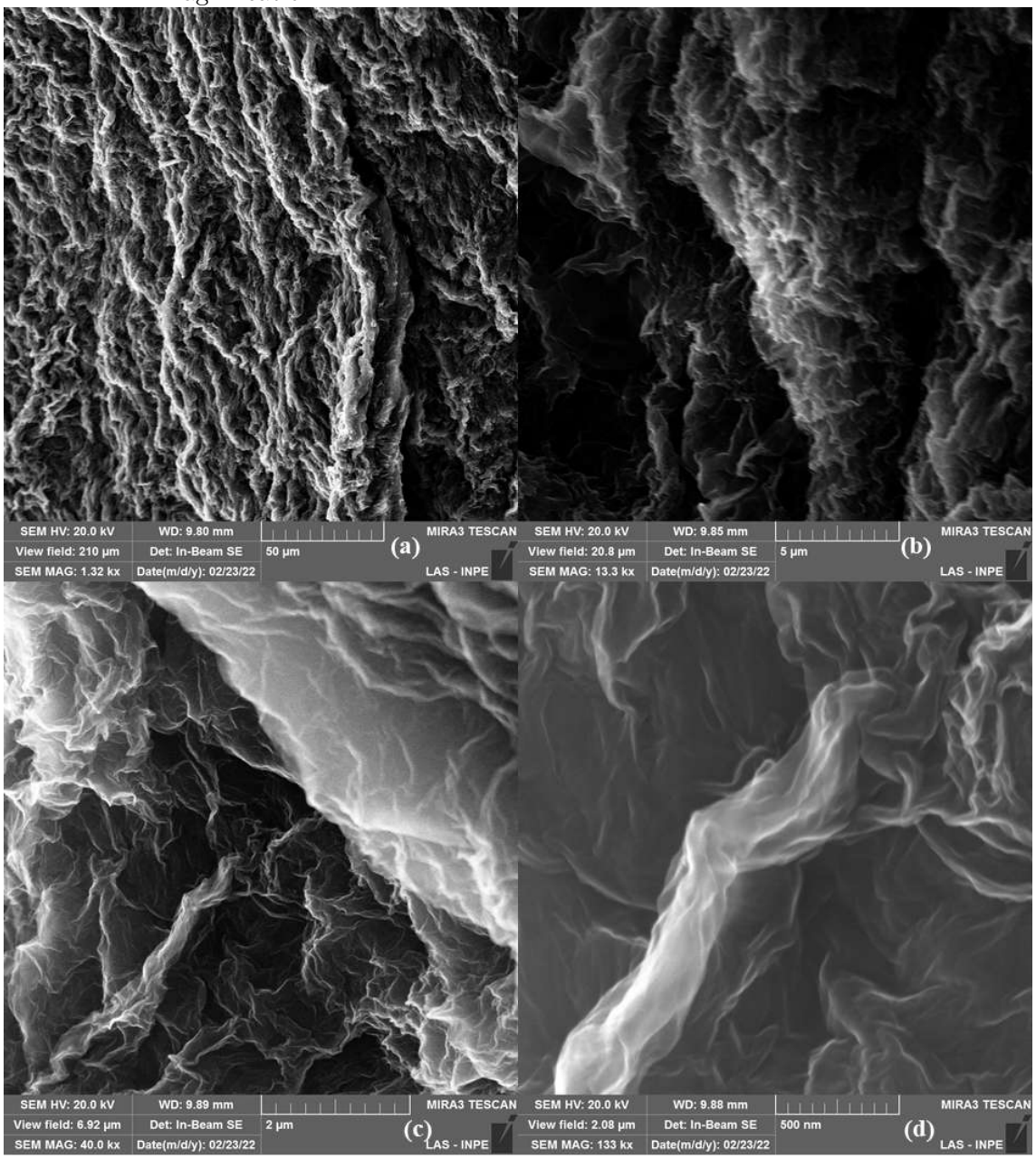

Source: Author.

Figure 4.17 - SEM images of Zn-rGO_S with (a) 1 kx, (b) 10 kx, (c) 30 kx and (d) 100 kx magnification.

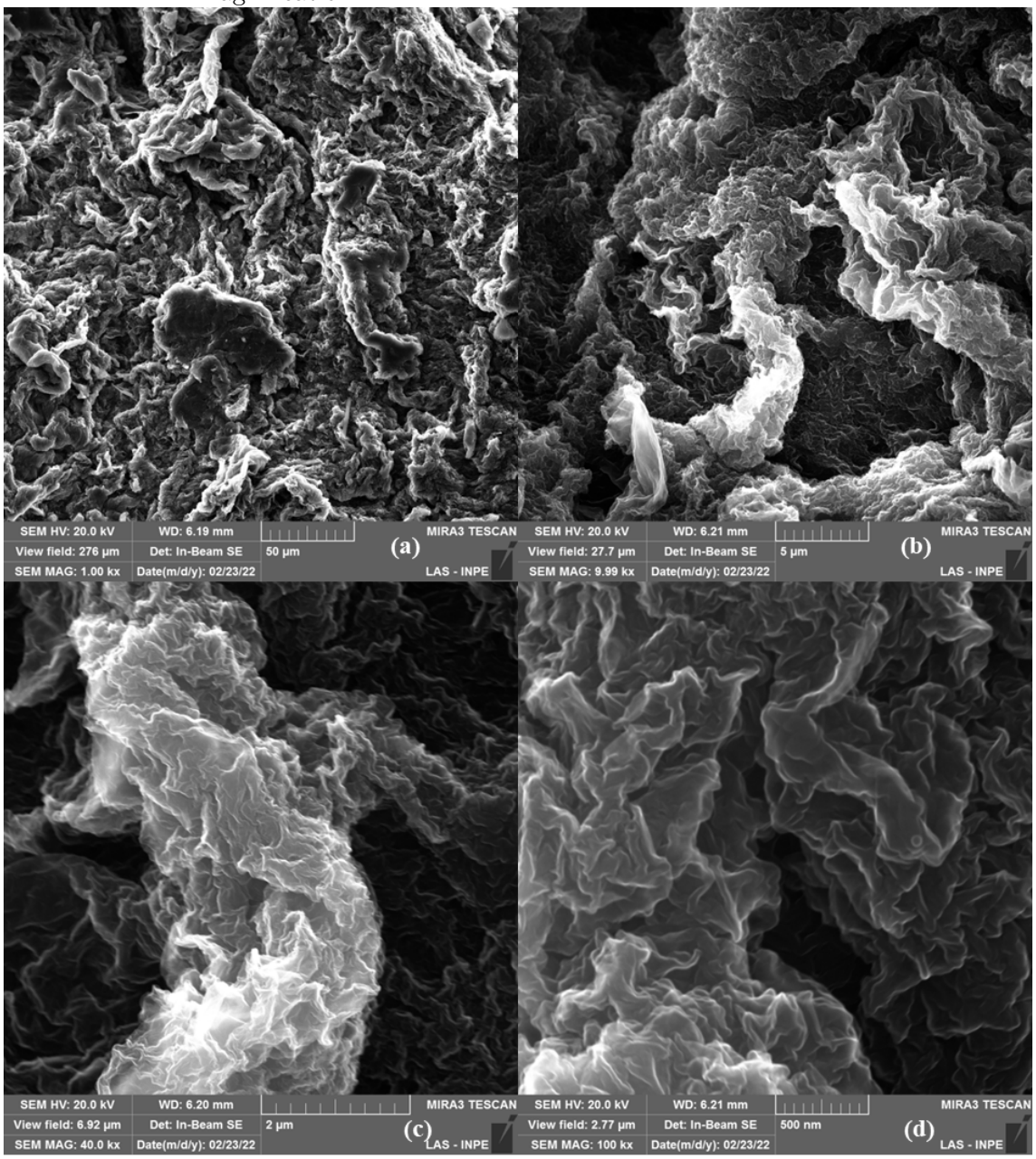

Source: Author.

Figure 4.18 - SEM images of Cu@Zn-rGO_P with (a) 1 kx, (b) 10 kx, (c) 30 kx and (d) 100 kx magnification.

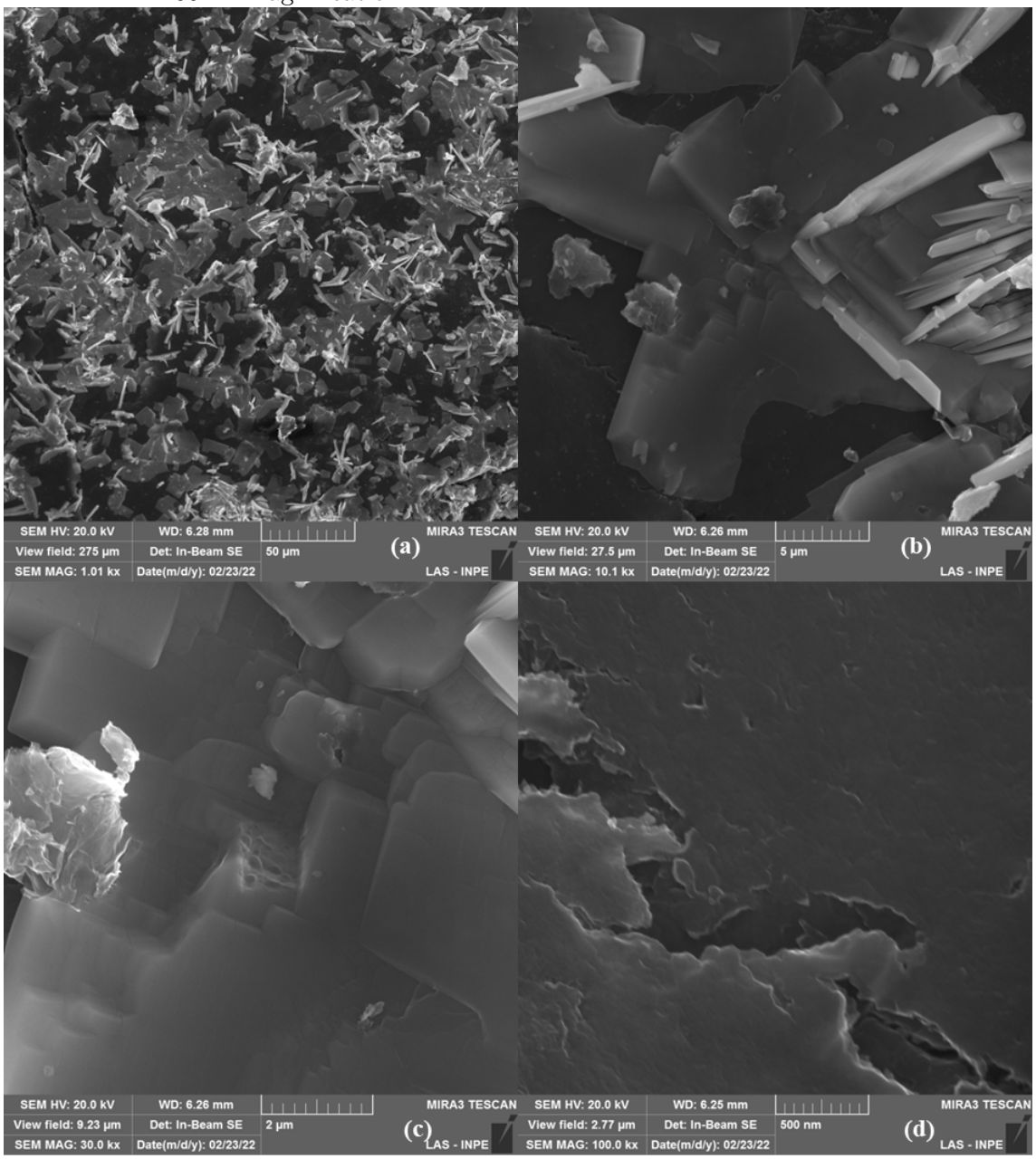

Source: Author.

4.2.5 Raman spectroscopy

The Raman spectra were collected for all the studied rGO, supports and catalysts. Generally, the spectra of graphite-like materials show a highly intense peak denoted as the G band at approximately 1584 cm^{-1}, representing the vibration of sp^2 carbon atoms present in the graphene layers. The D band is another well defined peak with maximum found at ~1530 cm^{-1} in materials containing high defect concentration, vacancies or dislocations at the edge of graphene layers. The presence of defects also results in the appearance of the D' band (1620 cm^{-1}) (MUZYKA et al., 2018).

In this study, the first order Raman was considered, as well as the D' band. In order to identify and analyse all bands, deconvolution and integration were performed using Voigt curve fittings. Figure 4.19 presents the normalized spectrum and peak deconvolution obtained for rGO_S as an example. The bands identified were D, G, D' and an additional broad band in the range 1497 - 1542 cm^{-1}, which was denoted as O band. The G band is not dispersive, therefore the position was fixed at 1584 cm^{-1} for the fitting procedure (ANTUNES et al., 2006). The obtained band positions and I_D/I_G integrated intensity ratio for all samples are shown in Table 4.6.

Figure 4.19 - Deconvolution of the spectrum obtained for rGO_S.

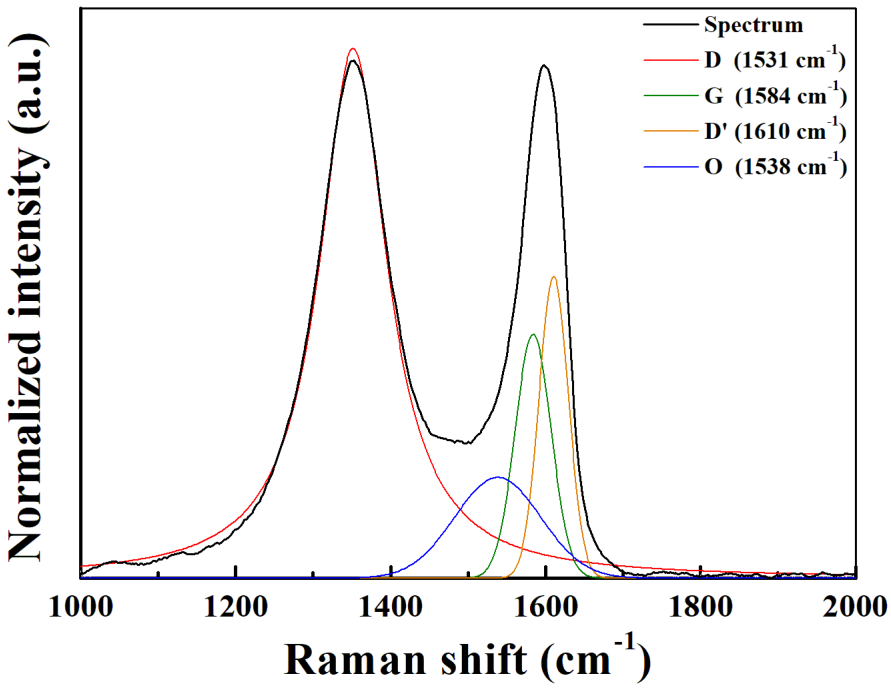

Source: Author.

For the rGO samples, the Raman spectra obtained are presented in Figure 4.19. As mentioned above, the observed well defined D band at about 1350 cm^{-1}, along with the D' and G bands which appeared when deconvoluting the peak at 1600 cm^{-1}. The intensity ratio of D and G bands determined were above 1, suggesting highly disordered structures (MENDOZA et al., 2019). In this case, it could suggest that the addition of surfactants lowered the defects concentration, even though all samples would still fall under the high disorder category, according to the authors. However, as no correlation was identified between usage of surfactants and I_D/I_G ratio, it is difficult to confirm the hypothesis. Moreover, the surfactants employed did not cause significant changes to the position of D, D' and O bands.

Figure 4.20 - Raman spectra obtained for the rGO samples.

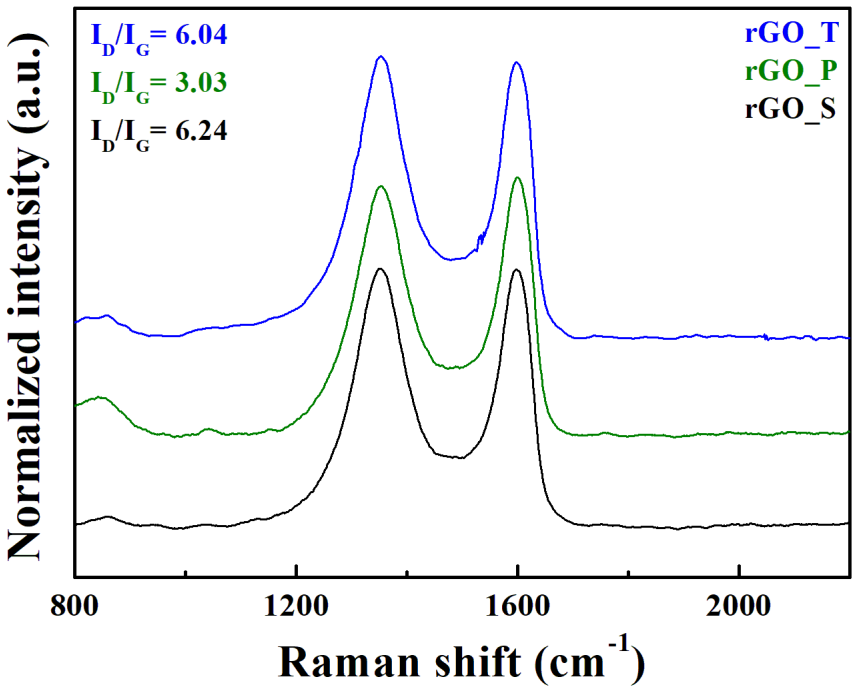

Source: Author.

In some studies, the O band observed is often denoted as D" and attributed to the oxygen content in a GO sample, which in turn may be used as a means of identifying the reduction level of rGO. By using 532 nm excitation wavelength, (CLARAMUNT et al., 2015) observed a shift in the D" band position towards 1500 and 1550 cm^{-1} as oxygen content (%) decreased or increased, respectively. From the O band positions observed in this study, it may be inferred that the graphene reduction degree is

equivalent to the obtained by the authors when employing thermal treatment at more drastic conditions of 300 °C and vacuum in the reduction method, indicating that the hydrothermal procedure may be more effective in reducing GO. However, a small difference is expected due to slightly different wavelengths used.

The spectra obtained for the supports and catalysts are presented in Figure 4.21, the same procedure described previously was used to deconvolute bands, obtaining the results exhibited in Table 4.6. It was observed that the materials also presented I_D/I_G ratio higher than 1, resulting from defects concentration. Bands positions were also not significantly altered neither when adding zinc or copper, nor surfactants, with the exception of the Cu@Zn-rGO_T catalyst, which presented the O band at 1497 cm^{-1}. Following the correlation found by (CLARAMUNT et al., 2015), this would suggest that this catalyst present the lowest oxygen content of all samples studied. The cause of this effect is not clear, as the impregnated catalyst and hybrid support containing Triton did not present this behavior.

Figure 4.21 - Raman spectra obtained for the supports and catalysts samples.

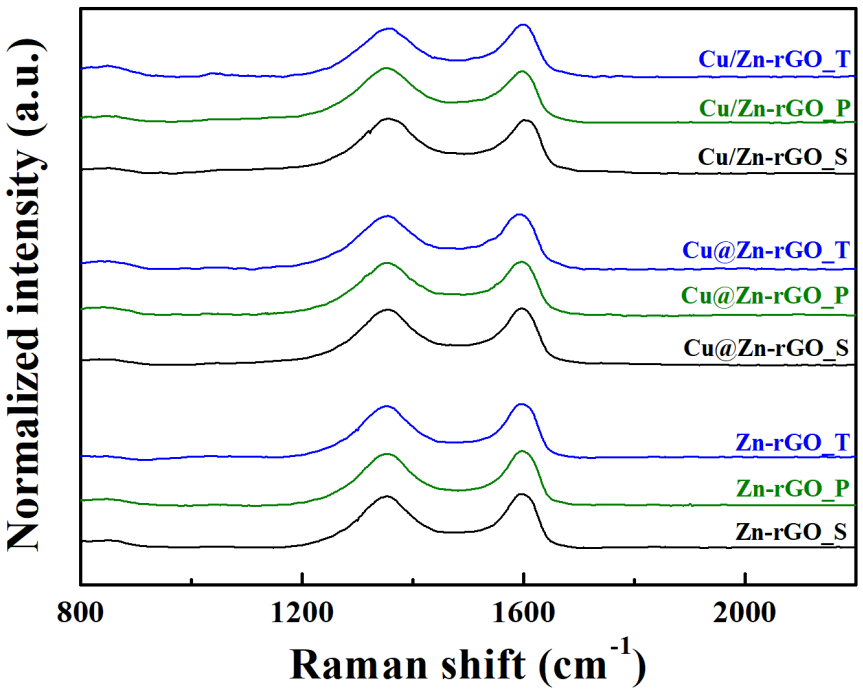

Source: Author.

Table 4.6 - Band position and I_D/I_G intensity ratio.

Sample	D	D'	O	
	Position (cm^{-1})			I_D/I_G
rGO_S	1351	1611	1538	6.0
rGO_P	1354	1613	1521	3.0
rGO_T	1352	1614	1537	6.2
Zn-rGO_S	1350	1612	1513	2.4
Zn-rGO_P	1351	1612	1533	5.0
Zn-rGO_T	1350	1612	1530	4.1
Cu@Zn-rGO_S	1353	1611	1542	5.2
Cu@Zn-rGO_P	1352	1610	1511	4.4
Cu@Zn-rGO_T	1351	1601	1497	3.1
Cu/Zn-rGO_S	1356	1613	1504	3.8
Cu/Zn-rGO_P	1352	1609	1519	5.6
Cu/Zn-rGO_T	1353	1609	1537	4.7

Source: Author.

Overall, the Raman spectroscopy results suggest that all samples present structures with high defect concentration, characterized mainly by chemical defects, vacancies and induced defects. The presence of defects is a positive property for catalysis, as it may promote the interaction with reactant molecules, rendering instability to the surface of the solid. The addition of surfactants did not cause significant changes in the spectra and no correlation was found with intensities ratio or band position.

4.3 Catalytic tests

4.3.1 Optimization of reaction conditions

Prior to the experiments with the rGO supported materials, the catalytic unit was tested with the commercial $Cu/ZnO/Al_2O_3$ catalyst, the pressure condition was optimized following the results for these tests, which were carried out using the parameters described in Section 3.3. Figure 4.22 presents the results obtained, the data shown was taken at 3 hours on stream with the dot line representing the initial conversion values determined at 0.5 h of reaction. It was observed that the initial conversion increased continuously with pressure, reaching 31% at 30 bar. Nevertheless, after 3 hours on stream the conversion dropped to less than 5%, indicating a striking catalyst deactivation (Figure 4.23). A discussion of the deactivation is presented in a subsequent section.

Methanol STY also increased with pressure, whereas the Y_{CO} exhibited a maximum at 20 bar, decreasing for higher pressure conditions. The catalytic activity in terms of methanol formation is explained by the equilibrium shift as pressure increases, according to Le Chatelier's principle for a reaction that occurs through a volume contraction ($CO_2 + 3\,H_2 \rightleftharpoons CH_3OH + H_2O$), as is observed in several previous studies (ALVAREZ et al., 2017; SAEIDI et al., 2014; YANG et al., 2017; YE et al., 2019). Industrially, the reaction is performed using syngas as reactant more drastic conditions ($\sim$ 50 - 100 bar) in order to inhibit RWGSR, favoring methanol formation and enhancing the selectivity to the desired product. In contrast, the Y_{CO} profile suggests the occurrence of RWGSR ($CO_2 + H_2 \rightleftharpoons CO + H_2O$), an endothermic reaction promoted at higher temperatures ($>$ 300 °C) and low pressures. Furthermore, the secondary reaction of CH_3OH decomposition ($CH_3OH \rightleftharpoons CO + H_2$) could also have contributed to the CO formation. Nevertheless, DME formation was not observed independently of the pressure condition, which is plausible as the experiments were performed in the absence of acid catalysts.

As the best result in terms of methanol STY was obtained using P = 30 bar, all posterior tests were performed using this pressure condition, also with T = 250 °C and GHSV = 3000 h^{-1}.

Figure 4.22 - CO_2 conversion, Methanol STY and CO yield obtained in each pressure.

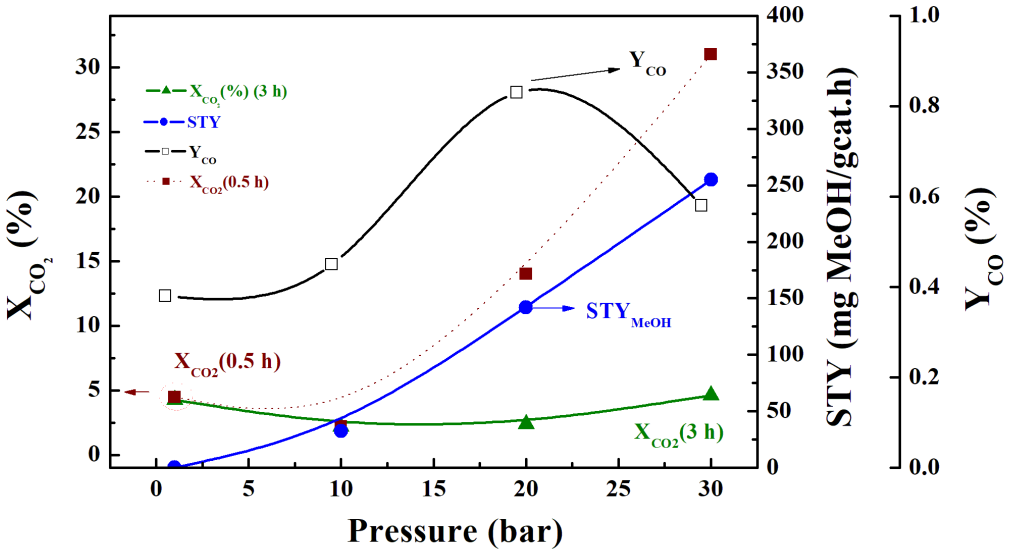

Source: Author.

Additionally, three physical mixtures of $Cu/ZnO/Al_2O_3$ and acid catalysts were tested in the attempt to dehydrate methanol to DME and evaluate the effect on CO_2 conversion. The acid catalysts used were γ-Al_2O_3, Nb_2O_5 and $36\%Nb_2O_5/\gamma$-Al_2O_3. For comparison, the experiments were carried out with the same parameters described previously, using 30 bar reaction pressure. The conversion over reaction time is presented in Figure 4.24 and the overall results are summarized in Table 4.7. It may be observed that alumina had a negative effect on catalyst activity, presenting only 8% CO_2 conversion at 0.5 h on stream, whereas $36\%Nb_2O_5/\gamma$-Al_2O_3 exhibited higher initial conversion followed by a striking deactivation, $\sim$3% at the end of 3 hours. Among the acid catalysts, Nb_2O_5 led to the best performance of the catalyst in terms of stability, with an intermediate initial conversion of 27% but with less accentuated deactivation. These results can interpreted in terms of the acid surface strength of the catalyst. It is well-known that water can adsorb irreversibly on strong acid sites, which is still a problem during CO_2 hydrogenation to methanol and DME, since water is a by-product from both reactions (XU et al., 1997).

Figure 4.23 - CO_2 conversion over reaction time obtained for the commercial catalyst.

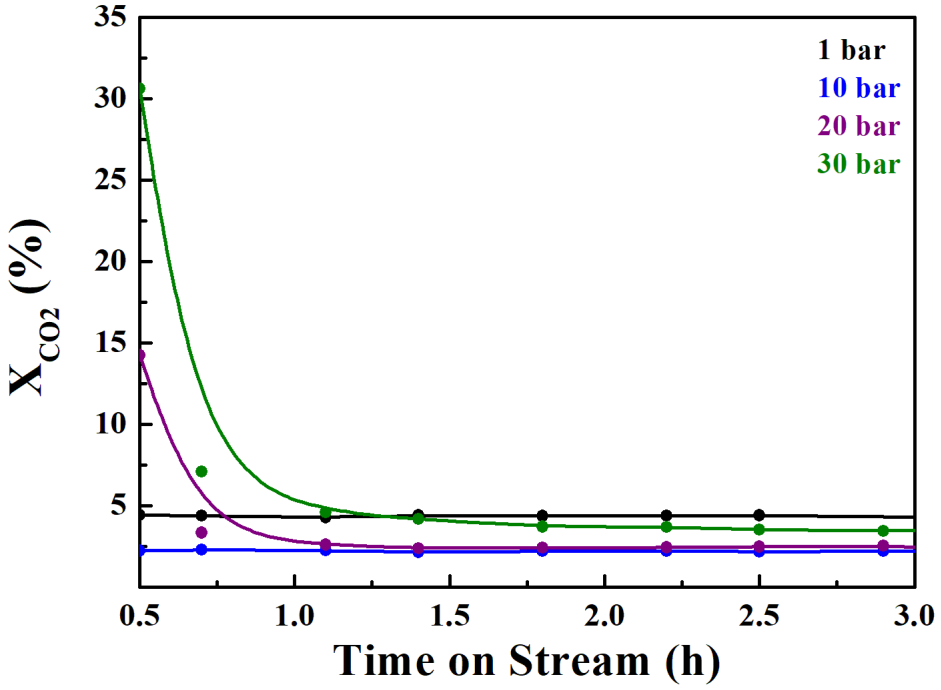

Source: Author.

By analyzing the results present in Table 4.7, it is possible to observe that the acid catalyst 36%Nb_2O_5/γ-Al_2O_3 was more efficient towards DME yield. Again, this result can be associated to the acid surface composition. Even though the evaluation of the acidic surface of the catalysts is beyond the scope of this study, the described results allow inferring the deactivation observed was promoted by γ-Al_2O_3 specifically for its strong acid sites, considering the sample containing γ-Al_2O_3 deactivated continuously during time on stream.

Figure 4.24 - CO_2 conversion over reaction time obtained for $Cu/ZnO/Al_2O_3$ + acid catalysts.

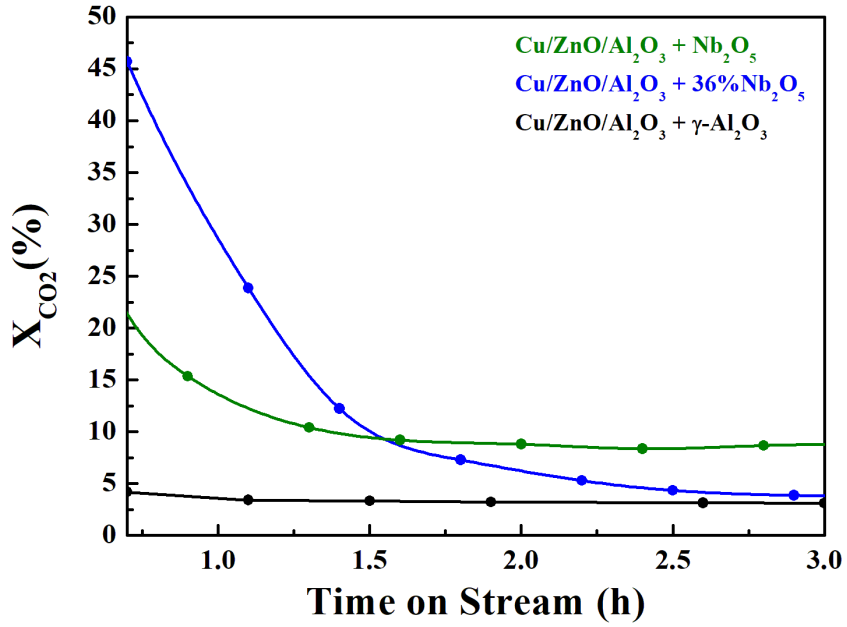

Source: Author.

Table 4.7 - Results obtained for the physical mixtures with acid catalysts.

Catalyst	X_{CO_2} (%)	STY (mg MeOH/gcat.h)	DME Yield (%)	CO Yield (%)
$Cu/ZnO/Al_2O_3$	5	242.14	-	0.58
γ-Al_2O_3	3	141.39	1.89	0.26
$36\%Nb_2O_5$	3	85.81	3.32	0.45
Nb_2O_5	8	85.46	1.24	0.44

Source: Author.

The methanol STY obtained was lower for all acid catalysts, specially for Nb_2O_5. As the liquids were collected in the condenser by the end of the reaction, it was possible to determine the volume of product and concentration. All chromatrograms obtained by FID showed a single peak attributed to methanol, therefore the liquid products consist of methanol and water only. For the γ-Al_2O_3 catalyst mixture, a small volume of liquid products was obtained ($\sim$0.1 mL), however, the methanol concentration was around 72%, thus resulting in methanol STY higher than the acid catalysts counterparts. A similar volume was obtained when using $36\%Nb_2O_5$, but

with significantly lower methanol content. As for the Nb_2O_5 mixture, the formation of a large quantity of liquid was observed, but with the lowest methanol concentration. This is explained by the dehydration of methanol to DME observed, while for the $Cu/ZnO/Al_2O_3$ the reaction did not proceed. For $36\%Nb_2O_5$, the lowest quantity of methanol formed may be explained by the highest DME yield, justifying the higher liquid volume obtained with lower methanol concentration, as water is also formed in the methanol dehydration.

Furthermore, as observed from the results (Table 4.7), CO yield was lower for the acid catalysts than for $Cu/ZnO/Al_2O_3$, suggesting inhibition of the RWGSR.

4.3.2 rGO supported catalysts

The catalytic tests with the rGO supported materials were carried out following the procedure described in Section 3.3, in all experiments the pressure condition used was 30 bar. The results are presented in terms of CO_2 conversion. Figure 4.25 shows the conversion obtained with the reference catalysts Cu/ZnO, Cu@rGO_S and Cu@rGO_P, which initially presented CO_2 conversion of 37, 12 and 2%, respectively. By the first hour on stream, the activity had decreased significantly for all materials, reaching almost 0 for the Cu@rGO catalysts and 1% for Cu/ZnO. By physically mixing copper and zinc oxides, (VALANT et al., 2015) had also obtained 1% CO_2 conversion, however, the catalyst was highly selective to methanol. In this case, the material only promoted the RWGSR, as CO was identified but no liquid products were formed. As for the rGO supported, the lack of the ZnO phase may have hindered CO_2 adsorption, as the synergistic effect of Cu and Zn may be required for activating carbon dioxide (LIU et al., 2003).

Figure 4.25 - Results of catalytic tests performed with the reference catalysts.

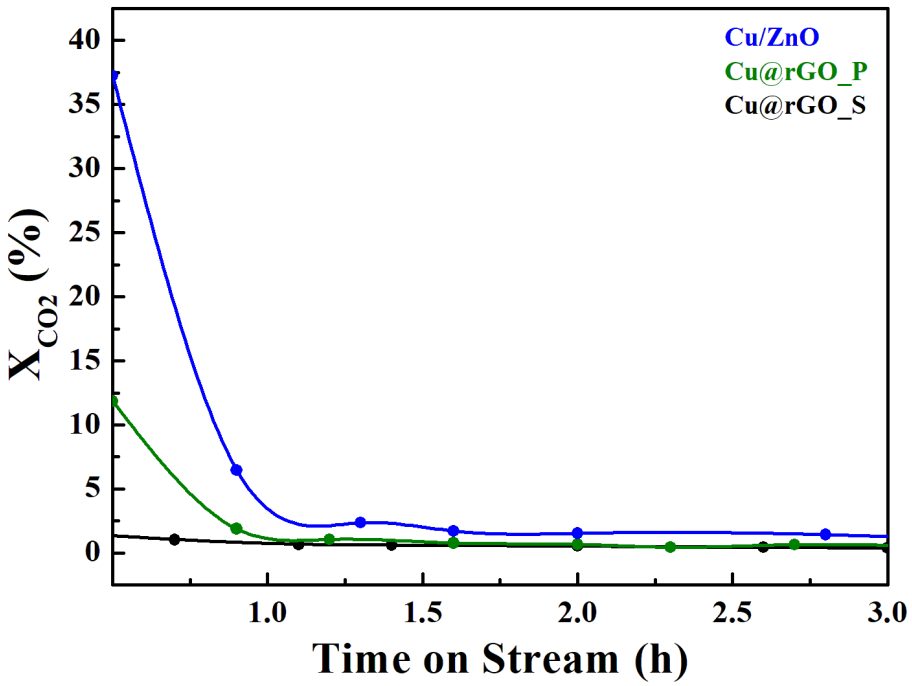

Source: Author.

The results obtained for the catalysts prepared through the hydrothermal method

are presented in Figure 4.26. Similarly to the references, the surfactant-free and Pluronic samples started the reaction with considerable CO_2 conversion (around 30%), then showed significant deactivation by 1 h of reaction time, although Cu@Zn-rGO_S maintained conversion to some extent until 2.2 h on stream, when another deactivation stage began, leading to 1% CO_2 conversion. As the Pluronic material had almost completely deactivated by 1.5 h of reaction, the surfactant may have had a negative effect on the catalyst performance. During the reduction stage, the GC detectors were monitored, as the Triton-containing sample was barely active, this may be explained by the consumption of the surfactant during the reduction step, in which an intense peak was identified in FID only when using this catalyst, possibly causing collapse of the graphene structure, and therefore resulting in poor activity. Given the complexity of the Triton X-100 molecule, confirmation of the substance by MS was not possible, hence, it is also possible that the peak is related to surface groups of the surfactant, which would not cause collapse of the structure. Nevertheless, as reduction was carried out at 300 °C, this result would be in agreement with the TG analysis (Figure 4.8), in which the major mass loss started at 200 °C for this sample only. However, to further confirm the effect, a TG analysis using H_2 atmosphere would be required. Furthermore, the one-step hydrothermal reduction of GO introducing two metal phases simultaneously to synthesize catalysts for the CO_2 hydrogenation is a completely novel procedure, so the literature does not provide additional information on the materials. Hence, preparing the catalysts through this methodology may lead to unforeseen consequences in terms of interaction of copper and zinc phases.

Figure 4.27 exhibits the CO_2 conversion obtained for the impregnated catalysts. The reduction step for the Triton sample presented the same behavior as mentioned previously, which is another indicative of the surfactant consumption and causing collapse of the structure, resulting in almost no activity right from the beginning of the experiment. The Pluronic sample present similar profile, with almost no activity during the test. As for Cu/Zn-rGO_S, deactivation occurred quickly in a single stage, resulting in 1% CO_2 conversion. The synthesis of graphene supported catalysts by wetness impregnation for the hydrogenation reaction has been reported by (DEERATTRAKUL et al., 2018), in which it was obtained 64.77 mg/gcat.h methanol STY with the same copper and zinc loading of the present work. However, the authors prepared the materials by impregnating Cu and Zn on rGO structure simultaneously, while here the copper precursor salt was introduced on Zn-rGO hybrid supports. This suggests that using Zn in the active phase is more appropriate than as support component when employing the impregnation method.

Figure 4.26 - Results of catalytic tests performed with the Cu@Zn-rGO catalysts.

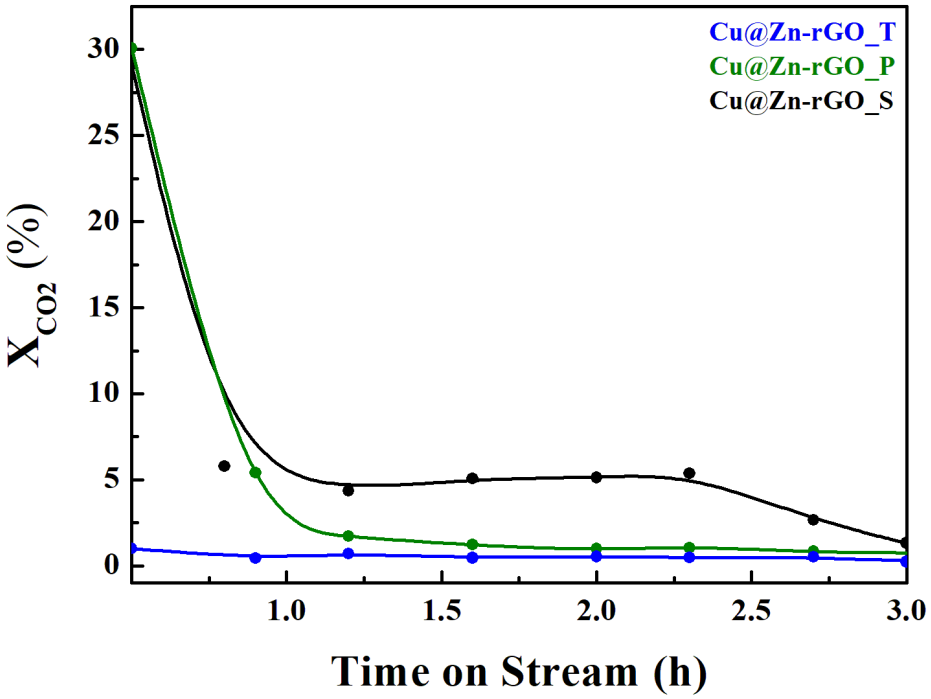

Source: Author.

A summary of the results for the rGO supported materials is presented in Table 4.8. As observed, the catalysts Cu@rGO_P, Cu@Zn-rGO_S, Cu@Zn-rGO_S and Cu/Zn-rGO_S presented significant activity initially (0.5 h reaction time), however, drastic deactivation was observed in all catalysts, therefore understanding the cause of deactivation would be necessary to develop catalysts capable of maintaining high CO_2 conversion to products in long processes. No liquid products were formed during any experiment, meaning that methanol was not obtained. Furthermore, the Flame Ionization Detector showed four peaks of unknown nature at first, but were identified as ethane (C_2H_6), acetaldehyde (CH_3CHO), isopropyl alcohol (C_3H_8O) and butane (C_4H_{10}) using a Mass Spectrometer (MS) coupling installed at the catalytic unit exit. The same peaks were obtained in all tests, as the retention times were very similar in every experiment. However, quantification of these compounds were not possible, as neither the Gas Chromatrograph nor the MS possessed primary standards for calibrations. Additionally, the m/z ratio of 47 was identified in all tests, which among the the MS mass spectra of hydrocarbons present in the extensive MS library, is only related to a fragment of DME, pointing that a very small quantity of methanol could have been formed during the reactions and dehydrated to DME. It is important to

highlight that this would also indicate a slight acidic nature of rGO, as was already suggested by (FAN et al., 2015), in fact, the tests described here were performed without the use of acid catalysts, aiming to comprehend the role of rGO on the catalysts.

Figure 4.27 - Results of catalytic tests performed with the CuZn-rGO catalysts.

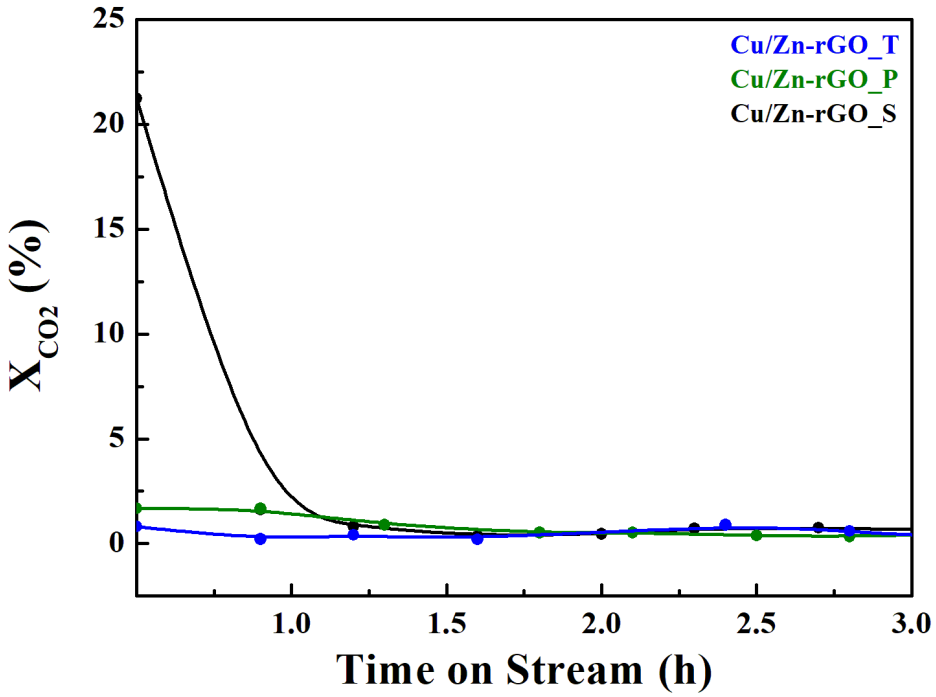

Source: Author.

Table 4.8 - CO_2 equilibrium conversion results.

Catalyst	X_{CO2} (%)	
	0.5 h	3.0 h
$Cu/ZnO/Al_2O_3$	31	5
Cu@rGO_S	2	0
Cu@rGO_P	12	0
Cu@Zn−rGO_S	29	1
Cu@Zn−rGO_P	30	1
Cu@Zn−rGO_T	1	0
Cu/Zn−rGO_S	21	1
Cu/Zn−rGO_P	2	1
Cu/Zn−rGO_T	1	1

Source: Author.

The possible causes for deactivation of the catalysts shall be further discussed in the subsequent section.

4.3.3 Catalyst deactivation

As observed both with the commercial and rGO supported catalysts, rapid deactivation occurred during the experiments. The discussion in this section aims to understanding the phenomenon. Firstly, for copper-based catalysts employed in hydrogenation reactions, it has been reported that the most common deactivation causes are thermal sintering, sulfur or chloride poisoning, carbon deposition and physical damage (TWIGG; SPENCER, 2001). With that in mind, additional characterization analyses were performed with the spent catalysts. As deactivation in the $Cu/ZnO/Al_2O_3$ and rGO supported material may originate from different sources, the discussion will be carried out separately.

4.3.3.1 $Cu/ZnO/Al_2O_3$ catalyst

In order to understand the deactivation of the $Cu/ZnO/Al_2O_3$ catalyst, XRD analyses were performed with the fresh and spent samples to gain insight regarding structural modification during the catalytic tests. Although XRD analysis consists in a bulk characterization technique, it exhibits the advantage of not modifying the oxidation state of species, which may occur when using high vacuum spectroscopy, giving relevant aspects related to structural phases compositions and their interchange, with subsequent modifications. The XRD pattern obtained for the fresh catalysts (Figure 4.28) is characteristic of hydrotalcite (HT) with lamellar structure

($Cu_xZN_{6-x}Al2(OH)16CO3 * 4H2O$), with peaks at 2θ = 11.8, 23.7, 34.7, 39.4, 47.1, 60.2 and 61.1°.

Figure 4.28 - XRD patterns obtained for the fresh $Cu/ZnO/Al_2O_3$ catalysts.

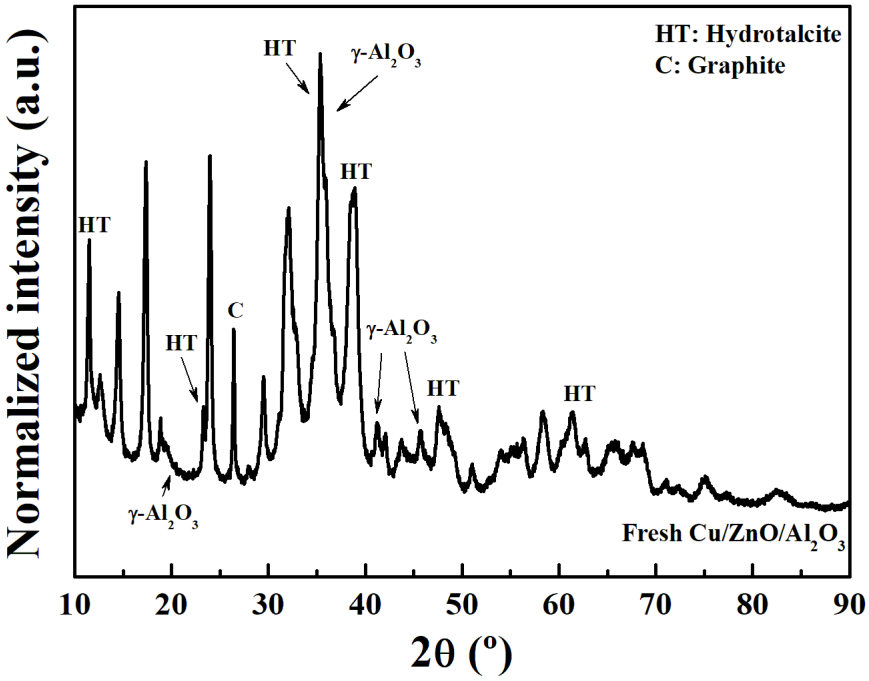

Source: Author.

The appearance of diffraction lines attributed to lamellar HT results from its memory effect, as the phase is lost during calcination but easily recovered upon contact with CO_2 and H_2O. Furthermore, lines corresponding to γ-Al_2O_3 and carbon were identified. The peak related to carbon is originated from the graphite used during the catalyst pelletization as binder.

XRD results obtained for the dilutant SiC and the spent catalysts at the different pressure conditions are presented in Figure 4.29. It was observed that SiC lines overlap with relevant Cu and/or Zn peaks, making the identification of most catalytic phases unfeasible. Nevertheless, the Cu^0 (2θ = 43.2 and 50.3°) phase was identified, although the broadening suggests the presence of other species such as Cu^{+1} and Cu^{+2}. However, Cu^0 is possibly the main phase, considering the peak maximum.

Figure 4.29 - XRD patterns obtained for SiC and the spent $Cu/ZnO/Al_2O_3$ catalysts.

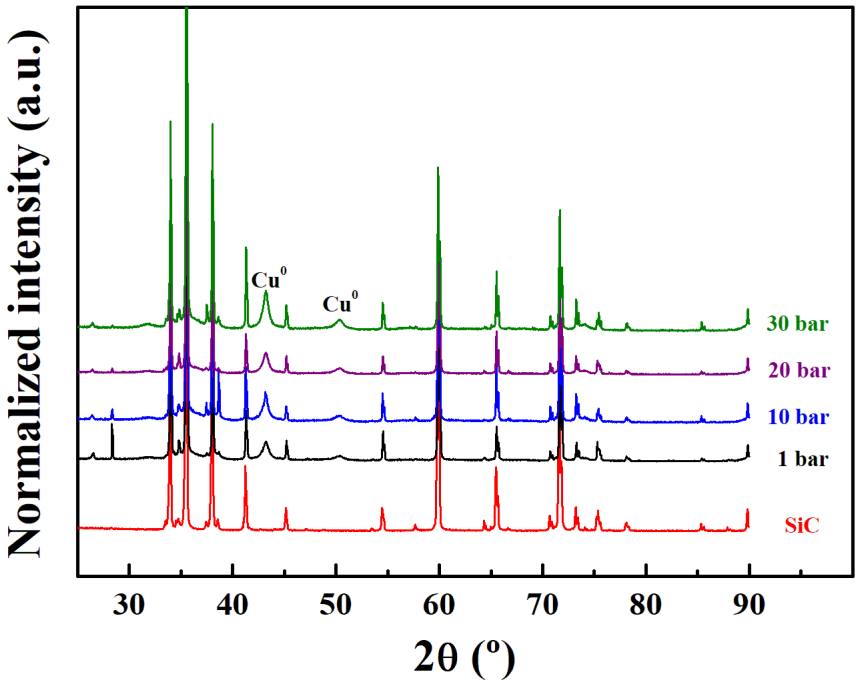

Source: Author.

By amplifying the regions between 33 - 39° and 40 - 55° (Figures 4.30a and 4.30b, respectively), other phases could be distinguished. The peaks centered at $2\theta = 37.6°$ indicate the formation of $CuAlO_2$. Diffraction lines corresponding to ZnO were also observed at $2\theta = 34.2$, 31.9 and 54.7°.

Upon increasing pressure from 1 to 30 bar, the peak at $2\theta = 37.5°$ presented a split to two peaks with maximum at 37.4 and 37.6°, which was not evident for the sample employed at 20 bar, but was observed when using 30 bar reaction pressure. The peak at $2\theta = 37.4°$ may attributed to Al_2O_3, indicating segregation from the $Cu/ZnO/Al_2O_3$ structure, followed by a phase growth at $2\theta = 37.6°$, corresponding to $CuAlO_2$, denoting clustering of Cu and Al. It has been reported that copper alumina $CuAlO_2$ may cause strong deactivation in Cu-based catalysts (MARION et al., 1991).

Figure 4.30 - XRD patterns obtained for the spent $Cu/ZnO/Al_2O_3$ catalysts at the amplified regions.

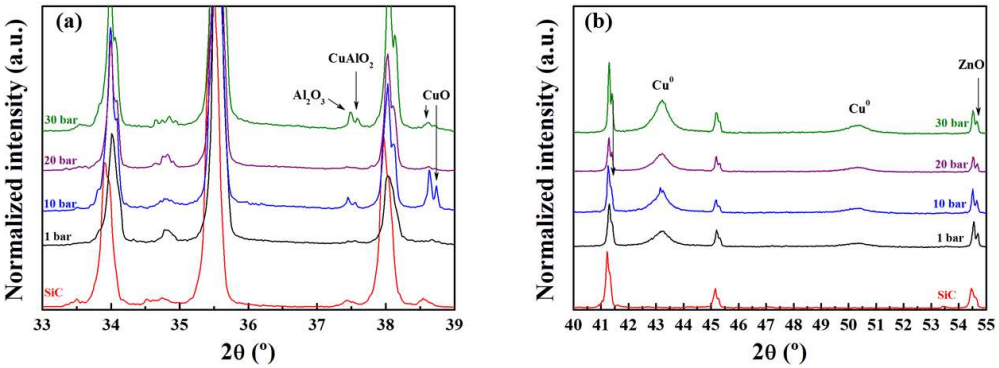

Source: Author.

Overall, the results suggest that deactivation of the $Cu/ZnO/Al_2O_3$ catalyst originates from strong modifications on the microstructure during the tests. This is evidenced by the formation of the inactive species $CuAlO_2$, agglomeration of CuO phases and segregation of Al and Zn. Such modifications may have altered the catalyst structure both geometric and electronically. As discussed in the Literature Review (Section 2.3.2.1), even though the nature of active sites is controversial, the positive synergistic effect of Cu-Zn interaction, therefore it is possible that the modifications inhibited the interplay between copper and zinc.

4.3.3.2 rGO supported catalysts

For the rGO supported materials, initially, the surfactant-free samples had the catalytic performance tested. As already described (Section 3.1.2), in the attempt to prevent layer stacking during the drying step or catalytic reaction, the synthesis procedures were repeated with the addition of surfactants, which have been reported to maintain the structural integrity of rGO (HU et al., 2017). However, while Pluronic only presented a slight decrease in number of layers (Table 4.5), no significant changes were observed in the defect concentration (Section 4.2.5) nor in the catalytic performance. As for the Triton-containing samples, even though a positive effect on number of layers was observed, the surfactant was decomposed during the reduction step, so the lack of activity in this case for both catalysts is attributed to collapse of the graphene structure, due to layer aggregation or removal of structural atoms. In principle, the presence of metals could act as spacer between rGO sheets, preventing agglomeration (ISKANDAR et al., 2018). Nonetheless, the results showed

the Cu and Zn content was not sufficient to keep the structural integrity.

Another possible cause of deactivation would be poisoning due to residual sulfur or chloride from the sulfuric and hydrochloric acids, respectively, employed during the synthesis of GO by the Hummers method. However, no m/z mass-to-charge ratios attributable to compounds containing these elements were detected by the Mass Spectrometer and no phase was identified in the XRD analysis. Hence, the possibility of poisoning is highly unlikely.

Regarding sintering, determination of copper crystallite with the Scherrer equation in the fresh samples was not possible, as the Cu_2O and ZnO peaks were overlapped, as explained previously in Section 4.2.3. However, using the non-overlapped CuO peak at $2\theta = 52.4°$ in the diffractogram obtained for the Cu@Zn-rGO_P catalyst (Figure 4.14), a crystallite size of 18.7 nm was found, suggesting that copper particles might have been already agglomerated in the fresh materials, causing poor metallic dispersion and catalytic performance. For comparison, (DEERATTRAKUL et al., 2018) synthesized a 20%CuZn/rGO catalyst obtaining CuO crystallite size of 9.57 nm. It is worth noticing the relatively high crystallite size of Cu in the rGO samples might be originated from the interaction between Cu precursor and the oxygen functionalities of GO. It is known that the main oxygen groups decorating GO nanosheets are phenolic hydroxyl (-OH), epoxy (C-O-C), carboxyl (COOH) and carbonyl (C=O), among others (PAREDES et al., 2008). These oxygen species are reactive and may interact with the metal precursor, influencing its metallic dispersion, which in turn will also depend on the metal nature. Recently, our group reported a study where Pd was deposited on the hybrid 30%CeO_2-rGO at the nanoscale, with particle size below 3 nm. Likewise, it was evidenced that CeO_2 was deposited on rGO as nanostructures, which was essential to provide the high dispersion for Pd nanoparticles. Interestingly, in the absence of CeO_2 the Pd was heterogeneously deposited with the co-existence of small and large particles, pointing out the interaction degree between metal and rGO. However, in this study, additional characterization such as N_2O chemisorption and Transmission Electron Microscopy (TEM) would be required to confirm the effect.

In the attempt to observe modification in the catalyst structure during the catalytic test, Raman spectroscopy analysis was performed with the spent Cu@Zn-rGO_P catalyst. A comparison between the spectra obtained for the fresh and spent samples is presented in Figure 4.31. Even though the sample is still disordered, as evidenced from the presence of D and D' bands (D' was observed after deconvolution), a

significant decrease in the I_D/I_G ratio was found. Accordingly, the chromatograms along with the mass spectra obtained during the reduction step of all catalysts revealed the formation of the same hydrocarbons described previously in Section 4.3.2. These results would suggest that surface or structural atoms are possibly being consumed during reduction with H_2, with the latter hypothesis resulting in a more negative effect, which could lead to the collapse of the structure. Furthermore, even though the GC does not contain standards for these hydrocarbons and therefore quantification of the compounds was not possible, the area under the peaks observed during reduction was significantly higher than the are of the signals obtained during reaction, corroborating the hypothesis, as the reactant mixture contains 75% vol. of H_2, while the reducing flow is pure.

Figure 4.31 - Raman spectra obtained for fresh and spent Cu@Zn-rGO_P catalysts.

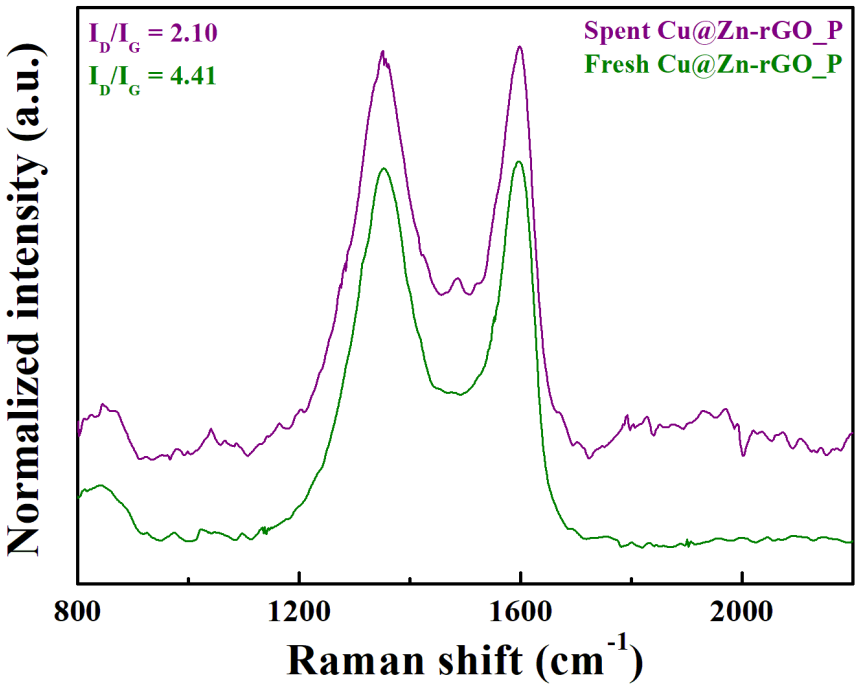

Source: Author.

Additionally, another test was performed with Cu@Zn-rGO_P using 500 mg of the material, in order to check if the lack of activity was simply due to insufficient amount of active phase, as the synthesized and commercial catalysts contained 10% and 50% copper, respectively. While no significant increase in CO_2 conversion was observed,

the area under the peaks obtained during reduction was notably higher, further confirming that the compounds were formed by reaction of the graphene structure and/or surface groups with hydrogen, as increasing the quantity of catalyst increased the amount of hydrocarbons formed.

To gain insight on the effect of temperature on the formation of hydrocarbons during the reduction step, another test was carried out following the same methodology described in Section 3.3, however, the catalyst was reduced at 250 °C, and the products formed were monitored by FID during the temperature rise. Interestingly, at low temperatures (<200 °C), no peaks were detected. At 220 °C, the hydrocarbons signals appeared, indicating that in order to prevent this effect, reduction should be performed at temperatures below 200 °C, however, it may not be sufficient for obtained the active phase desired, although a Temperature Programmed Reduction (TPR) analysis would be required to reveal the minimum temperature necessary. Moreover, given that Cu_2O was observed in the diffractograms, it is also possible that the reduction time or temperature employed is insufficient to obtain the metallic phase. However, the thermal stability would need to be assessed through TG analysis under hydrogen atmosphere.

Overall, the analyses performed are insufficient to affirm that the degrading of graphene structure observed is the cause, or one of the causes for the deactivation of the catalysts, as several other factors could still be considered. It is possible that the active sites are not accessible to the reactant molecules, or as suggested by the XRD analysis, Cu particles undergo agglomeration during the material synthesis procedure, such information would require characterization techniques such as Transmission Electron Microscopy (TEM). Is is also possible that the Cu/Zn ratio used was not adequate for the catalyst activity. Nevertheless, as graphene-based catalysts for the CO_2 hydrogenation reaction are still at the early stages of development, studies regarding deactivation and detailed information on the interaction of the active phases with rGO are scarce.

Even though the catalysts presented low activity, the research presents novel aspects, given that there are very few reports of rGO-supported catalysts and no studies regarding the use of surfactants for CO_2 hydrogenation. Also, advancement was made with the addition of Triton, as it allows rapid material drying at room temperature without the use of expensive techniques such as freeze-drying or CO_2 supercritical conditions.

As a suggestion regarding the synthesis procedures, impregnating the metal phases

simultaneously on a rGO structure may result in a more direct contact between the phases, unlike the impregnation of Cu onto Zn-rGO hybrid supports. The Cu/Zn ratio may also be optimized, as it may affect the catalytic performance. To better understand the behavior of active sites in the rGO-supported catalysts, in situ characterization methods such as Infrared (IR) spectroscopy could provide information of whether intermediates are being formed or CO_2 is not being activated by the catalysts. Furthermore, the catalytic tests could be performed at mild temperature and pressure conditions, in order to assess the effect on the performance.

5 CONCLUSION

The aim of this research was the development of rGO supported catalysts for the hydrogenation of CO_2, a highly relevant reaction for this century in terms of sustainability and production of high value-added products. The synthesis procedures from oxidation of graphite to graphene oxide to the hydrothermal reduction of GO and introduction of active phases were performed successfully, obtaining materials with different aspects when adding surfactants. The methodology included a novel one-step hydrothermal reduction procedure for the synthesis of catalysts containing Cu and Zn.

Several characterization techniques were applied in order to understand the properties of the materials prepared. Overall, the thermal stability of the catalysts and supports are adequate for the temperature range employed in CO_2 hydrogenation, with the exception of the samples containing the Triton X-100 surfactant, which presented degrading of the structures at temperatures below 200 °C.

The X-Ray Diffraction analyses revealed that the graphene structure was maintained during the synthesis procedures, while the copper oxidation states varied according to the catalyst synthesis method employed. The results also suggests, that incorporating a single metal on the hydrothermal reduction produces highly dispersed phases, while incorporating multiple metals may generate more crystalline structures.

Raman spectroscopy showed that rGO as well as the supports and catalysts present highly disordered structures, characterized by the D and D' bands and high I_D/I_G intensity ratio, suggesting the presence of functional groups, defects and vacancies. A band related to the reduction degree of the samples was also observed, indicating that some oxygen still remains in the graphene structure.

The specific surface area of the materials was determined by methylene blue adsorption. The remarkably high values obtained, ranging from 272 - 920 m^2/g, suggest a positive effect of the surfactants, as the decrease in specific surface area when adding metals was less pronounced on the surfactant-containing samples. Interestingly, it was observed that when using Triton the surface area for the support and catalyst was very similar.

The catalytic unit used for the experiments was tested with a commercial $Cu/ZnO/Al_2O_3$ catalyst at different reaction pressures prior to the experiments with

the rGO supported materials. It was confirmed that higher pressure conditions result in improved performance in terms of CO_2 conversion and methanol space-time yield, while also inhibiting the reverse water gas shift side reaction. Additionally, DME was obtained when mixing $Cu/ZnO/Al_2O_3$ with acid catalysts. It was observed that the addition of Nb_2O_5 enhanced CO_2 conversion and maintained stability of the material. The spent catalysts were characterized by XRD, being evidenced profound microstructural modifications. Even though the study of $Cu/ZnO/Al_2O_3$ was outside the scope of the present work, the results found are relevant, as the behavior of the catalyst is still debated to this day.

As for the catalytic tests with the rGO supported catalysts, the Cu@rGO_P, Cu@Zn-rGO_S, Cu@Zn-rGO_P and Cu/Zn-rGO_S samples presented significant activity at the start of the tests, although rapid deactivation was observed in all experiments, as conversion almost reached 0% over three hours of reaction time. Several hypothesis were raised as to the cause(s) of deactivation and additional characterization was performed in the attempt of understanding the changes in the material structure during the tests. Sulfur and chloride poisoning is highly unlikely, as the species were not detected by the Mass Spectrometer. Evaluation of sintering by XRD analysis was not possible as the copper and zinc peaks were overlapped. Raman spectroscopy performed with a spent catalyst indicates a decrease in defects concentration. It was observed that reducing the catalysts at 300 °C with H_2 flow may have degraded the graphene structure, pointed by detection of hydrocarbons by the Flame Ionization Detector and Mass Spectrometer. However, it is not possible to affirm that this is the major cause for deactivation. Furthermore, even though the reactions were performed in the absence of acid catalysts, traces of DME were confirmed by Mass Spectrometry. All these factors make the understanding of the cause of deactivation of rGO-supported catalysts worth investigating.

Overall, the study contributes to the understanding of the CO_2 hydrogenation reaction, while investigating the properties of graphene based materials, which are receiving considerable interest not only in the catalysts field, but also several other areas of knowledge. As rGO supported catalysts for this reaction are still in an early stage of development, the literature still lacks detailed information on the interaction between support and active phases, as well as possible specific deactivation modes that are not general for any copper catalyst. Also, using rGO-supported catalysts allows the recovery of transition or noble metals employed, making this alternative also promising in terms of sustainability. Nevertheless, the importance of converting CO_2 to products, the fact that the behavior of active sites are still controversial, the

necessity of optimizing the reaction and developing novel low cost catalysts, making it economically viable are all factors that highlight the importance of the present work.

Additionally, even though using Triton X-100 did not improve catalytic activity, the surfactant maintained the structural integrity of rGO, while also allowing rapidly drying at room temperature, avoiding expensive procedures. This finding is highly relevant for research on the synthesis of graphene-based materials, which possess remarkable physicochemical properties and wide range of applications.

Lastly, with the information gathered and insight gained, a few recommendations for future research may be made. Both the hydrothermal reduction and wetness impregnation synthesis procedures may be carried out by introducing Cu and Zn simultaneously, in order to evaluate the difference in active phases obtained in the final material. A hybrid support Al_2O_3-rGO could also be prepared, with posterior impregnation of copper and zinc sequentially or concurrently, this would provide a better comparison with the widely studied $Cu/ZnO/Al_2O_3$ catalysts. Also, different active phases such as Pd might yield improved results in terms of catalytic performance. Thermal stability analysis in both H_2 and CO_2/H_2 atmospheres would provide valuable information on the behavior of graphene based materials to be employed in hydrogenation reactions. Transmission Electron Microscopy (TEM) is a good alternative to a better comprehension of the active sites produced. In situ characterization techniques are fundamental for assessing modifications in structure, phases and integrity of the material, as well as to understand the mechanism of the reaction when using novel catalysts. After obtaining a stable graphene based catalysts, the optimization of reduction and reaction parameters, specially temperature, pressure and space velocity may provide interesting results. Finally, a long-term stability test under the reaction conditions would be required in order to start the research on industrial application. Overall, the novel rGO materials have room for improvement in several aspects.

REFERENCES

AHMAD, K.; UPADHYAYULA, S. Greenhouse gas CO_2 hydrogenation to fuels: a thermodynamic analysis. **Environmental Progress & Sustainable Energy**, v. 38, n. 1, p. 98–111, 2019. 12, 13

ALAM, S. N.; SHARMA, N.; KUMAR, L. Synthesis of graphene oxide (go) by modified hummers method and its thermal reduction to obtain reduced graphene oxide (rgo). **Graphene**, v. 6, n. 1, p. 1–18, 2017. 63

AN, X.; LI, J.; ZUO, Y.; ZHANG, Q.; WANG, D.; WANG, J. A cu/zn/al/zr fibrous catalyst that is an improved co2 hydrogenation to methanol catalyst. **Catalysis Letters**, v. 118, n. 3, p. 264–269, 2007. 17

ANTUNES, E.; LOBO, A.; CORAT, E.; TRAVA-AIROLDI, V.; MARTIN, A.; VERÍSSIMO, C. Comparative study of first-and second-order raman spectra of mwcnt at visible and infrared laser excitation. **Carbon**, v. 44, n. 11, p. 2202–2211, 2006. 76

ARCOUMANIS, C.; BAE, C.; CROOKES, R.; KINOSHITA, E. The potential of di-methyl ether (dme) as an alternative fuel for compression-ignition engines: a review. **Fuel**, v. 87, n. 7, p. 1014–1030, 2008. 8

ARENA, F.; BARBERA, K.; ITALIANO, G.; BONURA, G.; SPADARO, L.; FRUSTERI, F. Synthesis, characterization and activity pattern of cu–zno/zro2 catalysts in the hydrogenation of carbon dioxide to methanol. **Journal of Catalysis**, v. 249, n. 2, p. 185–194, 2007. 18

ARESTA, M.; DIBENEDETTO, A.; QUARANTA, E. **Reaction mechanisms in carbon dioxide conversion**. [S.l.]: Springer, 2016. 113, 115

ARIAS, F. A.; GUEVARA, M.; TENE, T.; ANGAMARCA, P.; MOLINA, R.; VALAREZO, A.; SALGUERO, O.; GOMEZ, C. V.; ARIAS, M.; CAPUTI, L. S. The adsorption of methylene blue on eco-friendly reduced graphene oxide. **Nanomaterials**, v. 10, n. 4, p. 681, 2020. 42

ASMAI, R. **X'PERT PRO MRD**. 2021. Available from: <https://mse.engineering.ucdavis.edu/amcat/panalytical-xpert-pro-mrd>. 44

ALVAREZ, A.; BANSODE, A.; URAKAWA, A.; BAVYKINA, A. V.; WEZENDONK, T. A.; MAKKEE, M.; GASCON, J.; KAPTEIJN, F. Challenges

in the greener production of formates/formic acid, methanol, and dme by heterogeneously catalyzed co2 hydrogenation processes. **Chemical Reviews**, v. 117, n. 14, p. 9804–9838, 2017. 12, 20, 80, 115

BARTHOLOMEW, C. H. Mechanisms of catalyst deactivation. **Applied Catalysis A: General**, v. 212, n. 1-2, p. 17–60, 2001. 22

BONURA, G.; CANNILLA, C.; FRUSTERI, L.; MEZZAPICA, A.; FRUSTERI, F. Dme production by co2 hydrogenation: key factors affecting the behaviour of cuznzr/ferrierite catalysts. **Catalysis Today**, v. 281, p. 337–344, 2017. 14, 15, 21, 115

BUSSCHE, K. V.; FROMENT, G. A steady-state kinetic model for methanol synthesis and the water gas shift reaction on a commercial cu/zno/al2o3catalyst. **Journal of Catalysis**, v. 161, n. 1, p. 1–10, 1996. 113, 115, 116, 118

CÁMARA-TORRES, M.; SINHA, R.; EQTESADI, S.; WENDELBO, R.; SCATTO, M.; SCOPECE, P.; SANCHEZ, A.; VILLANUEVA, S.; EGIZABAL, A.; ÁLVAREZ, N. Effect of the reduced graphene oxide (rgo) compaction degree and concentration on rgo–polymer composite printability and cell interactions. **Nanoscale**, v. 13, n. 34, p. 14382–14398, 2021. 53

CHEN, J.; YAO, B.; LI, C.; SHI, G. An improved hummers method for eco-friendly synthesis of graphene oxide. **Carbon**, v. 64, p. 225–229, 2013. 32, 33

CHEN, L.; BATCHELOR-MCAULEY, C.; RASCHE, B.; JOHNSTON, C.; HINDLE, N.; COMPTON, R. G. Surface area measurements of graphene and graphene oxide samples: dopamine adsorption as a complement or alternative to methylene blue? **Applied Materials Today**, v. 18, p. 100506, 2020. 42

CLARAMUNT, S.; VAREA, A.; LOPEZ-DIAZ, D.; VELÁZQUEZ, M. M.; CORNET, A.; CIRERA, A. The importance of interbands on the interpretation of the raman spectrum of graphene oxide. **The Journal of Physical Chemistry C**, v. 119, n. 18, p. 10123–10129, 2015. 77, 78

DEERATTRAKUL, V.; DITTANET, P.; SAWANGPHRUK, M.; KONGKACHUICHAY, P. Co2 hydrogenation to methanol using cu-zn catalyst supported on reduced graphene oxide nanosheets. **Journal of CO2 Utilization**, v. 16, p. 104–113, 2016. 36, 63, 68

DEERATTRAKUL, V.; LIMPHIRAT, W.; KONGKACHUICHAY, P. Influence of reduction time of catalyst on methanol synthesis via co2 hydrogenation using

cu–zn/n-rgo investigated by in situ xanes. **Journal of the Taiwan Institute of Chemical Engineers**, v. 80, p. 495–502, 2017. 37

DEERATTRAKUL, V.; PUENGAMPHOLSRISOOK, P.; LIMPHIRAT, W.; KONGKACHUICHAY, P. Characterization of supported cu-zn/graphene aerogel catalyst for direct co2 hydrogenation to methanol: effect of hydrothermal temperature on graphene aerogel synthesis. **Catalysis Today**, v. 314, p. 154–163, 2018. 37, 52, 86, 93

DIEZ-RAMIREZ, J.; SANCHEZ, P.; RODRIGUEZ-GOMEZ, A.; VALVERDE, J. L.; DORADO, F. Carbon nanofiber-based palladium/zinc catalysts for the hydrogenation of carbon dioxide to methanol at atmospheric pressure. **Industrial & Engineering Chemistry Research**, v. 55, n. 12, p. 3556–3567, 2016. 25

DIN, I. U.; SHAHARUN, M. S.; NAEEM, A.; TASLEEM, S.; AHMAD, P. Revalorization of co2 for methanol production via zno promoted carbon nanofibers based cu-zro2 catalytic hydrogenation. **Journal of Energy Chemistry**, v. 39, p. 68–76, 2019. 24

DING, J.; LIU, Y.; YUAN, N.; DING, G.; FAN, Y.; YU, C. The influence of temperature, time and concentration on the dispersion of reduced graphene oxide prepared by hydrothermal reduction. **Diamond and Related Materials**, v. 21, p. 11–15, 2012. 33

DONG, X.; LI, F.; ZHAO, N.; XIAO, F.; WANG, J.; TAN, Y. Co2 hydrogenation to methanol over cu/zno/zro2 catalysts prepared by precipitation-reduction method. **Applied Catalysis B: Environmental**, v. 191, p. 8–17, 2016. 18

DUNN, C. **China's use of methanol in liquid fuels has grown rapidly since 2000**. 2017. Available from: <https://www.eia.gov/todayinenergy/detail.php?id=30072>. 5

DUTROW, B. L.; CLARK, C. M. X-ray powder diffraction (xrd). **Geochemical Instrumentation and Analysis**, p. 1–2, 2012. 123

EPP, J. X-ray diffraction (xrd) techniques for materials characterization. In: **Materials characterization using nondestructive evaluation (NDE) methods**. [S.l.]: Elsevier, 2016. p. 81–124. 122

ERTL, G.; KNÖZINGER, H.; WEITKAMP, J. **Handbook of heterogeneous catalysis**. [S.l.]: Citeseer, 1997. 127

FAN, X.; ZHANG, G.; ZHANG, F. Multiple roles of graphene in heterogeneous catalysis. **Chemical Society Reviews**, v. 44, n. 10, p. 3023–3035, 2015. 2, 34, 35, 88

FAN, Y. J.; WU, S. F. A graphene-supported copper-based catalyst for the hydrogenation of carbon dioxide to form methanol. **Journal of CO2 Utilization**, v. 16, p. 150–156, 2016. 37, 69

FLEISCH, T.; BASU, A.; GRADASSI, M.; MASIN, J. Dimethyl ether: a fuel for the 21st century. **Studies in Surface Science and Catalysis**, v. 107, p. 117–125, 1997. 9, 10

FLEISCH, T.; BASU, A.; SILLS, R. Introduction and advancement of a new clean global fuel: the status of dme developments in china and beyond. **Journal of Natural Gas Science and Engineering**, v. 9, p. 94–107, 2012. 2, 7, 9, 11

FRANCHINI, C. A.; LLORCA, J.; KUZNETSOV, A.; SILVA, A. M. Outstanding dispersion of ceo2 on reduced graphene oxide. implications for highly dispersed pd catalysts. **Diamond and Related Materials**, v. 109, p. 108061, 2020. 2, 33, 35, 57

FRUSTERI, F.; BONURA, G.; CANNILLA, C.; FERRANTE, G. D.; ALOISE, A.; CATIZZONE, E.; MIGLIORI, M.; GIORDANO, G. Stepwise tuning of metal-oxide and acid sites of cuznzr-mfi hybrid catalysts for the direct dme synthesis by co2 hydrogenation. **Applied Catalysis B: Environmental**, v. 176, p. 522–531, 2015. 11, 14, 15, 22, 115

FRUSTERI, F.; CORDARO, M.; CANNILLA, C.; BONURA, G. Multifunctionality of cu–zno–zro2/h-zsm5 catalysts for the one-step co2-to-dme hydrogenation reaction. **Applied Catalysis B: Environmental**, v. 162, p. 57–65, 2015. 115

FURIMSKY, E. Co2 hydrogenation to methanol and methane over carbon-supported catalysts. **Industrial & Engineering Chemistry Research**, v. 59, n. 35, p. 15393–15423, 2020. 23

GABBOTT, P. **Principles and applications of thermal analysis**. [S.l.]: John Wiley & Sons, 2008. 119, 120

GEIM, A. K.; NOVOSELOV, K. S. The rise of graphene. p. 11–19, 2010. 27

GOOD, D.; FRANCISCO, J.; JAIN, A.; WUEBBLES, D. J. Lifetimes and global warming potentials for dimethyl ether and for fluorinated ethers: Ch3ocf3 (e143a), chf2ochf2 (e134), chf2ocf3 (e125). **Journal of Geophysical Research: Atmospheres**, v. 103, n. D21, p. 28181–28186, 1998. 9

GROSSMANN, D.; DREIER, A.; LEHMANN, C.; GRÜNERT, W. Methanol synthesis over cu–zno aggregates supported on carbon nanotubes. **Applied Catalysis A: General**, v. 504, p. 351–360, 2015. 23

GUERRERO-CONTRERAS, J.; CABALLERO-BRIONES, F. Graphene oxide powders with different oxidation degree, prepared by synthesis variations of the hummers method. **Materials Chemistry and Physics**, v. 153, p. 209–220, 2015. 69

HASSAN, H. M.; ABDELSAYED, V.; RAHMAN, S. K. A. E.; ABOUZEID, K. M.; TERNER, J.; EL-SHALL, M. S.; AL-RESAYES, S. I.; EL-AZHARY, A. A. Microwave synthesis of graphene sheets supporting metal nanocrystals in aqueous and organic media. **Journal of Materials Chemistry**, v. 19, n. 23, p. 3832–3837, 2009. 32

HINRICHSEN, O.; GENGER, T.; MUHLER, M. Chemisorption of n2o and h2 for the surface determination of copper catalysts. **Chemical Engineering & Technology: Industrial Chemistry-Plant Equipment-Process Engineering-Biotechnology**, v. 23, n. 11, p. 956–959, 2000. 129

HONG, Z.-s.; CAO, Y.; DENG, J.-f.; FAN, K.-n. Co2 hydrogenation to methanol over cu/zno/al2o3 catalysts prepared by a novel gel-network-coprecipitation method. **Catalysis Letters**, v. 82, n. 1, p. 37–44, 2002. 18

HU, J.; LI, H.; MUHAMMAD, S.; WU, Q.; ZHAO, Y.; JIAO, Q. Surfactant-assisted hydrothermal synthesis of tio2/reduced graphene oxide nanocomposites and their photocatalytic performances. **Journal of Solid State Chemistry**, v. 253, p. 113–120, 2017. 38, 53, 58, 92

HUMMERS, J. W. S.; OFFEMAN, R. E. Preparation of graphitic oxide. **Journal of the American Chemical Society**, v. 80, n. 6, p. 1339–1339, 1958. 32

ISKANDAR, F.; ABDILLAH, O. B.; STAVILA, E.; AIMON, A. H. The influence of copper addition on the electrical conductivity and charge transfer resistance of reduced graphene oxide (rgo). **New Journal of Chemistry**, v. 42, n. 19, p. 16362–16371, 2018. 92

ITODO, A.; ITODO, H.; GAFAR, M. Estimation of specific surface area using langmuir isotherm method. **Journal of Applied Sciences and Environmental Management**, v. 14, n. 4, 2010. 57

JADHAV, S. G.; VAIDYA, P. D.; BHANAGE, B. M.; JOSHI, J. B. Catalytic carbon dioxide hydrogenation to methanol: a review of recent studies. **Chemical Engineering Research and Design**, v. 92, n. 11, p. 2557–2567, 2014. 3

JIANG, X.; KOIZUMI, N.; GUO, X.; SONG, C. Bimetallic pd–cu catalysts for selective co2 hydrogenation to methanol. **Applied Catalysis B: Environmental**, v. 170, p. 173–185, 2015. 19

KAKAMI, A.; YOKOTE, J.; EBARA, I.; TACHIBANA, T. Application of dimethyl ether to arcjet thruster as propellant. **Vacuum**, v. 83, n. 1, p. 77–81, 2008. 9

KONDRAT, S. A.; SMITH, P. J.; WELLS, P. P.; CHATER, P. A.; CARTER, J. H.; MORGAN, D. J.; FIORDALISO, E. M.; WAGNER, J. B.; DAVIES, T. E.; LU, L. Stable amorphous georgeite as a precursor to a high-activity catalyst. **Nature**, v. 531, n. 7592, p. 83–87, 2016. 17

KRISHNAMOORTHY, K.; VEERAPANDIAN, M.; MOHAN, R.; KIM, S.-J. Investigation of raman and photoluminescence studies of reduced graphene oxide sheets. **Applied Physics A**, v. 106, n. 3, p. 501–506, 2012. 63

KUMAR, V.; KUMAR, A.; LEE, D.-J.; PARK, S.-S. Estimation of number of graphene layers using different methods: a focused review. **Materials**, v. 14, n. 16, p. 4590, 2021. 69, 70

LIANG, X.-L.; DONG, X.; LIN, G.-D.; ZHANG, H.-B. Carbon nanotube-supported pd–zno catalyst for hydrogenation of co2 to methanol. **Applied Catalysis B: Environmental**, v. 88, n. 3-4, p. 315–322, 2009. 24

LIU, X.-M.; LU, G.; YAN, Z.-F.; BELTRAMINI, J. Recent advances in catalysts for methanol synthesis via hydrogenation of co and co2. **Industrial & Engineering Chemistry Research**, v. 42, n. 25, p. 6518–6530, 2003. 14, 16, 17, 85

LUK, V. N.; MO, G. C.; WHEELER, A. R. Pluronic additives: a solution to sticky problems in digital microfluidics. **Langmuir**, v. 24, n. 12, p. 6382–6389, 2008. 54

LUO, Z.; TIAN, S.; WANG, Z. Enhanced activity of cu/zno/c catalysts prepared by cold plasma for co2 hydrogenation to methanol. **Industrial & Engineering Chemistry Research**, v. 59, n. 13, p. 5657–5663, 2020. 26

MA, Q.; GENG, M.; ZHANG, J.; ZHANG, X.; ZHAO, T.-S. Enhanced catalytic performance for co2 hydrogenation to methanol over n-doped graphene incorporated cu-zno-al2o3 catalysts. **ChemistrySelect**, v. 4, n. 1, p. 78–83, 2019. 35

MACHADO, B. F.; SERP, P. Graphene-based materials for catalysis. **Catalysis Science & Technology**, v. 2, n. 1, p. 54–75, 2012. 28, 29, 30, 32

MARCANO, D. C.; KOSYNKIN, D. V.; BERLIN, J. M.; SINITSKII, A.; SUN, Z.; SLESAREV, A.; ALEMANY, L. B.; LU, W.; TOUR, J. M. Improved synthesis of graphene oxide. **ACS Nano**, v. 4, n. 8, p. 4806–4814, 2010. 33, 39

MARION, M. C.; GARBOWSKI, E.; PRIMET, M. Catalytic properties of copper oxide supported on zinc aluminate in methane combustion. **Journal of the Chemical Society, Faraday Transactions**, v. 87, n. 11, p. 1795–1800, 1991. 91

MARKETS AND MARKETS. **Methanol market**. 2021. Available from: <https://www.marketsandmarkets.com/Market-Reports/methanol-market-425.html>. 5

MAURO, M.; CIPOLLETTI, V.; GALIMBERTI, M.; LONGO, P.; GUERRA, G. Chemically reduced graphite oxide with improved shape anisotropy. **The Journal of Physical Chemistry C**, v. 116, n. 46, p. 24809–24813, 2012. 69

MCNAIR, H. M.; MILLER, J. M.; SNOW, N. H. **Basic gas chromatography**. [S.l.]: John Wiley & Sons, 2019. 131

MELIÁN-CABRERA, I.; GRANADOS, M. L.; FIERRO, J. Reverse topotactic transformation of a cu–zn–al catalyst during wet pd impregnation: relevance for the performance in methanol synthesis from co2/h2 mixtures. **Journal of Catalysis**, v. 210, n. 2, p. 273–284, 2002. 17

MENDOZA, M. E.; FERREIRA, E. H.; KUZNETSOV, A.; ACHETE, C. A.; AUMANEN, J.; MYLLYPERKIÖ, P.; JOHANSSON, A.; PETTERSSON, M.; ARCHANJO, B. S. Revealing lattice disorder, oxygen incorporation and pore formation in laser induced two-photon oxidized graphene. **Carbon**, v. 143, p. 720–727, 2019. 77

MITSUDA, K.; KIMURA, H.; MURAHASHI, T. Evaporation and decomposition of triton x-100 under various gases and temperatures. **Journal of Materials Science**, v. 24, n. 2, p. 413–419, 1989. 59, 60

MITSUTAKE, H.; POPPI, R. J.; BREITKREITZ, M. C. Raman imaging spectroscopy: history, fundamentals and current scenario of the technique. **Journal of the Brazilian Chemical Society**, v. 30, n. 11, p. 2243–2258, 2019. 125, 126

MUSK, E. **$100M gigaton scale carbon removal**. 2021. Available from: <https://www.xprize.org/prizes/elonmusk>. 12

MUZYKA, R.; DREWNIAK, S.; PUSTELNY, T.; CHRUBASIK, M.; GRYGLEWICZ, G. Characterization of graphite oxide and reduced graphene oxide obtained from different graphite precursors and oxidized by different methods using raman spectroscopy. **Materials**, v. 11, n. 7, p. 1050, 2018. 76

NAKADA, K.; ISHII, A. Migration of adatom adsorption on graphene using dft calculation. **Solid State Communications**, v. 151, n. 1, p. 13–16, 2011. 29, 30, 31

NIU, J.; LIU, H.; JIN, Y.; FAN, B.; QI, W.; RAN, J. Comprehensive review of cu-based co2 hydrogenation to ch3oh: insights from experimental work and theoretical analysis. **International Journal of Hydrogen Energy**, 2022. 1, 16

OGAWA, T.; INOUE, N.; SHIKADA, T.; OHNO, Y. Direct dimethyl ether synthesis. **Journal of Natural Gas Chemistry**, v. 12, n. 4, p. 219–227, 2003. 6, 7

OLAH, G. A. Beyond oil and gas: the methanol economy. **Angewandte Chemie International Edition**, v. 44, n. 18, p. 2636–2639, 2005. 1, 5, 12

OSSONON, B. D.; BÉLANGER, D. Synthesis and characterization of sulfophenyl-functionalized reduced graphene oxide sheets. **RSC Advances**, v. 7, n. 44, p. 27224–27234, 2017. 63

OTT, J.; GRONEMANN, V.; PONTZEN, F.; FIEDLER, E.; GROSSMANN, G.; KERSEBOHM, D. B.; WEISS, G.; WITTE, C. Methanol. **Ullmann's encyclopedia of industrial chemistry**, 2000. 3

PAREDES, J.; VILLAR-RODIL, S.; MARTINEZ-ALONSO, A.; TASCON, J. Graphene oxide dispersions in organic solvents. **Langmuir**, v. 24, n. 19, p. 10560–10564, 2008. 93

QIN, Z.-z.; SU, T.-m.; JI, H.-b.; JIANG, Y.-x.; LIU, R.-w.; CHEN, J.-h. Experimental and theoretical study of the intrinsic kinetics for dimethyl ether synthesis from co2 over cu–fe–zr/hzsm-5. **AIChE Journal**, v. 61, n. 5, p. 1613–1627, 2015. 115, 116, 118

RAO, C.; SOOD, A.; SUBRAHMANYAM, K.; GOVINDARAJ, A. Graphene: the new two-dimensional nanomaterial. **Angewandte Chemie International Edition**, v. 48, n. 42, p. 7752–7777, 2009. 27

RAO, C.; SOOD, A.; VOGGU, R.; SUBRAHMANYAM, K. Some novel attributes of graphene. **The Journal of Physical Chemistry Letters**, v. 1, n. 2, p. 572–580, 2010. 28

RAUDASKOSKI, R.; NIEMELÄ, M. V.; KEISKI, R. L. The effect of ageing time on co-precipitated cu/zno/zro2 catalysts used in methanol synthesis from co2 and h2. **Topics in Catalysis**, v. 45, n. 1, p. 57–60, 2007. 14, 18

Robertson, JH**Elements of X-ray diffraction by BD cullity**. [S.l.]: International Union of Crystallography, 1979. 123

ROODE-GUTZMER, Q. I.; KAISER, D.; BERTAU, M. Renewable methanol synthesis. **ChemBioEng Reviews**, v. 6, n. 6, p. 209–236, 2019. 6

SAEIDI, S.; AMIN, N. A. S.; RAHIMPOUR, M. R. Hydrogenation of co2 to value-added products—a review and potential future developments. **Journal of CO2 Utilization**, v. 5, p. 66–81, 2014. 12, 20, 80

SAMSUDIN, E. M.; HAMID, S. B. A.; JUAN, J. C.; BASIRUN, W. J. Influence of triblock copolymer (pluronic f127) on enhancing the physico-chemical properties and photocatalytic response of mesoporous tio2. **Applied Surface Science**, v. 355, p. 959–968, 2015. 59

SARAVANAN, K.; HAM, H.; TSUBAKI, N.; BAE, J. W. Recent progress for direct synthesis of dimethyl ether from syngas on the heterogeneous bifunctional hybrid catalysts. **Applied Catalysis B: Environmental**, v. 217, p. 494–522, 2017. 1, 12

SEMELSBERGER, T. A.; BORUP, R. L.; GREENE, H. L. Dimethyl ether (dme) as an alternative fuel. **Journal of Power Sources**, v. 156, n. 2, p. 497–511, 2006. 6, 7, 8, 9, 10, 11

SHELDON, D. Methanol production-a technical history. **Johnson Matthey Technology Review**, v. 61, n. 3, p. 172–182, 2017. 4, 5

SHEN, J.; YAN, B.; SHI, M.; MA, H.; LI, N.; YE, M. One step hydrothermal synthesis of tio 2-reduced graphene oxide sheets. **Journal of Materials Chemistry**, v. 21, n. 10, p. 3415–3421, 2011. 2, 33, 36

SHENG, Q.; YE, R.-P.; GONG, W.; SHI, X.; XU, B.; ARGYLE, M.; ADIDHARMA, H.; FAN, M. Mechanism and catalytic performance for direct dimethyl ether synthesis by co2 hydrogenation over cuznzr/ferrierite hybrid catalyst. **Journal of Environmental Sciences**, v. 92, p. 106–117, 2020. 117, 118

STUDT, F.; BEHRENS, M.; KUNKES, E. L.; THOMAS, N.; ZANDER, S.; TARASOV, A.; SCHUMANN, J.; FREI, E.; VARLEY, J. B.; ABILD-PEDERSEN, F. The mechanism of co and co2 hydrogenation to methanol over cu-based catalysts. **ChemCatChem**, v. 7, n. 7, p. 1105–1111, 2015. 115

SUN, K.; LU, W.; WANG, M.; XU, X. Low-temperature synthesis of dme from co2/h2 over pd-modified cuo–zno–al2o3–zro2/hzsm-5 catalysts. **Catalysis Communications**, v. 5, n. 7, p. 367–370, 2004. 14, 15, 21, 36

SUN, T.; ZHANG, Z.; XIAO, J.; CHEN, C.; XIAO, F.; WANG, S.; LIU, Y. Facile and green synthesis of palladium nanoparticles-graphene-carbon nanotube material with high catalytic activity. **Scientific Reports**, v. 3, n. 1, p. 1–6, 2013. 2, 36

SZEKELY, G.; NEBULONI, M.; ZERILLI, L. Thermal analysis-mass spectrometry coupling and its applications. **Thermochimica Acta**, v. 196, n. 2, p. 511–532, 1992. 120

TOYIR, J.; PISCINA, P. R. de la; FIERRO, J. L. G.; HOMS, N. Highly effective conversion of co2 to methanol over supported and promoted copper-based catalysts: influence of support and promoter. **Applied Catalysis B: Environmental**, v. 29, n. 3, p. 207–215, 2001. 19

TWIGG, M. V.; SPENCER, M. S. Deactivation of supported copper metal catalysts for hydrogenation reactions. **Applied Catalysis A: General**, v. 212, n. 1-2, p. 161–174, 2001. 22, 89

VALANT, A. L.; COMMINGES, C.; TISSERAUD, C.; CANAFF, C.; PINARD, L.; POUILLOUX, Y. The cu–zno synergy in methanol synthesis from co2, part 1: Origin of active site explained by experimental studies and a sphere contact quantification model on cu+ zno mechanical mixtures. **Journal of Catalysis**, v. 324, p. 41–49, 2015. 16, 85

VYAZOVKIN, S. Thermogravimetric analysis. **Characterization of Materials**, p. 1–12, 2002. 119

WALOCK, M. **Nanocomposite coatings based on quaternary metalnitrogen**. Tese (Doutorado) — Paris, ENSAM, 2012. 124

WANG, J.; ZENG, C. Al2o3 effect on the catalytic activity of cu-zno-al2o3-sio2 catalysts for dimethyl ether synthesis from co2 hydrogenation. **Journal of Natural Gas Chemistry**, v. 14, n. 3, p. 156–162, 2005. 14, 15, 21

WEBB, P. A. **Introduction to chemical adsorption analytical techniques and their applications to catalysis**. [S.l.: s.n.], 2003. 128

WENGUI, G.; HUA, W.; YUHAO, W.; WEI, G.; MIAOYAO, J. Dimethyl ether synthesis from co2 hydrogenation on la-modified cuo-zno-al2o3/hzsm-5 bifunctional catalysts. **Journal of Rare Earths**, v. 31, n. 5, p. 470–476, 2013. 14, 15, 21

WITOON, T.; NUMPILAI, T.; PHONGAMWONG, T.; DONPHAI, W.; BOONYUEN, C.; WARAKULWIT, C.; CHAREONPANICH, M.; LIMTRAKUL, J. Enhanced activity, selectivity and stability of a cuo-zno-zro2 catalyst by adding graphene oxide for co2 hydrogenation to methanol. **Chemical Engineering Journal**, v. 334, p. 1781–1791, 2018. 38, 68

WU, J.; JIN, Z.; WANG, B.; HAN, Y.; XU, Y.; LIANG, Z.; WANG, Z. Nickel nanoparticles encapsulated in microporous graphenelike carbon (ni@ mgc) as catalysts for co2 methanation. **Industrial & Engineering Chemistry Research**, v. 58, n. 45, p. 20536–20542, 2019. 34

XU, M.; LUNSFORD, J. H.; GOODMAN, D. W.; BHATTACHARYYA, A. Synthesis of dimethyl ether (dme) from methanol over solid-acid catalysts. **Applied Catalysis A: General**, v. 149, n. 2, p. 289–301, 1997. 21, 81

YANG, H.; ZHANG, C.; GAO, P.; WANG, H.; LI, X.; ZHONG, L.; WEI, W.; SUN, Y. A review of the catalytic hydrogenation of carbon dioxide into value-added hydrocarbons. **Catalysis Science & Technology**, v. 7, n. 20, p. 4580–4598, 2017. 22, 80

YANG, Y.; MIMS, C. A.; MEI, D.; PEDEN, C. H.; CAMPBELL, C. T. Mechanistic studies of methanol synthesis over cu from co/co2/h2/h2o mixtures: The source of c in methanol and the role of water. **Journal of Catalysis**, v. 298, p. 10–17, 2013. 16, 68

YE, R.-P.; DING, J.; GONG, W.; ARGYLE, M. D.; ZHONG, Q.; WANG, Y.; RUSSELL, C. K.; XU, Z.; RUSSELL, A. G.; LI, Q. Co 2 hydrogenation to high-value products via heterogeneous catalysis. **Nature Communications**, v. 10, n. 1, p. 1–15, 2019. 1, 12, 80

ZHANG, Y.; FEI, J.; YU, Y.; ZHENG, X. Study of co2 hydrogenation to methanol over cu-v/γ-al2o3 catalyst. **Journal of Natural Gas Chemistry**, v. 16, n. 1, p. 12–15, 2007. 14

ZHANG, Y.; LI, D.; ZHANG, S.; WANG, K.; WU, J. Co 2 hydrogenation to dimethyl ether over cuo–zno–al 2 o 3/hzsm-5 prepared by combustion route. **RSC Advances**, v. 4, n. 32, p. 16391–16396, 2014. 14, 15

ZHOU, Y.; BAO, Q.; TANG, L. A. L.; ZHONG, Y.; LOH, K. P. Hydrothermal dehydration for the “green” reduction of exfoliated graphene oxide to graphene and demonstration of tunable optical limiting properties. **Chemistry of Materials**, v. 21, n. 13, p. 2950–2956, 2009. 33

APPENDIX A - METHANOL AND DIMETHYL ETHER SYNTHESIS MECHANISMS AND KINETICS

Even though there are several studies regarding the mechanistic pathways of methanol synthesis over copper and zinc, there are still some uncertainties about the specific role of Cu and Zn on the reaction. Regarding the mechanisms, many authors agree that the hydrogenation reactions of the intermediate formate ($HCOO^-$) are the rate determining steps (RDS) (ARESTA et al., 2016). Based on this assumption, the classic reaction mechanism proposed for the methanol synthesis is presented in Scheme A.1. The subscript (a) denotes adsorbed species.

$$\begin{aligned} CO_2 + \tfrac{1}{2}\,H_2 &\rightleftharpoons HCOO_{(a)} \\ HCOO_{(a)} + 2\,H_{(a)} &\rightleftharpoons CH_3O_{(a)} + O_{(a)} \quad \textbf{(RDS)} \\ CH_3O_{(a)} + H_{(a)} &\rightleftharpoons CH_3OH \end{aligned} \tag{A.1}$$

A more detailed reaction mechanism for methanol synthesis over commercial $Cu/ZnO/Al_2O_3$ catalysts was proposed by Bussche and Froment (BUSSCHE; FROMENT, 1996), based on previous works, experimental data and kinetics modeling. Although the study focuses on methanol synthesis using syngas as reactant, the authors assume that CO_2 is the main source of carbon in methanol and take into account the reverse water gas shift reaction. Scheme A.2 shows the proposed reaction mechanism (BUSSCHE; FROMENT, 1996). In the scheme, "s" denotes a free active site, while "M · ns" represents an "M" species adsorbed on "n" active sites. Carbonate species are formed by further adsorption of CO_2 on oxidized copper surface, and then hydrogenated to formate. In agreement with the classic proposed reaction mechanisms for methanol synthesis (ARESTA et al., 2016), the rate determining step is the hydrogenation of formate, accepted as the longest living intermediate in methanol synthesis on Cu catalysts (BUSSCHE; FROMENT, 1996). Further hydrogenation occurs, resulting in the methanol formation and the release of surface oxygen. The free oxygen is also hydrogenated, starting the lower section of the mechanism, which is

the reverse water gas shift reaction.

$$
\begin{aligned}
\mathrm{H_{2(g)}} + 2\,\mathrm{s} &\rightleftharpoons 2\,\mathrm{H}\cdot\mathrm{s} && (K_{H2}) && \\
\mathrm{CO_{2(g)}} + \mathrm{s} &\rightleftharpoons \mathrm{O}\cdot\mathrm{s} + \mathrm{CO_{(g)}} && (k_1, K_1) && \textbf{(RDS)} \\
\mathrm{CO_{2(g)}} + \mathrm{O}\cdot\mathrm{s} + \mathrm{s} &\rightleftharpoons \mathrm{CO_3}\cdot 2\,\mathrm{s} && (K_2) && \\
\mathrm{CO_3}\cdot 2\,\mathrm{s} + \mathrm{H}\cdot\mathrm{s} &\rightleftharpoons \mathrm{HCO_3}\cdot 2\,\mathrm{s} + \mathrm{s} && (K_3) && \\
\mathrm{HCO_3}\cdot 2\,\mathrm{s} + \mathrm{s} &\rightleftharpoons \mathrm{HCO_2}\cdot 2\,\mathrm{s} + \mathrm{O}\cdot\mathrm{s} && (K_4) && \\
\mathrm{HCO_2}\cdot 2\,\mathrm{s} + \mathrm{H}\cdot\mathrm{s} &\rightleftharpoons \mathrm{H_2CO_2}\cdot 2\,\mathrm{s} + \mathrm{s} && (k_{5a}) && \textbf{(RDS)} \\
\mathrm{H_2CO_2}\cdot 2\,\mathrm{s} &\rightleftharpoons \mathrm{H_2CO}\cdot\mathrm{s} + \mathrm{O}\cdot\mathrm{s} && (K_{5b}) && \\
\mathrm{H_2CO}\cdot\mathrm{s} + \mathrm{H}\cdot\mathrm{s} &\rightleftharpoons \mathrm{H_3CO}\cdot\mathrm{s} + \mathrm{s} && (K_6) && \\
\mathrm{H_3CO}\cdot\mathrm{s} + \mathrm{H}\cdot\mathrm{s} &\rightleftharpoons \mathrm{CH_3OH_{(g)}} + 2\,\mathrm{s} && (K_7) && \\
\mathrm{O}\cdot\mathrm{s} + \mathrm{H}\cdot\mathrm{s} &\rightleftharpoons \mathrm{OH}\cdot\mathrm{s} + \mathrm{s} && (K_8) && \\
\mathrm{OH}\cdot\mathrm{s} + \mathrm{H}\cdot\mathrm{s} &\rightleftharpoons \mathrm{H_2O}\cdot\mathrm{s} + \mathrm{s} && (K_9) && \\
\mathrm{H_2O}\cdot\mathrm{s} &\rightleftharpoons \mathrm{H_2O_{(g)}} + \mathrm{s} && (K_{H2O}) &&
\end{aligned}
\tag{A.2}
$$

Considering the hypothesis of pseudo-steady-state for the concentration of some of the intermediate species and using a total number of sites balance, the authors were able to derive rate expressions for the methanol synthesis (Equation A.3) and the reverse water gas shift reaction (Equation A.4).

$$
r_{\mathrm{MeOH}} = k'_{5a} K'_2 K_3 K_4 K_{H_2} p_{\mathrm{CO_2}} p_{\mathrm{H_2}} \left(1 - \frac{1}{K_1^*} \frac{p_{\mathrm{H_2O}} p_{\mathrm{CH_3OH}}}{p_{\mathrm{CO_2}} p_{\mathrm{H_2}}^3}\right) \beta^3 \tag{A.3}
$$

$$
r_{\mathrm{RWGS}} = k'_1 p_{\mathrm{CO_2}} \left(1 - K_3^* \frac{p_{\mathrm{CO}} p_{\mathrm{H_2O}}}{p_{\mathrm{CO_2}} p_{\mathrm{H_2}}}\right) \beta, \tag{A.4}
$$

in which

$$
k'_{5a} = k_{5a} \cdot c_t^2 \tag{A.5}
$$

$$
k'_1 = k_1 \cdot c_t, \tag{A.6}
$$

c_t is the total sites number, β is the fraction of active sites and p_i is the partial pressure of species i. All K_i and k_i are equilibrium and rate constants, respectively, for step i of the mechanism indicated in the previous scheme. K_1^* and K_3^* are equi-

librium constants thermodynamically determined, that is, functions of temperature and pressure only (BUSSCHE; FROMENT, 1996).

The kinetic expressions derived by Bussche and Froment are widely applied in modeling reaction profiles in methanol synthesis from syngas and also from CO_2 and H_2 over commercial $Cu/ZnO/Al_2O_3$ catalysts (ALVAREZ et al., 2017).

Using Density Functional Theory (DFT) calculations, as well as feed-gas switching experiments, Studt et al. (STUDT et al., 2015) were able to investigate the actual effect of ZnO in copper-based catalysts. The results show that Zn decreases C-bound intermediates, therefore covering CO hydrogenation sites and promoting formate coverage. This indicates that the hydrogenation of formate, which is considered the slow step in methanol synthesis, can only be effectively performed on Cu catalyst if ZnO is present in the system. Thus, the results indicate that Cu/ZnO catalysts should be used for CO_2 hydrogenation but not for CO hydrogenation to methanol.

Regarding the DME synthesis from CO_2 hydrogenation, since most studies are focused on catalyst optimization, the mechanism for this reaction is not yet quite well understood (ARESTA et al., 2016). Nevertheless, studies show that on hybrid catalyst for DME production, a good performing catalyst should be multi-functional, so that its active site mixture promotes the methanol synthesis in metallic sites and at the same time, favours the methanol dehydration to DME (BONURA et al., 2017; FRUSTERI et al., 2015b; FRUSTERI et al., 2015a). The studies also emphasize that designing an efficient catalyst for the DME synthesis in one step requires a balanced distribution of acid and basic sites on the catalyst surface.

Qin et al. proposed a mechanism and rate expressions for the direct CO_2 hydrogenation to DME over $Cu/Fe/Zr/HZSM-5$ catalysts (QIN et al., 2015). The mechanism takes into account three main reactions, namely CO_2 hydrogenation to methanol, reverse water gas shift reaction and methanol dehydration to DME. The authors assume that among the three main reactions, methanol synthesis is the slowest. The rate determining step in the methanol synthesis reaction is the generation of the intermediate species. The proposed mechanism is presented in Scheme A.10, in which "s" denotes metallic sites and "HX" represents the HZSM-5 acid sites. The upper part represents the CO production through the reverse water gas shift mechanism, with the intermediate carboxyl species formation being the rate determining step. The second part is the hydrogenation of CO_2 to methanol mechanism, with the formic acid hydrogenation (RDS) producing adsorbed hydroxyl that will be converted in H_2O by the RWGSR mechanism. Methanol dehydration to DME is represented by

the lower section of the mechanism, in which methanol, when adsorbing on HZSM-5 acid sites, obtains an adsorbed proton (H) and dissociates into a positive carbon ion and water, that combined with an undissociated neighboring methanol forms DME. This combination is the result of a unimolecular nucleophilic substitution reaction, and it is the rate determining step in the methanol dehydration to DME. The CO_2 hydrogenation to methanol mechanism is similar to the mechanism proposed by Bussche and Froment (BUSSCHE; FROMENT, 1996), with the reaction proceeding via formation of HOCO, HCOO, HCOOH and then methanol formation from CH_3O hydrogenation.

Assuming that the Cu species serve as the active site only for the RWGSR and the methanol synthesis reaction, that the HZSM-5 species is the active site for methanol dehydration only and that nonrate determining steps reach equilibrium, the authors derived rate expressions for the RWGS reaction, CO_2 hydrogenation to methanol and DME synthesis, the expressions are represented by Equations A.7, A.8 and A.9, respectively. The relative errors calculated between the model and the experimental data of the partial pressure of all species were less than 10%, indicating that the model can be considered an accurate description of the CO_2 hydrogenation kinetics (QIN et al., 2015).

$$r_{\mathrm{RWGS}} = \frac{k_A p_{\mathrm{CO_2}} p_{\mathrm{H_2}}^{0,5} [1 - (K_A/K_{PA})(p_{\mathrm{CO}} p_{\mathrm{H_2O}}/p_{\mathrm{CO_2}} p_{\mathrm{H_2}})]}{(1 + K_{\mathrm{CO}} p_{\mathrm{CO}} + K_{\mathrm{H_2O}} p_{\mathrm{H_2O}})^2} \tag{A.7}$$

$$r_{\mathrm{MeOH}} = \frac{k_B p_{\mathrm{CO}} [1 - (K_B/K_{PB})(p_{\mathrm{CH_3OH}}/p_{\mathrm{CO}} p_{\mathrm{H_2}}^{0,5})]}{(1 + K_{\mathrm{CO}} p_{\mathrm{CO}} + K_{\mathrm{H_2O}} p_{\mathrm{H_2O}})^3} \tag{A.8}$$

$$r_{\mathrm{DME}} = \frac{k_C [p_{\mathrm{CH_3OH}}^2/p_{\mathrm{H_2O}} - (K_3/K_{PC}) p_{\mathrm{DME}}]}{(1 + K_{\mathrm{CH_3OH}} p_{\mathrm{CH_3OH}} + K_{\mathrm{H_2O}} p_{\mathrm{H_2O}})^2} \tag{A.9}$$

$$
\begin{aligned}
\mathrm{H_2} + 2\,\mathrm{s} &\rightleftharpoons 2\,\mathrm{H}\cdot\mathrm{s} && \\
\mathrm{CO_2} + \mathrm{H}\cdot\mathrm{s} + \mathrm{s} &\rightleftharpoons \mathrm{HOCO}\cdot 2\,\mathrm{s} && \textbf{(RDS)} \\
\mathrm{HOCO}\cdot 2\,\mathrm{s} &\rightleftharpoons \mathrm{CO}\cdot\mathrm{s} + \mathrm{OH}\cdot\mathrm{s} && \\
\mathrm{CO}\cdot\mathrm{s} &\rightleftharpoons \mathrm{CO} + \mathrm{s} && \\
\\
\mathrm{CO_2} + \mathrm{H}\cdot\mathrm{s} + \mathrm{s} &\rightleftharpoons \mathrm{HCOO}\cdot 2\,\mathrm{s} && \\
\mathrm{HCOO}\cdot 2\,\mathrm{s} + \mathrm{H}\cdot\mathrm{s} &\rightleftharpoons \mathrm{HCOOH}\cdot 2\,\mathrm{s} + \mathrm{s} && \\
\mathrm{HCOOH}\cdot 2\,\mathrm{s} + \mathrm{H}\cdot\mathrm{s} &\rightleftharpoons \mathrm{H_2CO}\cdot 2\,\mathrm{s} + \mathrm{OH}\cdot\mathrm{s} && \textbf{(RDS)} \\
\mathrm{H_2CO}\cdot 2\,\mathrm{s} + \mathrm{H}\cdot\mathrm{s} &\rightleftharpoons \mathrm{H_3CO}\cdot\mathrm{s} + 2\,\mathrm{s} && \\
\mathrm{H_3CO}\cdot\mathrm{s} + \mathrm{H}\cdot\mathrm{s} &\rightleftharpoons \mathrm{CH_3OH}\cdot\mathrm{s} + \mathrm{s} && \\
\mathrm{CH_3OH}\cdot\mathrm{s} &\rightleftharpoons \mathrm{CH_3OH} + \mathrm{s} && \\
\\
\mathrm{OH}\cdot\mathrm{s} + \mathrm{H}\cdot\mathrm{s} &\rightleftharpoons \mathrm{H_2O}\cdot\mathrm{s} + \mathrm{s} && \\
\mathrm{H_2O}\cdot\mathrm{s} &\rightleftharpoons \mathrm{H_2O} + \mathrm{s} && \\
\\
\mathrm{CH_3OH} + \mathrm{HX} &\rightleftharpoons \mathrm{CH_3OH}\cdot\mathrm{HX} && \\
\mathrm{CH_3^+}\cdot\mathrm{X^-} + \mathrm{CH_3OH}\cdot\mathrm{HX} &\rightleftharpoons \mathrm{CH_3OHCH_3}\cdot\mathrm{HX} + \mathrm{X^-} && \textbf{(RDS)} \\
\mathrm{CH_3OHCH_3}\cdot\mathrm{HX} + \mathrm{X^-} &\rightleftharpoons \mathrm{CH_3OCH_3}\cdot\mathrm{HX} + \mathrm{HX} && \\
\mathrm{CH_3OCH_3}\cdot\mathrm{HX} &\rightleftharpoons \mathrm{CH_3OCH_3} + \mathrm{HX} && \\
\mathrm{H^+} + \mathrm{X^-} &\rightleftharpoons \mathrm{HX} &&
\end{aligned}
\tag{A.10}
$$

Another mechanism for the direct CO_2 hydrogenation to DME was recently proposed by Sheng et al.(SHENG et al., 2020). The authors investigated the catalytic performance of a Cu/Zn/Zr/ferrierite hybrid catalyst and deduced a reaction mechanism through the use of in situ diffuse reflectance infrared Fourier transform spectroscopy (DRIFTS) (SHENG et al., 2020). The proposed mechanism is illustrated in Figure A.1.

Figure A.1 - Reaction mechanism of the direct DME synthesis by CO_2 hydrogenation over Cu/Zn/Zr/ferrierite catalyst.

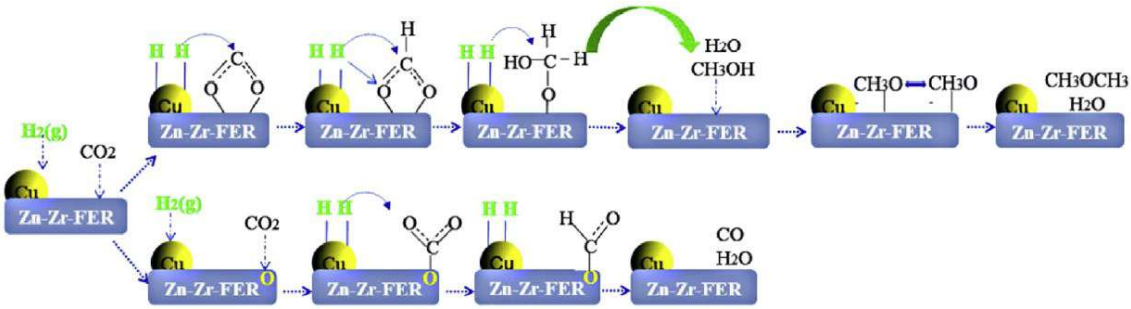

Source: Sheng et al. (2020).

The upper section describes the methanol synthesis and posterior dehydration to DME, while the lower part is the RWGSR mechanism, indicating that it occurs parallel to the CO_2 hydrogenation to methanol. The pathway occurs by CO_2 firstly adsorbing dissociatively on the catalyst surface and reacting with surface H on metallic Cu sites to form intermediate formate species. Similar to the mechanisms previously discussed (BUSSCHE; FROMENT, 1996; QIN et al., 2015), formate is further hydrogenated to H_2COOH, which decomposes into H_2CO and OH forming CH_3OH and H_2O by another hydrogenation process. The desorbed CH_3OH species is adsorbed on the acid ferrierite site generating methoxy groups. DME is produced by a combination of two neighboring methoxy intermediates. The RWGSR mechanism starts with the adsorption of CO_2 with oxygen, and then forms HCOO species through hydrogenation, this intermediate decomposes into CO and OH (SHENG et al., 2020).

APPENDIX B - CHARACTERIZATION METHODS

B.1 Thermogravimetric Analysis (TGA)

Thermogravimetric Analysis (TGA) is an experimental technique in which the change in the mass of a sample is measured as the sample temperature is varied with a controlled temperature program. Usually the sample is heated at a constant heating rate or held at a constant temperature, but other non-linear methods such as sample controlled TGA, in which the heating rate varies with the sample mass, are also applied.

The sample mass is measured by a thermobalance, a sensitive analytical balance with an electronically programmed furnace, with a typical temperature range $25-1600°C$ and heating rates in the range $1-20°C/min$, even though the rates can reach up to hundreds of $°C/min$. In general, the choice of temperature program depends on the information desired about the sample. Furthermore, the atmosphere used in TGA experiments can be reactive, oxidizing or inert, changes in the atmosphere during a run are also possible (VYAZOVKIN, 2002).

There are many mechanisms by which mass loss can occur, including evaporation of volatile constituents, drying, desorption and adsorption of gases, water loss or uptake, oxidation of metals, oxidative decomposition of organic substances in air or oxygen, thermal decomposition in an inert atmosphere with gaseous products forming and heterogeneous chemical reaction.

TGA results are usually represented as a TGA curve, which is a percent mass vs temperature and/or time plot. A commonly used complementary report is the first derivative of the TGA curve with respect to temperature or time, it shows peaks indicating the rate at which mass is changed, this representation is known as the Differential Thermogravimetric (DTG) curve. Figure B.1 presents both the TGA and DTG curve of the stepwise decomposition of calcium oxalate monohydrate, in which a heating rate of 30K/min was employed to a 19 mg sample, the TGA curve was normalized, thus beginning at 100%. The figure indicates mechanisms for each step of mass loss and from the DTG curve it is possible to quantify the loss rate (GABBOTT, 2008).

The TGA procedure is often coupled with other analytical techniques to increase its capability to characterize materials, the most common coupling is TGA with Mass Spectrometry (MS), due to the high sensitivity and specificity of the method.

The TGA-MS coupling can be performed in two basic system types: direct coupling under vacuum and systems in which the thermobalance operates under atmospheric pressure. The latter presents several advantages, since in many studies, inert, oxidizing, reducing or self-generated atmosphere conditions are desirable for carrying out the thermal analysis.

While TGA usually provides quantitative information about the total mass loss at a temperature range, MS identifies off-gases and indicates their relative proportion. By using MS data, it is possible to build a calibration curve where the integrated peak area of a selected mass peak is plotted against the mass loss found in samples of known composition, then the amount of a specific component in the off-gas can be related to the original sample.

In modern TGA-MS instruments, quadrupole mass spectrometers are usually chosen due to their simple and space-saving construction, good resolution in fast mass scans and constant resolution over the whole mass range. This mass analyzer separates ions according to the stability of the flight trajectory by an oscillating electric field, which is generated when a radio frequency voltage is applied between a pair of opposite rods of the quadrupole. The equipment has two possible classes of ion source: axial beam ion source, where the electron beam and ion extraction are both in the axial direction, enabling simple construction and high sensitivity, and cross-beam ion source, in which the electron beam and ion extraction are located at right angles (90°) (SZEKELY et al., 1992).

Figure B.1 - Stepwise decomposition of calcium oxalate monohydrate.

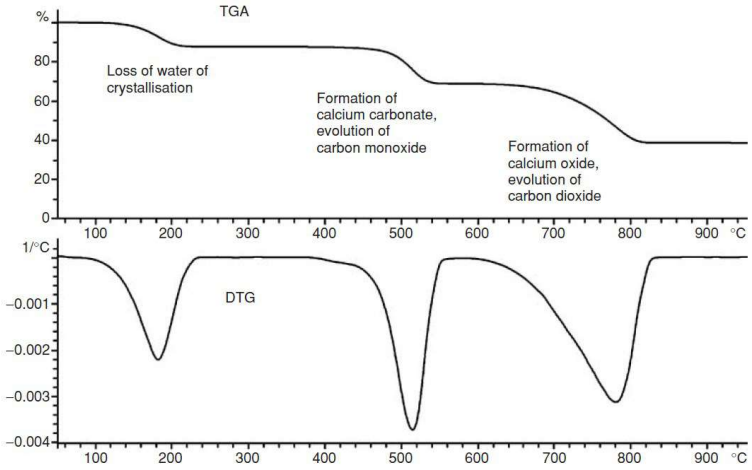

Source: Gabbott (2008).

B.2 X-Ray Diffraction (XRD)

X-Ray Diffraction (XRD) is an analytical technique generally used to identify crystalline material phases and obtain information on the unit cell dimensions. The determination of unknown solids is crucial for research in material science, engineering, geology, environmental science and biology.

The method is based on the constructive interference of monochromatic X-rays and a crystalline sample, produced when conditions satisfy Bragg's Law, given by

$$n\lambda = 2d\sin(\theta) \tag{B.1}$$

where n is the number of wavelengths, λ is the wavelength of the X-ray, d is the d-spacing of the crystal layers and θ is the incident angle, which is the angle between incident ray and the scatter plane. This law relates the wavelength of electromagnetic radiation to the diffraction angle and the lattice spacing in a crystalline sample.

The three main elements of a X-ray diffractometer equipment are: an X-ray tube, a sample holder and an X-ray detector. The X-rays are generated in a cathode ray tube by heating a filament to produce electrons, which are accelerated toward a target by voltage appliance. A characteristic X-ray diffractogram is then produced when the electrons have sufficient energy to dislodge inner shell electrons of the target material. The most common diffractogram consists of K_α and K_β components, in which K_α is composed of $K_{\alpha1}$ and $K_{\alpha2}$, and the specific wavelengths are characteristic of the target material (usually Cu for single-crystal diffraction, with CuK_α radiation = 1,5418 Å). The X-rays are collimated and directed toward the sample, and the intensity of the reflected X-rays is recorded as the sample and detector are rotated. The detection is carried out through an intensity peak, formed when the geometry of the incident X-rays satisfies Bragg's Law. Figure B.2 represents the geometrical condition to satisfy Bragg's Law.

In an X-ray diffractometer, the sample rotates in the path of the collimated X-ray beam at an angle θ while the detector is mounted on an arm that rotates at an angle 2θ to collect the diffracted X-rays. For typical analysis, data is collected at 2θ in the range $5° - 70°$, preset in the X-ray scan.

The X-Ray signal is recorded, processed and converted to a count rate, which is then output to a device such as a printer or computer. Results are often presented as peak positions at 2θ and X-rays intensities in the form of tables or x-y plots. The intensity

Figure B.2 - Geometrical condition for diffraction from lattice planes.

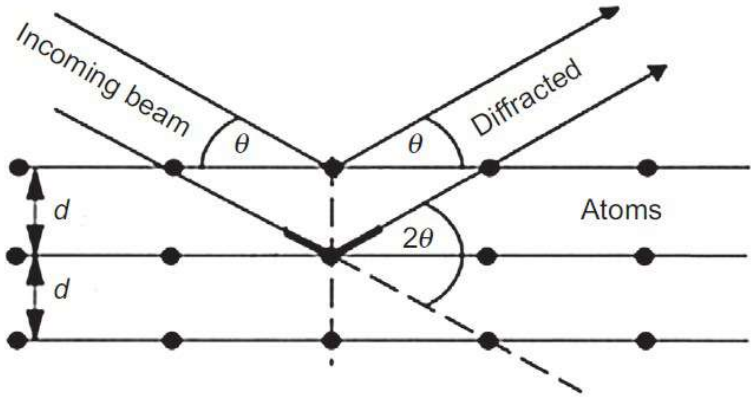

Source: Epp (2016).

is reported as peak height or integrated intensity, that is, the area under the peak. The determination of the unknown material is done by obtaining the d-spacing through the solution of the Bragg equation (B.1) for the appropriate wavelength λ. Then match routines compare the d-spacing of the unknown to those of known materials, indicating which elements compose the sample. This is possible because each mineral has an unique set of d-spacing. Files of d-spacing for hundreds of thousands of known inorganic compounds are provided by the International Centre for Diffraction Data (ICDD), formerly known as the Joint Committee on Powder Diffraction Standards (JCPDS).

Besides identifying unknown solids, XRD also has applications including measurement of sample purity, determination of unit cell dimensions, characterization of crystalline materials and identification of fine-grained minerals such as clays. Furthermore, with specialized techniques, XRD can be used to determine crystal structures through Rietveld refinement and modal amounts of minerals, characterize thin films samples and make textural measurements, such as orientation of grains in a polycrystalline sample.

XRD is a powerful and rapid method, it provides an unambiguous mineral determination, minimal sample preparation is required, the equipment is widely available and data interpretation is relatively straight forward. Nonetheless, there are some limitations including the fact that homogeneous and single phase materials are best suited for identification of an unknown, and for mixed materials, detection limit is $\sim 2\%$ of a sample. Also, indexing patterns for non-isometric crystal systems for unit cell determinations is a complex procedure, and peak overlay may occur in high

angle diffraction (DUTROW; CLARK, 2012; ROBERTSON, 1979).

B.3 Scanning Electron Microscopy (SEM)

Scanning Electron Microscopy (SEM) is a characterization technique based on the interaction of a sample with accelerated electrons, it provides information about the surface topography, chemical composition and the crystalline structure.

A scanning electron microscope operates by focusing a beam of electrons generated by a thermionic or field emitting source. In thermionic sources, the filaments (usually Tungsten or LaB_6) are heated to produce thermal emission of electrons, having stable currents and requiring less complex vacuum systems ($\sim 10^{-6}$ Torr). On the other hand, in field emitting sources an electric field is applied to a pointed tip until quantum mechanical tunneling of electron occurs. Field emitting sources present higher resolution and very long potential lifetime, although it requires ultra-high vacuum in the gun area ($\sim 10^{-10}$ Torr). Figure B.3 presents a scheme of a Scanning Electron Microscope. An applied current on the electromagnetic lenses system produces a magnetic field, focusing the electron beam on the stage where the sample is held. The beam probe is scanned across the surface of the specimen making the electrons interact with the various sections of the surface.

The interaction of the electrons with the sample produces several types of signals that form the SEM images. Secondary Electrons (SE) are low energy electrons that escape from the specimen atoms and are collected by a specific detector (Fig B.3), providing high resolution images with information regarding the topography of the specimen. Backscattered Electrons (BSE) are primary beam electrons that approach the nucleus of an atom and are scattered through a large angle, giving information about elements of higher atomic mass. If an incident electron knocks out a core shell electron from an atom of the specimen, therefore causing outer shell electrons to fill the vacancy, the energy difference is released as a characteristic X-ray, which reveals the chemical composition of the sample.

B.4 Raman spectroscopy

Raman Spectroscopy is a non-destructive chemical analysis technique that makes use of Raman scattering, also known as inelastic scattering of monochromatic laser lights, it provides detailed information about chemical structure, polymorphy, crystallinity and molecular interactions.

Every vibrational spectroscopy is based on one of three phenomena that occur when

Figure B.3 - Scheme of a Scanning Electron Microscope (SEM).

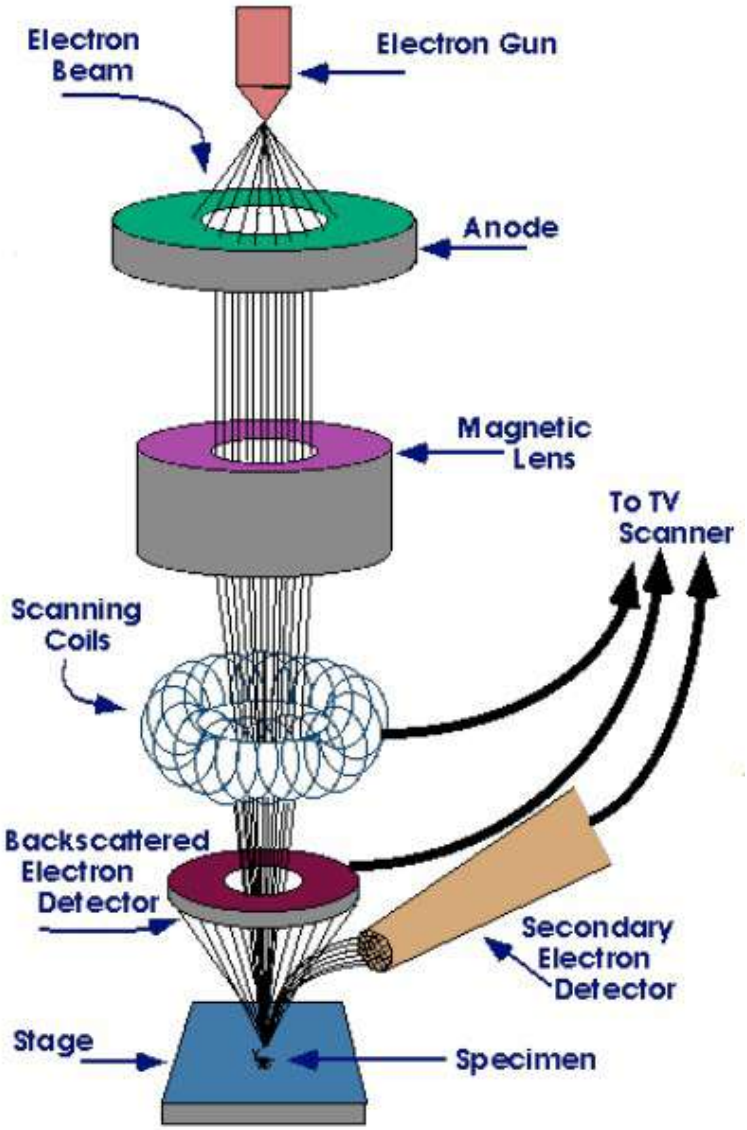

Source: Walock (2012).

electromagnetic radiation interacts with a molecule: absorption, transmission and scattering. The latter is responsible for the Raman spectra. In Raman scattering, the intensity of the bands depends on the variation of induced dipole moment, thus nonpolar bonds present greater signals that polar bonds. The process consists of focusing monochromatic light on the sample, making the incident photons go into a virtual state and then the scattered photons are measured. The virtual state does not refer to any pre-existing electronic or vibrational state of the molecule, it is only created at the time of laser incidence.

Figure B.4 presents a schematic illustration of possible absorption mechanisms when

a laser interacts with the sample molecule, the upward arrows represent the excitation while downward arrows indicate the emission. The radiation scattering is divided into Rayleigh, Stokes and anti-Stokes, the most common being the Rayleigh scattering (or elastic scattering), in which no considerable exchange of energy occurs and thus, photons return to the fundamental state ($\nu = 0$). When photons interact with the molecule causing polarization, if the energy is transferred from the photon to the molecule, the scattered photon has a longer wavelength and lower energy, this is called Stokes scattering, and if the opposite occurs, then it is called anti-Stokes scattering. This energy difference is equal to the energy difference between the excited ($\nu = 1$) and fundamental vibrational states. Most of the measured Raman scattering is Stokes, given that the molecules at room temperature are mainly in the fundamental state, and only a small portion of the scattered lights derive from the anti-Stokes scattering.

The strength of the Raman signal is proportional to the fourth power of the laser wavelength, therefore the use of more energetic lasers provide better performance. Nonetheless, this is not always favorable because the photon could acquire enough energy to reach the electronic excited state generating a fluorescence spectrum and obscuring the Raman scattering.

Figure B.4 - Schematic illustration of absorption of monochromatic light.

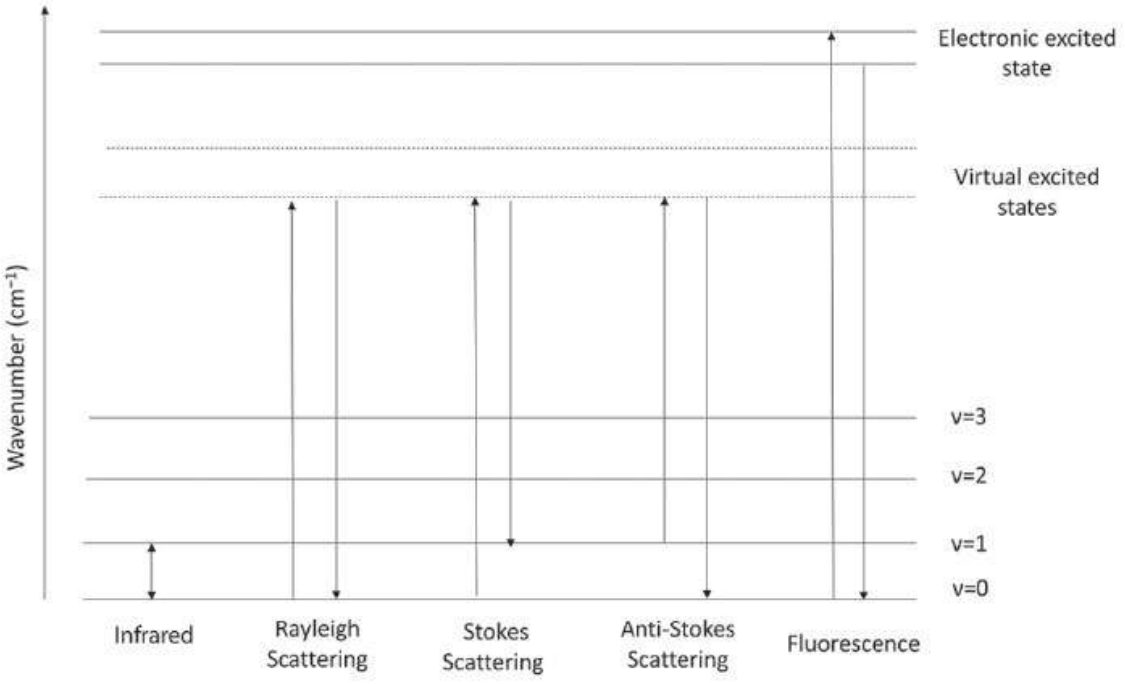

Source: Mitsutake et al. (2019)

The most commonly used method for data acquisition is called point mapping. The laser is focused on a point in the sample and a spectrum is acquired at this point, the process is repeated as the sample is moved and new spectra are acquired in the same region. Other methods for acquiring Raman spectroscopy data include Linear scan mapping, where the spectra is obtained over a line of pixels, and imaging techniques, in which the laser illuminates the entire sample, allowing acquisition of spectra of the whole region simultaneously, with the disadvantage of the laser being unfocused. For data analysis, there are two possible procedures: univariate and multivariate analysis, the former being the most utilized. For the univariate analysis, only one value is chosen (such as band area or peak height) to represent the analyte of interest, while in the multivariate analysis the full Raman spectrum is used.

Material characterization is the area with the highest number of Raman spectroscopy applications, the main materials analyzed are polymers, catalysts and carbon compounds, including graphite and graphene. In most cases, it is used along other imaging techniques including Transmission Electron Microscopy (TEM), Scanning Electron Microscopy (SEM) and Atomic Force Microscopy (AFM). Other areas with Raman applications are Art and Archaeology, Chemistry, Geology, Life sciences, Pharmaceutics and Semiconductors. In general, Raman spectroscopy analysis is well suited for solids, powders, liquids, gels, slurries, gases, biological materials, pure chemicals, mixtures, solutions, metallic oxides and corrosion.

Raman spectroscopy also allows the visualization of the distribution of compounds in the analyte, making it possible to determine the homogeneity of the distribution, understanding the physical properties of materials. One of the most advantageous factors is the possibility of detecting small amounts of analyte, that is, even if the sample is absent in some pixels, a higher concentration is found on other pixels, allowing the detection of low concentrations. Furthermore, the main disadvantages of Raman imaging are spatial resolution, which is limited by diffraction; sample components with low Raman signals; fluorescence interference and subsampling, which occurs when the mapped area is too small and thus, unrepresentative of the sample (MITSUTAKE et al., 2019).

B.5 Chemical adsorption

Chemical adsorption (chemisorption) analysis is one of the most utilized techniques for the characterization of metallic catalysts. If the stoichiometry of the adsorption reaction is known, the procedure provides information on the metal surface area and

metal dispersion.

The analysis can be carried out by static methods, such as volumetry and gravimetry, or by dynamic methods through a Thermal Conductivity Detector (TCD). For static methods, the equipment consists of a gas dosing device, a pressure gauge, a pumping system, a cell and an oven. In this procedure, a previously pretreated and evacuated material is put in contact with a known quantity of the adsorbate gas. In static volumetry the amount of adsorbed gas is determined by measuring the pressure after the adsorption process reaches the equilibrium. In gravimetry analysis the amount of adsorbed gas is measured by weighting the sample with an electrobalance. The adsorption isotherm is obtained after successive doses of gas, by relating the amount of adsorbed gas with the equilibrium pressure.

On the other hand, in dynamic methods an inert gas initially flushes the catalyst in order to remove all adsorbed molecules, then the flow is switched to the adsorbate gas until the TCD shows a constant gas phase composition. After purging the remaining gas, the reactive flow is turned back on to evaluate the dead volume and possible reversible adsorption phenomena (ERTL et al., 1997).

A chemisorption isotherm is a set of amount of gas adsorbed versus pressure data points that characterize the adsorption process at constant temperature. Assuming that the surface of a solid catalyst contains a fixed number of active adsorption sites, and that only one molecule may occupy a site in a certain time, the Langmuir Isotherm can be written as

$$\theta = \frac{bP}{(1 + bP)}, \tag{B.2}$$

in which θ is the surface coverage defined as the ratio between the adsorbed molecules and total number of available sites, P is pressure and b is a combination of the adsorption equilibrium constant and the concentration-pressure proportionality. An illustration of the steps required in order to obtain the chemisorption isotherm is presented in Figure B.5. The molecules adsorbed weakly by physisorption (reversible) are indicated by R and the strongly adsorbed molecules that form the chemisorbed monolayer are represented by I (irreversible). The first step, represented by the upper section (Figure B.5), shows the sample after initial cleaning by heat and vacuum. After the first adsorption test, both R and I molecules are adsorbed on the active metal surface generating the initial isotherm, which is a combination of reversible and irreversible adsorption. The weakly adsorbed molecules are then removed by vacuum or flushing, leaving only those that established strong chemisorption bonds with the surface. Afterwards, a second test is performed under the same conditions as the

first test, however this time the active surface is already covered with a chemisorbed monolayer, so that the uptake of adsorbate will be restricted to reversible adsorption, resulting in a second isotherm. Finally, by subtracting the quantity reversibly adsorbed from the first isotherm at each pressure point yields a new isotherm of irreversible adsorption only (WEBB, 2003).

Figure B.5 - Steps to obtain the chemisorption isotherm.

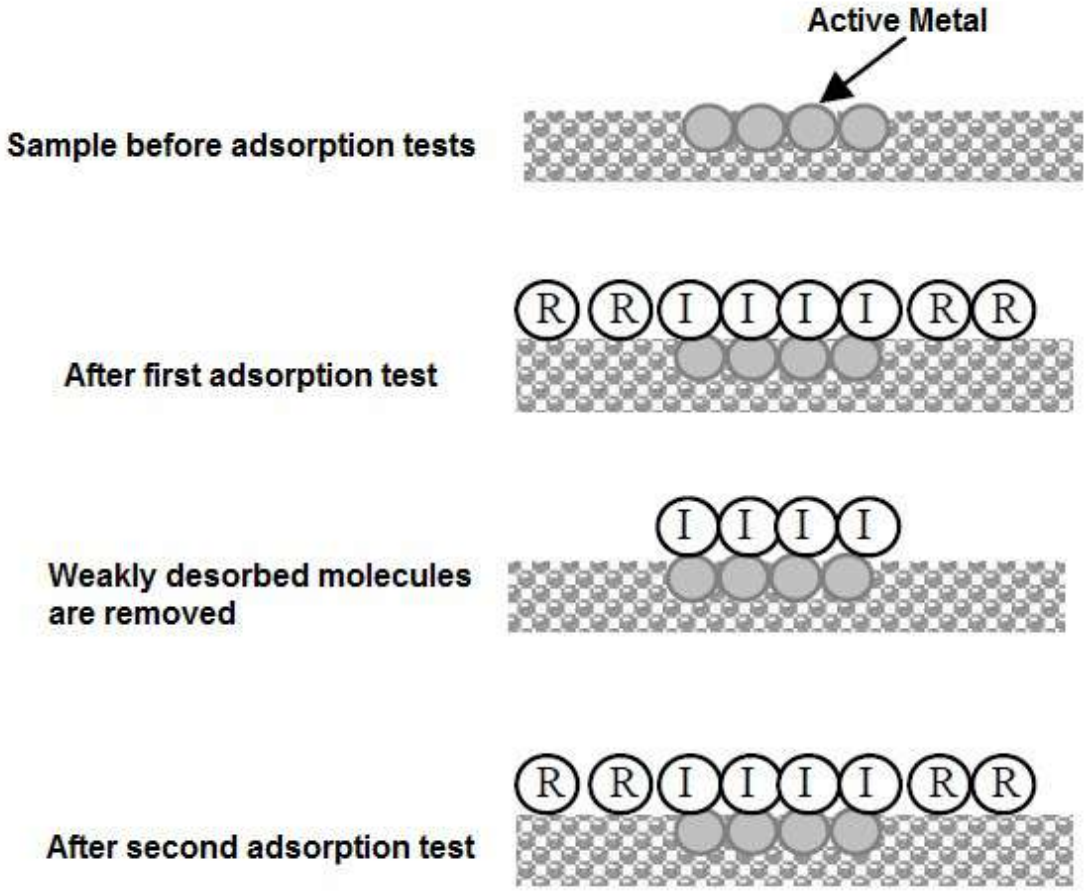

Source: Webb (2003).

From the irreversible adsorption isotherm, the monolayer capacity of the active surface can be determined. However, the function is asymptotic to the value of total coverage, so that the plateau of the curve must be extrapolated back to the y-axis to calculate the monolayer capacity value. The specific active surface area can be determined afterwards, by multiplying the number of molecules adsorbed per gram by the area occupied by one molecule, which can often be found in literature. The chemisorption analysis also determines the specific quantity of active metal, which

can be used to calculate metal dispersion and percent metal. For the estimation of active particle size, it is assumed that the crystallite shape is of regular geometry such as a sphere, then the particle diameter can be calculated by

$$D = \frac{6}{\rho_m A_m}, \tag{B.3}$$

where ρ_m is the molecular density and A_m is the active surface area determined previously.

The determination of Cu metal areas is often performed by chemisorption of nitrous oxide (N_2O), which is based on the decomposition of N_2O on copper atoms, following the reaction

$$N_2O + 2Cu_{(s)} \rightarrow Cu_2O_{(s)} + N_2. \tag{B.4}$$

Hinrichsen et al. performed N_2O chemisorption tests and reported the isothermal N_2O flow method as simple, fast and reliable technique. The experiment was carried out at room temperature and atmospheric pressure, using a mixture of 1% N_2O in He. The specific metal surface found for Cu was 17.8 m^2/g (HINRICHSEN et al., 2000).

B.6 Gas Chromatography (GC)

Gas Chromatography (GC) is a separation method in which the sample is vaporized and carried by a gas phase known as the carrier gas through a stationary bed with large surface area. The sample components are then separated from one another due to different affinities with the column and relative vapor pressures. This technique is used both for reactants and reaction products.

The attraction of a certain component to the stationary phase can be expressed by an equilibrium constant known as the distribution constant (K_c), which is defined as the ratio between the concentration of a solute A in the stationary phase and its concentration in the gas phase.

$$K_c = \frac{[A]_S}{[A]_M} \tag{B.5}$$

A solute is retained by the column and characterized by the retention volume or retention time, in other words, the carrier gas volume necessary to elute the solute. Considering the gas phase flow rate (F_c) constant, the retention volume is given by

$$V_R = t_R \times F_c. \tag{B.6}$$

When the retention volume (and therefore retention time) is reached, then the chromatogram, which is the resulting graph in a chromatography analysis, will signal a peak. An earlier smaller peak represents a solute that passes through the column without stopping, in GC this is often air or methane and this peak's retention volume is called hold-up volume or void volume (V_M), which serves to measure the inter-particle volume of the column.

The retention volume can be related to the theoretical distribution constant

$$V_R = V_M + K_c V_S \tag{B.7}$$

where V_R is the retention volume and V_M and V_S represent the volumes of mobile and stationary phases, respectively.

The purposes of the carrier gas are carrying the sample through the column and providing a suitable matrix for the detector to identify components individually. For both the Thermal Conductivity and Flame Ionization detectors, Helium (He) is recommended as the carrier gas.

One of the most crucial aspects of chromatography is the column choice. A Capillary column is a simple open tube without any packing material, a thin layer of liquid phase coats the inside wall instead. These columns have very high lengths (up to 100m), which allows efficient separation of complex mixtures. The efficiency is one of the reasons why most of the analysis nowadays are carried out in capillary columns. As for the tube material, many types of columns such as glass, copper and stainless steel have been used, however, fused silica is the most popular today, for it is the most flexible one, easy to handle and the most inert column.

The Flame Ionization Detector (FID) is the most commonly used detector in gas chromatography. It consists of two opposite charged electrodes and small flame of hydrogen and air. The vaporized sample is mixed with hydrogen and then burned in the FID, producing ions that cause a current between the two electrodes proportionally to the amount of compound in the sample. This current is then measured by an electrometer, amplified and fed into an integrator. The signal is represented by a peak, and the area of the peak is proportional to the concentration of sample burned. This detector is suited to analyse hydrocarbons and oxygenates.

Another important detector is the universal Thermal Conductivity Detector (TCD), one of the oldest used in gas chromatography. It consists of two or four cell cavities

drilled into a metal block, each cavity containing a resistance filament incorporated in a Wheatstone Bridge circuit. When the carrier gas passes through these filaments, the circuit is balanced and no signal is being emitted. Then, when an analyte is present, the thermal conductivity of the gas is decreased, causing a slight change in the filament temperature which results in a large increase in resistance, unbalancing the bridge. The voltage produced between opposite corners of the circuit is fed to an integrator and the signal is represented by a peak, similar to the representation of FID signals (MCNAIR et al., 2019).